Aqueous Solution and Vapor Phase Adsorption of Oxygenates onto Zeolites

A Dissertation
Submitted to the Faculty of the Graduate School
of the University of Minnesota
by

Elizabeth Emma Mallon

In Partial Fulfillment of the Requirements
for the Degree of
Doctor of Philosophy

Advisors: Michael Tsapatsis and Aditya Bhan

November 2012

Acknowledgments

I would like to thank my advisors, Professors Michael Tsapatsis and Aditya Bhan, whose patience and commitment to rigorous science and student scholarship has shaped me into the researcher I am today. I often think of Michael as a wise zen master, someone who is always calm and has the remarkable ability to ask penetrating scientific questions on a range of research topics. I am so thankful for the time he has taken to share his perspective with me on research and on life. I had the unique experience of first meeting Aditya when he was still a post-doc, and if it weren't for his research ideas and enthusiasm, I may not have attended the University of Minnesota. I am very thankful for the countless hours he has spent reading my dossier, manuscripts, and this dissertation. Much of my professional development is the result of his valuable feedback.

I was fortunate to work among many impressive graduate students in the Tsapatsis group whose creativity has been inspiring. Particular recognition goes to Professor Dongxia Liu, Kumar Varoon, Dr. Pyungsoo Lee, and Xueyi Zhang who synthesized the MCM-36, ITQ-1, 3DOm-MFI, and SPP materials used throughout this dissertation, respectively. An enormous amount of thanks goes to Marta Navarro, who fortuitously came to Minneapolis as a visiting student in my final year of graduate school. The work in Chapter 5 would not have been possible without her ability to consistently synthesize beautiful silicalite-1 crystals. I would also like to thank the Bhan group members, especially my fellow "first Bhan students," Samia Ilias, Ian Hill, Hsu Chiang, and Mark Mazar. Graduate school would have been much less fun without them.

Several excellent undergraduate students contributed to the work presented here. I would like to acknowledge Joshua Kranz, Ian Babineau, Yasmine Guefrachi, and David Ford, who were not only incredibly helpful in lab, but also greatly enriched my graduate school experience.

Thanks are also due to the students, faculty, and staff of CEMS who make it such a wonderful place to do research. I felt at home in the department when I first visited as a prospective student, and that feeling has stayed with me for the last 5 years.

I would like to thank my amazing friends and fiancé, Brian, who have all been honest and encouraging sounding boards as I have navigated the challenges of life and graduate school. Finally, I would like to thank my family for their continuous support, particularly during my graduate school adventure. There are no words to express my deep gratitude to them.

To my family

Abstract

The ability of zeolites to discriminate between molecules on the basis of size and functionality gives them the potential to be effective adsorbents and membrane materials for purification of biomass-derived chemicals and fuels. Since molecules from biomass are polyfuntional and non-volatile, it is necessary to decouple the interactions that drive aqueous adsorption of oxygenates onto zeolites in order to develop efficient zeolite-based separations for biomass processing. In this dissertation, the roles of adsorbent structural and chemical composition and adsorbate functionality are explored through the systematic development of aqueous and vapor adsorption isotherms of C_2-C_6 oxygenates on small (FER), medium (MWW, MFI, BEA), and large (MOR, FAU) pore zeolites as well as on hierarchical microporous-mesoporous materials (MCM-36, 3DOm-MFI, and SBA-15).

Ambient temperature Henry's constants (K_{ads}) for aqueous diol and triol adsorption on silicalite-1 (aluminum-free MFI) increase exponentially with carbon number demonstrating that confinement of the adsorbate in the zeolite pores is a primary driving force for adsorption. This conclusion is supported by a monotonic decrease in propylene glycol K_{ads} values with an increase in adsorbent pore size, and by a comparison of propylene glycol K_{ads} values on MWW and MFI and their hierarchical counterparts (MCM-36 and 3DOm-MFI, respectively) that shows that propylene glycol preferentially adsorbs in the micropores of hierarchical materials.

A comparison of diol and triol adsorption on silicalite-1 demonstrates that increasing the number of hydroxyl groups causes a decrease in adsorption affinity, and this phenomenon is probed by comparing Henry's constants for aqueous adsorption of C_3 polyfunctional molecules onto zeolites with their octanol-water partition coefficients, K_{ow}, which were calculated using the prevalent ClogP group contribution method. It was found that K_{ads} increases linearly with K_{ow} for these adsorbates on H-ZSM-5 (aluminum-containing MFI), FAU, BEA, and ITQ-1 (MWW) at 278 K regardless of interactions in the bulk phase as measured by the solution activity coefficient. Exceptions to the correlation established between K_{ads} and K_{ow} are the adsorption of 1,2,ω-triols with carbon number greater than three on H-ZSM-5 and adsorption of all oxygenates studied on FER, which we postulate is due to a shift in the adsorption configuration with adsorbate/zeolite structure which cannot be captured by K_{ow} alone.

The effect of zeolite defects on oxygenate adsorption was isolated through the development of vapor and aqueous adsorption isotherms on silicalite-1 materials that vary in structural and surface properties. Silicalite-1 crystals prepared through alkaline-synthesis, alkaline synthesis with steaming post-treatment, and fluoride synthesis routes are confirmed as crystalline MFI by SEM and XRD and are shown to contain ~8.5 to 0 silanol defects per

unit cell by ^{29}Si MAS, ^{1}H MAS, and ^{1}H-^{29}Si CPMAS NMR. A hysteresis in the Ar 87 K adsorption isotherm at 10^{-3} P/P_0 evolves with a decrease in silanol defects, and, through features in the XRD and ^{29}Si MAS NMR spectra, it is postulated that the hysteresis is the result of an orthorhombic-monoclinic symmetry shift with decreasing silanol defect density. Gravimetric and aqueous solution measurements reveal that propylene glycol adsorption at 333 K is promoted by silanol defects, with a maximum 20-fold increase observed for aqueous adsorption in the Henry's Law regime with an increase from ~0 to 8.5 silanols per unit cell. A comparison of vapor and aqueous propylene glycol adsorption on defect-free silicalite-1 at 333 K, both of which exhibit the Type V character, indicates that water enhances adsorption by a factor of 2 in the Henry's Law regime, which is in agreement with simulations reported in the literature. K_{ads} values for aqueous C_2-C_4 polyol adsorption at 298 K are shown to have a linear dependence on the silanol defect density, which indicates that these molecules preferentially interact with silanol defects.

CONTENTS

Acknowledgements **i**

Dedication **ii**

Abstract **iii**

Table of Contents **v**

List of Tables **viii**

List of Figures **x**

1 Introduction **1**

1.1 Motivation 1

1.2 Zeolite Pore Size and Adsorption 3

1.3 Adsorbate Functionality and Adsorption 4

1.4 System Temperature and Adsorption 5

1.5 Zeolite Defects and Adsorption 6

2 Driving Forces for Adsorption of Polyols onto Zeolites from Aqueous Solutions **7**

2.1 Introduction 7

2.2 Methods 9

2.2.1 Materials 9

2.2.2 Chromatography 11

2.3 Results and Discussion 11

2.3.1 Confinement Effects 11

2.3.2 Shape Selectivity Effects 18

2.3.3 Effects of Brønsted Acid Sites 20

2.3.4 Effects of Adsorbate Hydroxyl Groups 21
2.4 Conclusions 24

3 Correlations for Adsorption of Oxygenates onto Zeolites from Aqueous Solutions 26
3.1 Introduction 26
3.2 Methods 28
3.2.1 Adsorption Experiments 28
3.2.2 Computation of Octanol-Water Partition Coefficients (K_{ow}) 29
3.3 Results and Discussion 30
3.3.1 Effect of Adsorbate Functionality 30
3.3.2 Correlating K_{ads} for Polyfunctional Adsorbates 31
3.3.3 Effect of Solution Thermodynamics 34
3.3.4 Effect of Zeolite Structure 37
3.4 Conclusions 41
3.5 Supporting Information 42
3.5.1 Extracting K_{ads} for C_6 Polyfunctional Adsorbates 42

4 Temperature Effects on Adsorption of Oxygenates onto Zeolites from Aqueous Solutions 46
4.1 Introduction 46
4.2 Methods 47
4.3 Results and Discussion 47
4.3.1 Effect of Temperature on Adsorption 47
4.3.2 Calculating ΔH_{ads} from Aqueous Solution Adsorption Isotherms . . 52
4.3.3 Calculating ΔS_{ads} from Aqueous Solution Adsorption Isotherms . . 55
4.4 Conclusions 58
4.5 Supporting Information 58
4.5.1 Relationship between Solution Excess Enthalpy (H^E) and the Heat of Mixing (ΔH_{mixing}) 58
4.5.2 Errors Associated with van't Hoff Plot Normalization 59
4.5.3 Design of Aqueous Solution Calorimetry Experiments 59

5 Probing the Relationship between Silanol Defects, Silicalite-1 Symmetry, and Polyol Adsorption Properties 63
5.1 Introduction 63
5.2 Methods 65
5.3 Results and Discussion 68

5.3.1 Effect of Synthesis and Steaming Conditions on Zeolite Structure and Defect Density 68
5.3.2 Effect of Defects on Vapor Propylene Glycol Adsorption 73
5.3.3 Comparison of Vapor and Aqueous Propylene Glycol Adsorption . . 75
5.3.4 Correlating K_{ads} for Polyol Adsorption from Aqueous Solutions with Silanol Defect Concentration 78
5.4 Conclusions 81
5.5 Supporting Information 82
5.5.1 ^{1}H-^{29}Si CPMAS and ^{1}H MAS NMR Data for the Silicalite-1 Materials 82
5.5.2 Comparison of Vapor Propylene Glycol Adsorption on Si[F] with Simulations 85
5.5.3 Effect of Solution Volume Change on Aqueous Solution Adsorption Measurements 86
5.5.4 Calculation of Partial Pressures from Aqueous Solution Concentrations 90
5.5.5 Effect of Non-Ideal Solution Interactions on K_{ads} 97

6 Future Directions **99**

Bibliography **101**

A Mass Transfer Modeling of Adsorption Kinetics on Zeolites **111**

B XRD Study of Hydroxymethylfurfural Adsorption on Silicalite-1 **119**

C List of Pure Silica Zeolite Analogues **124**

LIST OF TABLES

2.1 Chemical composition of adsorbents. 10

3.1 Structure and chemical composition of adsorbents 28
3.2 Sources of log P computational methods and comparison of results for the test set of experimental values from the SRS PhysProp database 30
3.3 K_{ow} values for the adsorbates. 32
3.4 Molecules used to calculate RMSE values for the K_{ow} calculation methods. 42
3.5 K_{ow} values for the adsorbates from the XLogP3 and LogKow computational methods. 43

4.1 Enthalpies for propylene glycol and 1,3-propanediol adsorption on H-MFI and H-BEA reported in units of kJ mol^{-1}. 53
4.2 Entropies for propylene glycol and 1,3-propanediol adsorption on H-MFI and H-BEA reported in units of J mol^{-1} K^{-1}. 55
4.3 Vapor phase molar entropy values reported by NIST WebBook 57

5.1 Summary of the synthesis methods, material treatments, and structural and chemical characterization data for the silicalite-1 adsorbents. 65
5.2 Comparison of propylene glycol K_{ads} values calculated with and without a solution volume change. 92
5.3 Comparison of 1,2-butanediol K_{ads} values calculated with and without a solution volume change. 92
5.4 Comparison of ethylene glycol K_{ads} values calculated with and without a solution volume change. 93
5.5 Wilson equation parameter values used to calculate activity coefficients. . . 95

B.1 HMF concentrations used in XRD measurements 120

C.1 Zeolites which can be synthesized in pure silica form 124

LIST OF FIGURES

1.1 General routes for synthesis of commodity chemicals from fossil and renewable feedstocks[1] 2
1.2 Unit cells for the (a) MFI, (b) FER, and (c) BEA structures 3
1.3 Inorganic adsorbents (a) SBA-15, (b) MCM-36, and (c) 3DOm-MFI that contain micropores and mesopores 4
1.4 Relationship between adsorption affinity (K_{ads}) and polyol functionality on zeolites 5
1.5 (a) Schematic of non-bonding and vacancy silanol defects in a siliceous zeolite framework and (b) the relationship between K_{ads} and silicalite-1 silanol defect density 6

2.1 Adsorption isotherms at 298 K for 1,2-butanediol (■), propylene glycol (●), and ethylene glycol (▲) on MFI silicliate-1. Solid lines are from unweighted least squares linear regressions. Dashed lines represent 95% confidence intervals. 12
2.2 Adsorption isotherms at 298 K for 1,2-butanediol (■), propylene glycol (●), and ethylene glycol (▲) on BEA CP811C-300. Solid lines are from unweighted least squares linear regressions. Dashed lines represent 95% confidence intervals. 13
2.3 Adsorption isotherms at 298 K for 1,2-butanediol (■), propylene glycol (●), and ethylene glycol (▲) on MWW MCM-22. Solid lines are from unweighted least squares linear regressions. Dashed lines represent 95% confidence intervals. 14
2.4 K_{ads} versus 1,2-diol carbon number for MFI silicalite-1, BEA CP811C-300, and MWW MCM-22 at 298 K. Solid lines are from unweighted least squares linear regressions. 14
2.5 Adsorption isotherms at 298 K for propylene glycol on MFI (■), BEA (●), MOR (▲), and FAU (◇) with Si/Al∼40. Solid lines are from unweighted least squares linear regressions. Dashed lines represent 95% confidence intervals. 15

2.6 Adsorption isotherms at 298 K for propylene glycol on MFI (■), BEA (●), MOR (▲), and FAU (◇) with Si/Al∼10. Data points for FAU and MOR represent average values. Solid lines are from unweighted least squares linear regressions. Dashed lines represent the 95% confidence interval for MFI. Dotted lines represent the 95% confidence interval for BEA. 16

2.7 Adsorption isotherms at 298 K for propylene glycol on mesoporous materials MCM-36 (□), 3DOm-MFI (○), and SBA-15 (△) and on ITQ-1 (■), the pure silica analogue of MWW, and MFI CBV28014 (●). Solid lines are from unweighted least squares linear regressions for the mesoporous materials. Dotted lines are unweighted least squares linear regressions for ITQ-1 and MFI. Dashed lines represent 95% confidence intervals for the mesoporous materials. 17

2.8 K_{ads} 3DOm-MFI versus smallest accessible zeolite pore diameter for propylene glycol on the MWW, MFI, BEA, MOR, and FAU zeolite frameworks and mesoporous materials MCM-36, 3DOm-MFI, and SBA-15. 18

2.9 Adsorption isotherms at 298 K for 1,2-hexanediol (▼), 1,2-butanediol (■), propylene glycol (●), 1,3-propanediol (◇), and ethylene glycol (▲) on FER CP914. Solid lines are from unweighted least squares linear regressions. Dashed lines represent 95% confidence intervals. 19

2.10 K_{ads} versus diol carbon number for 1,ω-diols (●) and 1,2-diols with carbon number greater than 3 (■) on FER CP914 at 298 K. Solid lines are from unweighted least squares linear regressions. 20

2.11 Adsorption isotherms at 298 K for 1,2,6-hexanetriol (□), 1,2,4-butanetriol (○), glycerol (△), 1,2-hexanediol (■), and 1,3-propanediol (●) on MFI silicliate-1. Solid lines are from unweighted least squares linear regressions of the triols. Dotted lines are from unweighted least squares linear regressions of the diols. Dashed lines represent 95% confidence intervals for the triols. 22

2.12 K_{ads} versus carbon number for 1,2-diols (■), 1,2,ω-triols (●), and 1,3-propanediol (▲) on MFI silicalite-1 at 298 K. Solid lines are from unweighted least squares linear regressions. 23

3.1 Adsorption isotherms at 278 K for hydroxyacetone (△), propylene glycol (▲), dihydroxyacetone (□), glycerol (■), and glyceraldehyde (◧) on H-ZSM-5. Solid lines represent least-squares linear regressions. Dashed lines represent 95% confidence intervals. 31

3.2 Adsorption isotherms at 278 K for hydroxyacetone (△), propylene glycol (▲), dihydroxyacetone (□), glycerol (■), and glyceraldehyde (◧) on BEA. Solid lines represent least-squares linear regressions. Dashed lines represent 95% confidence intervals. 32
3.3 Adsorption isotherms at 278 K for hydroxyacetone (△), propylene glycol (▲), dihydroxyacetone (□), glycerol (■), and glyceraldehyde (◧) on FAU. Solid lines represent least-squares linear regressions. Dashed lines represent 95% confidence intervals. 33
3.4 Adsorption isotherms at 278 K for hydroxyacetone (△), propylene glycol (▲), dihydroxyacetone (□), glycerol (■), and glyceraldehyde (◧) on ITQ-1. Solid lines represent least-squares linear regressions. Dashed lines represent 95% confidence intervals. 34
3.5 Measured K_{ads} versus K_{ow} on MFI CBV28014 at 278 K for carbonyl-containing molecules (▲), diols (■), and 1,2,ω-triols (● and ●). The solid line represents the least-squares linear regression on the black data points. Diol $K_{ads,intrinsic}$ values (■) obtained by decoupling the solution activity coefficients from the measured water-zeolite partition coefficients. 35
3.6 Measured K_{ads} versus K_{ow} for the carbonyl-containing adsorbates and their polyol counterparts on FAU, BEA, and ITQ-1 at 278 K. Solid lines represent least-squares linear regressions. (Inset at top) K_{ads}-K_{ow} correlation slopes versus pore size for FAU, BEA, H-ZSM-5, and ITQ-1. 39
3.7 Adsorption isotherms at 278 K for hydroxyacetone (△), propylene glycol (▲), dihydroxyacetone (□), and glycerol (■), on FER. Glyceraldehyde adsorption was negligible. Solid lines represent least-squares linear regressions. Dashed lines represent 95% confidence intervals. 40
3.8 Measured K_{ads} versus K_{ow} for the carbonyl-containing adsorbates (♢), their polyol counterparts (♦), and other 1,2- (●) and 1,ω−diols (○) on FER at 278 K. Solid lines represent least-squares linear regressions. Dashed line represents the correlation found on ITQ-1. 41
3.9 Adsorption isotherms at 278 K for ethylene glycol (●), 1,3-propanediol (▲), 1,2-butanediol (□), and 1,2,4-butanetriol (◧) on H-ZSM-5. Solid lines represent least-squares linear regressions. Dashed lines represent 95% confidence intervals. 43
3.10 Adsorption isotherms at 278 K for 1,2-hexanediol (■) and 1,2,6-hexanetriol (◧) on H-ZSM-5 and 1,2-hexanediol (□) on FER. Solid lines represent Langmuir isotherms calculated using parameters obtained from Langmuir linear regressions of the data. 44

3.11 Adsorption isotherms at 278 K for ethylene glycol (●), 1,3-propanediol (▲), and 1,2-butanediol (□) on FER. Solid lines represent least-squares linear regressions. Dashed lines represent 95% confidence intervals. 45

4.1 Adsorption isotherms for propylene glycol on H-MFI at 278 (■), 283 (●), 288 (◀), 293 (◆), 298 (▶), and 303 (▲) K. Solid lines represent least-squares linear regressions. 48
4.2 Adsorption isotherms for propylene glycol on H-BEA at 278 (■), 283 (●), 288 (◀), 293 (◆), 298 (▶), and 303 (▲) K. Solid lines represent least-squares linear regressions. 49
4.3 Adsorption isotherms for 1,3-propanediol on H-MFI at 278 (■), 283 (●), 288 (◀), 293 (◆), 298 (▶), and 303 (▲) K. Solid lines represent least-squares linear regressions. 49
4.4 van't Hoff plots for propylene glycol transfer to H-MFI (■) and H-BEA (■) from aqueous solutions when T_1 is set as 278 K. Solid lines represent least-squares linear regressions and dashed lines represent 95% confidence intervals. 50
4.5 van't Hoff plot for 1,3-propanediol transfer to H-MFI (■) from aqueous solutions when T_1 is set as 278 K. Solid lines represent least-squares linear regressions and dashed lines represent 95% confidence intervals. 51
4.6 Enthalpies and entropies for transfer of propylene glycol (left) and 1,3-propanediol (right) onto H-MFI and H-BEA from aqueous solutions. 51
4.7 Proposed thermodynamic cycle for extraction of ΔH_{ads} for propylene glycol (PG) 52
4.8 van't Hoff plots for propylene glycol transfer to H-MFI (■) and H-BEA (■) when T_1 is set as 293 K. Solid lines represent least-squares linear regressions. 60
4.9 van't Hoff plot for 1,3-propanediol transfer to H-MFI (■) when T_1 is set as 293 K. The solid line represents a least-squares linear regression. 60

5.1 SEM images of the a) Si[F], b) Si[OH], c) S1, and d) S2 silicalite-1 crystals prepared using the conditions described in Table 5.1. 68
5.2 XRD of Si[OH], S1, S2, and Si[F]. Inset: Magnified view of Si[OH], S1, S2, and Si[F] XRD data compared with simulated monoclinic[2] and orthorhombic[3] MFI patterns. 69
5.3 ^{29}Si MAS NMR of Si[OH], S1, S2, and Si[F]. Inset: Magnified view of the ^{29}Si MAS NMR Q^3 peak at -103 ppm of Si[OH], S1, and S2. 71
5.4 Argon adsorption (open symbols) and desorption (closed symbols) on Si[OH], S1, S2, and Si[F] at 87 K. 72

5.5 Vapor propylene glycol adsorption on S1 and Si[F] at 333 K (logarithmic pressure scale). Inset: Data plotted on a linear pressure scale. Dashed lines are a guide to the eye. 74
5.6 Aqueous propylene glycol adsorption isotherms on Si[OH], S1, and Si[F] 333 K (logarithmic concentration scale). Inset: Data plotted on a linear concentration scale. Dashed lines are a guide to the eye. 75
5.7 Aqueous and vapor adsorption isotherms for propylene glycol on Si[F] 333 K (logarithmic pressure scale). Inset: Data plotted on a linear pressure scale. Dashed lines are a guide to the eye. 77
5.8 Aqueous and vapor adsorption isotherms for propylene glycol on S1 at 333 K (logarithmic pressure scale). Top axis relates aqueous solution concentration to the pressure reported. Dashed lines are a guide to the eye. 78
5.9 Aqueous propylene glycol adsorption solutions on Si[OH], S1, S2, and Si[F] at 298 K. Solid lines represent least-squares linear regressions and dashed lines represent 95% confidence intervals. K_{ads} values are reported in mL solution/g zeolite. 79
5.10 Aqueous ethylene glycol adsorption on Si[OH], S1, S2, and Si[F] at 298 K. Solid lines represent least-squares linear regressions and dashed lines represent 95% confidence intervals. K_{ads} values are reported in mL solution/g zeolite. 80
5.11 Aqueous 1,2-Butanediol adsorption on Si[OH], S1, S2, and Si[F] at 298 K. Solid lines represent least-squares linear regressions and dashed lines represent 95% confidence intervals. K_{ads} values are reported in mL solution/g zeolite. 81
5.12 K_{ads} versus Si-OH/uc for aqueous 1,2-butanediol, propylene glycol, and ethylene glycol adsorption on Si[OH], S1, S2, and Si[F] at 298 K. Error bars represent 95% confidence intervals. Inset: Magnified view of K_{ads} values below 15 mL Solution/g Zeolite. 82
5.13 ^{1}H-^{29}Si CPMAS NMR of the Si[OH], S1, S2, and Si[F] silicalite-1 materials. 83
5.14 ^{1}H MAS NMR of the Si[OH], S1, S2, and Si[F] silicalite-1 materials. 84
5.15 Vapor propylene glycol adsorption on Si[F] at 333 K and computational adsorption data from Xiong *et al.* for vapor propylene glycol on defect-free silicalite-1 at 298 K[4]. Inset: Data on a linear pressure scale. Dashed lines are a guide to the eye. 85
5.16 Aqueous propylene glycol adsorption on Si[F] at 333 K. 89
5.17 Aqueous propylene glycol adsorption on S1 at 333 K. 89
5.18 Aqueous propylene glycol adsorption on Si[OH] at 333 K. 90

5.19 Aqueous propylene glycol adsorption on silicalite-1 at 298 K. Black points/lines are for the assumption that there is no volume change, green are for a volume change with propylene glycol adsorption, and red are for a volume change with propylene glycol adsorption and filling of the remaining pore volume with water. 91
5.20 Aqueous 1,2-butanediol adsorption on silicalite-1 at 298 K. Black points/lines are for the assumption that there is no volume change, and green points are for a volume change with polyol adsorption. 93
5.21 Aqueous ethylene glycol adsorption on silicalite-1 at 298 K. Black points/lines are for the assumption that there is no volume change, and green points are for a volume change with polyol adsorption. 94
5.22 Aqueous propylene glycol adsorption on Si[F] at 333 K with pressures calculated with an activity coefficient of one (ideal solution), non-unity activity coefficients, and with the method of Xiong *et al.*[4,5] 96
5.23 $K_{\text{ads,measured}}$ (closed symbols) and $K_{\text{ads,intrinsic}}$(open symbols) versus silanol defect density (Si-OH/uc) for aqueous 1,2-butanediol, propylene glycol, and ethylene glycol adsorption on Si[OH], S1, S2, and Si[F] at 298 K. Lines represent least-squares linear regressions. Error bars represent 95% confidence intervals. Inset: Magnified view of K_{ads} values below 15 mL Solution/g Zeolite. 98

A.1 Schematic of the sources and corresponding concentration profiles for zeolite mass transfer resistance. 112
A.2 Propylene glycol adsorption at 0.28 Pa (P/P_0=0.1) onto H-MFI at 303 K with respect to (a) time and (b) square root time. 115
A.3 Propylene glycol adsorption at 0.28 Pa (P/P_0=0.1) onto (a) 3DOm-MFI and (b) SPP at 303 K. 116
A.4 Ethanol adsorption at 110 Pa (P/P_0=0.1) onto H-MFI at 303 K 117

B.1 HMF adsorption data reported by Ranjan *et al.*[6] and calculated final concentrations and loadings for samples 1-6 used in this study. Dashed line represents a linearized Langmuir fit of the data from Ranjan *et al.* with K=2.487 [L solution per g HMF] and $[*]_0$=0.1862 [g HMF adsorbed per g zeolite] 121
B.2 Diffraction patterns for (a) the sample background and (b) raw samples without background correction. 121
B.3 Background corrected diffraction patterns for silicalite-1 with adsorbed HMF in the ranges of (a) 0-20° and (b) 8-13° 2θ. 122

CHAPTER

ONE

INTRODUCTION

1.1 Motivation

The most abundant and renewable source of carbon for fuel and chemical production is biomass. Nature produces 128 billion metric tons of carbohydrate biomass per year via photosynthesis, and only 3-4% is used by humans for both food and non-food purposes.[7] Although several potential routes to synthesize commodity chemicals from biomass exist (see Figure 1.1),[1] new separation technologies need to be developed to purify non-volatile and thermally sensitive biomass-derived oxygenates.[7] A zeolite adsorption or membrane separation process could be used to inexpensively obtain chemicals and fuels from biomass,[8] and the efficiency of both of these separation strategies is dependent on how biomass-derived oxygenates adsorb on the zeolite surface.[9,10]

Adsorption of oxygenates with functionality representative of the compounds encountered in biomass processing was systematically studied on different zeolite adsorbents to reveal the critical parameters for adsorption. Aqueous solution adsorption isotherms of C_2-C_6 oxygenates on zeolite adsorbents were developed using high performance liquid chromatography. Vapor isotherms for select adsorbate-zeolite systems were obtained using thermogravimetry. Structural and chemical characterization of the zeolites was accomplished using scanning electron microscopy (SEM), X-ray diffraction (XRD), argon and nitrogen physisorption, and magic angle spinning nuclear magnetic resonance spectroscopy (MAS NMR). Henry's constants, K_{ads}, were obtained from the adsorption isotherms and analyzed with respect to zeolite properties, adsorbate functionality, and system temperature to elucidate the roles of adsorbate-solvent, adsorbate-zeolite, and adsorbate-adsorbate interactions for adsorption.

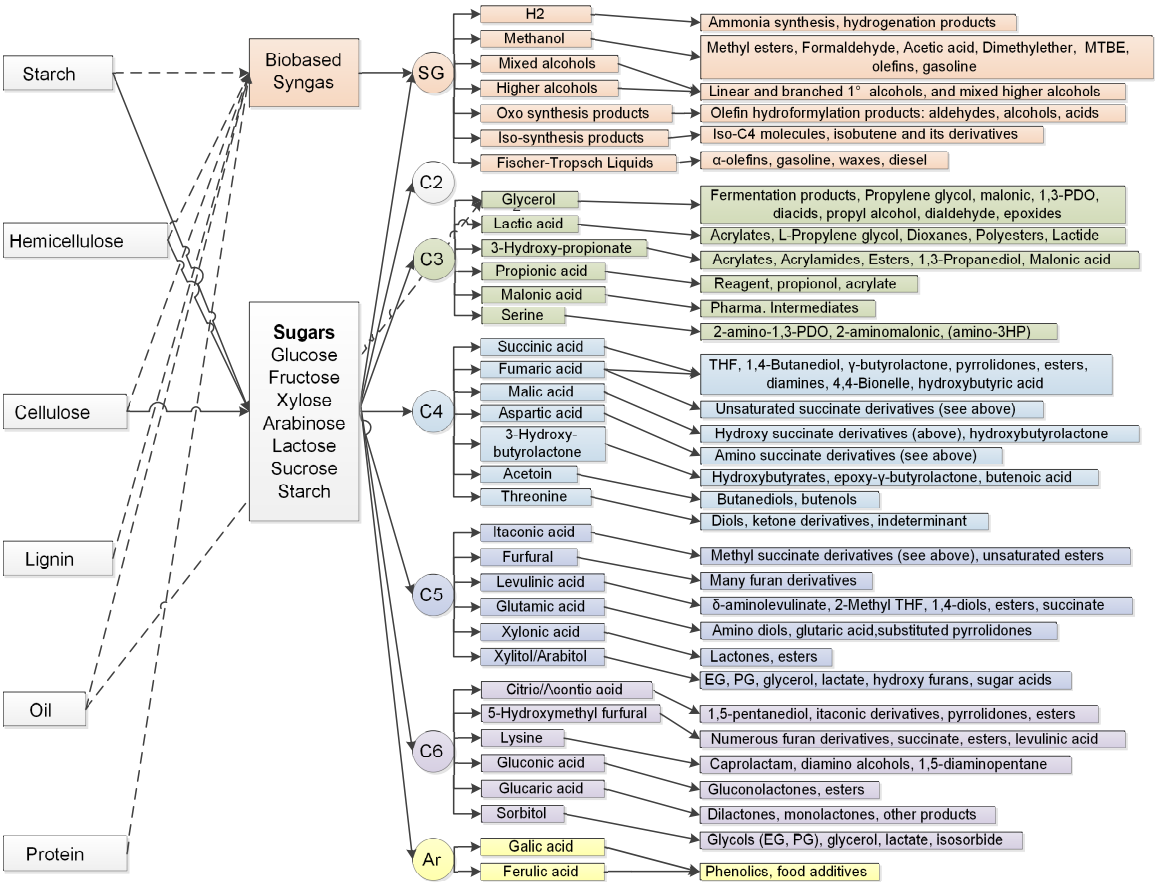

Figure 1.1: General routes for synthesis of commodity chemicals from fossil and renewable feedstocks[1]

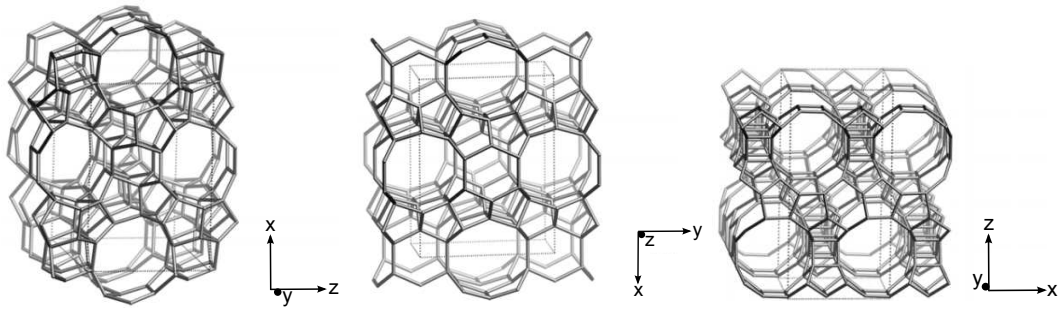

(a) (b) (c)

Figure 1.2: Unit cells for the (a) MFI, (b) FER, and (c) BEA structures

1.2 Zeolite Pore Size and Adsorption

Zeolites are a class of crystalline materials constructed from AlO_4 and SiO_4 tetrahedra. Each oxygen is shared between two tetrahedral atoms, either 2 silicon atoms or a silicon and aluminum atom, which gives a framework ratio of O/(Al+Si)=2.[11] The tetrahedra can be assembled into different building units, and the wide variety of ways in which these building units can interconnect has resulted in over 200 synthetic and natural zeolite frameworks.[12] As shown in Figure 1.2, the connections between building units create a network of Angstrom-sized pores which allow zeolites to discriminate between molecules with similar dimensions and functionality thereby leading to their use as highly selective catalysts and adsorbents.[13]

The pore size and shape dictates not only which molecules can diffuse through the zeolite framework, but also the strength of alkane adsorption. When the size of the alkane approaches the pore diameter, dispersion interactions between the adsorbate and the zeolite pore walls increase which results in stronger adsorption. Eder *et al.* compared adsorption of linear C_3-C_6 alkanes on zeolites using calorimetry and gravimetry to find that the heat of adsorption decreased in the sequence MFI>MOR>FAU which correlates with an increase in pore size.[14] Savitz *et al.* used calorimetry and gravimetry to study methane, ethane, and propane adsorption on high silica FER, TON, MFI, MTW, UTD-1, and FAU[15] and showed that the heat of adsorption for all alkanes investigated decreased from MFI to FAU which is in agreement with the observations of Eder *et al.*[14] While it has been shown that alkane adsorption strength decreases with zeolite pore size, the effect of the zeolite framework on adsorption of oxygenates has not been identified.

In Chapter 2, we present ambient temperature aqueous solution adsorption isotherms for propylene glycol, a C_3 polyol, on small (FER), medium (MWW, MFI, BEA) and large (MOR, FAU) pore zeolites as well as on ordered microporous-mesoporous materials (MCM-36, 3DOm-MFI, and SBA-15 as shown in Figure 1.3) to study the effect of zeolite pore size

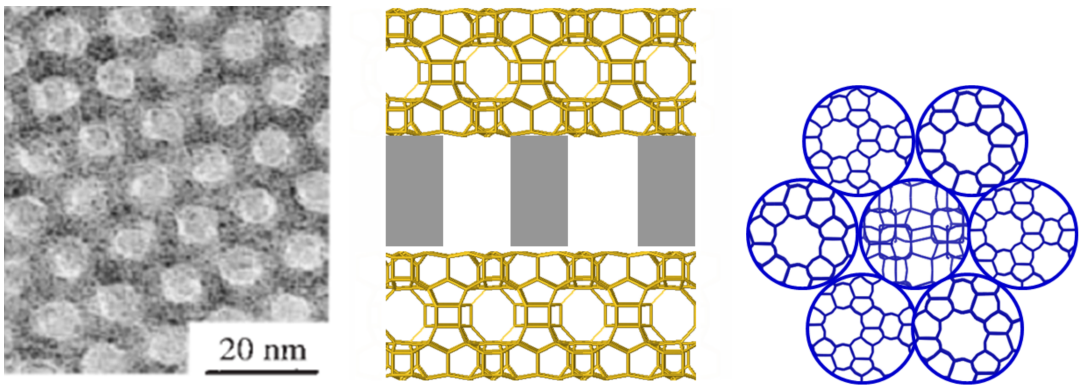

(a) (b) (c)

Figure 1.3: Inorganic adsorbents (a) SBA-15, (b) MCM-36, and (c) 3DOm-MFI that contain micropores and mesopores

on oxygenate adsorption. We extract the Henry's constants, K_{ads}, for these systems and show that dispersion forces are critical for polyol adsorption, and that propylene glycol preferentially adsorbs in the micropores of hierarchical materials due to increased confinement.

1.3 Adsorbate Functionality and Adsorption

Zeolite adsorption affinity is also a function of the adsorbate functionality and it is important to quantify this relationship in order to interpret zeolite reaction rates and separation selectivities.[16,17] A linear increase in adsorption enthalpy and the natural logarithm of Henry's constant with n-alkane chain length was observed experimentally and theoretically for several frameworks including MFI,[14,18–20] MOR,[14,21] FAU,[14,15,19,21] FER,[14,15] TON,[15] MTW,[15] UTD-1,[15] MWW,[22] and BEA.[21] Lee and Gorte[23] studied the heats of adsorption of methanol, ethanol, and propanol using microcalorimetry on MFI and found that they also increased linearly with carbon number which is in agreement with the findings of Thamm,[24] Dubinin *et al.* ,[25] and Nguyen *et al.*[26]

In this work, C_2-C_6 aqueous polyol adsorption isotherms on MFI are employed to explore the effect of polyol carbon number and hydroxyl group number on adsorption. The results and detailed discussion are presented in Chapter 2 which provide additional evidence for confinement as a primary driving force for adsorption as shown in Figure 1.4.

It is also identified in Chapter 2 that adsorption affinity decreases with an increase in polyol hydroxyl group number. The relationship between Henry's constants for C_3 polyfunctional molecules onto zeolites and their octanol-water partition coefficients, K_{ow}, is discussed in Chapter 3 to show that K_{ow} is a predictor for adsorption on MFI, FAU, BEA, and MWW regardless of interactions with water in the bulk phase. An exception to the

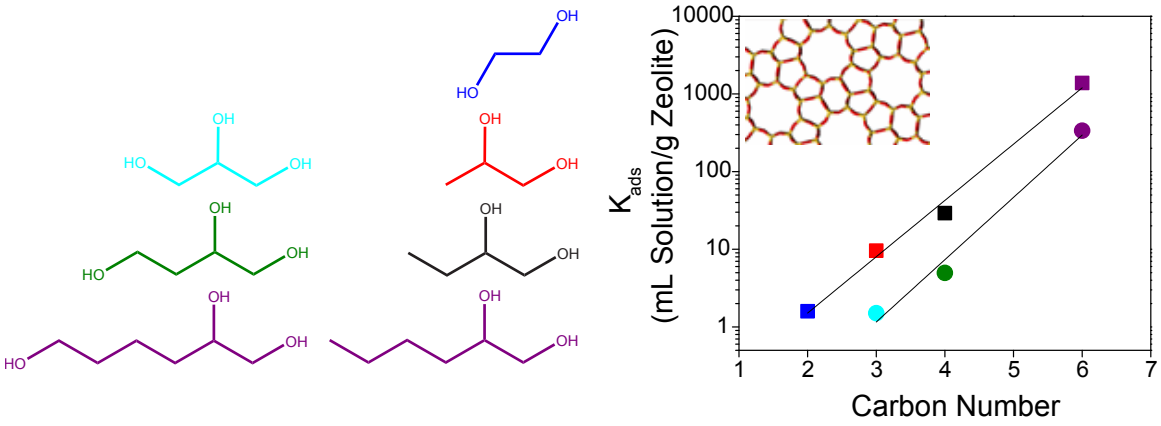

Figure 1.4: Relationship between adsorption affinity (K_{ads}) and polyol functionality on zeolites

K_{ads}-K_{ow} correlation was identified for the small pore zeolite, FER, which highlights the effect of size selectivity on polyol adsorption.

1.4 System Temperature and Adsorption

The heat of adsorption can be calculated using the van't Hoff equation from Henry's Law vapor adsorption isotherms at multiple temperatures for a particular adsorbate-zeolite system. The heat of adsorption can also be determined from binary solution adsorption isotherms by postulating a thermodynamic cycle. Ma and Yang utilized this approach with adsorption of thiophenic compounds from n-octane and hexadecane on NaY, 13X, and Cu(I)-Y zeolites.[27,28] The authors reported average thiophene adsorption enthalpies on NaY and Cu(I)-Y that were in agreement with the values obtained experimentally from vapor adsorption isotherms thus demonstrating the accuracy of their approach.

Aqueous solution adsorption isotherms for propylene glycol (1,2-propanediol) and 1,3-propanediol on MFI and BEA were obtained at temperatures ranging over 278-303 K and are reported in Chapter 4. It is shown that adsorption for these systems is an exothermic process, and in some cases, it can also be driven by an entropy increase. Heats of adsorption are extracted through a proposed thermodynamic cycle and are discussed relative to zeolite and adsorbate properties to again highlight the critical nature of dispersion forces on adsorption.

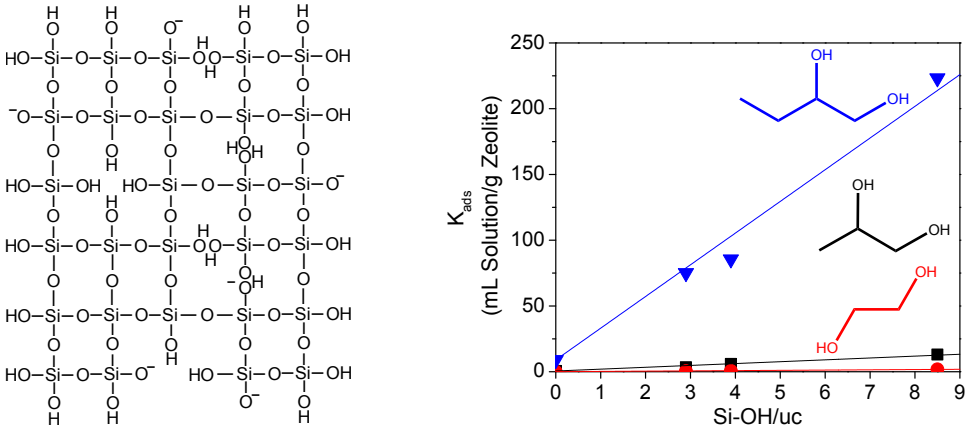

(a) (b)

Figure 1.5: (a) Schematic of non-bonding and vacancy silanol defects in a siliceous zeolite framework and (b) the relationship between K_{ads} and silicalite-1 silanol defect density

1.5 Zeolite Defects and Adsorption

So far the effects of zeolite pore size and molecule structure on oxygenate adsorption have been discussed, but the role of zeolite defects on adsorption remains unresolved. Several works have shown via gravimetry and simulations that silanol defect sites in the framework of high-silica zeolites (depicted in Figure 1.5(a)) increase water adsorption capacity due to weak electrotatic interactions.[17,29] Since alcohols can also participate in hydrogen bonding, the effect of silicalite-1 silanols on ethanol adsorption was probed in two gravimetric studies which yielded contradictory results. Chen *et al.* showed that removal of silicalite-1 defects suppresses vapor ethanol adsorption,[30] while Zhang *et al.* found that vapor ethanol adsorption is insensitive to the number of hydrophilic groups on the zeolite surface.[17]

In Chapter 5, polyol adsorption was measured on several silicalite-1 materials using gravimetry and aqueous solutions to systematically investigate the relationship between silanol defects and polyol adsorption affinity. Analyses of structural characterization data demonstrate that silicalite-1 materials that vary from ∼8.5 to 0 Si-OH defects per unit cell have been synthesized. Liquid and vapor adsorption data are compared to show that water promotes propylene glycol adsorption affinity and that polyols interact on a 1:1 basis with defect sites thereby enhancing adsorption by over an order of magnitude in the Henry's law regime.

CHAPTER

TWO

DRIVING FORCES FOR ADSORPTION OF POLYOLS ONTO ZEOLITES FROM AQUEOUS SOLUTIONS*

2.1 Introduction

Coal, natural gas, and crude oil are used to produce approximately 95% of the carbon-containing commodity chemicals, but many of these chemicals can also be manufactured from plant-based carbohydrates, lipids, and oils.[31] Propylene glycol, 1,3-propanediol, and ethylene glycol are diols, hydrocarbons functionalized with two hydroxyl (-OH) groups, which constitute some of the commodity chemicals that can be produced from fossil and renewable feedstocks. Fermentation is a potential route for obtaining diols from biomass, but in order to separate species in the reactor effluent using a traditional separation process, pretreatment of the effluent stream to remove unreacted sugars and proteins is required since these molecules are thermally sensitive and non-volatile.[32] Furthermore, the target product has a low vapor pressure, so a distillation step would be used to remove water, the primary component, resulting in an energy intensive and expensive unit operation which may account for 50-70% of the total production cost.[7,33] A membrane or adsorption separation process may be able to replace one or more of these separation steps, making production of diols using renewable feedstocks a viable synthetic route. Zeolitic materials are potential candidates in this application due to their high pressure and temperature stability, selectivity, and flux.[34]

The ability of zeolites to discriminate alkanes of varying length and degree of branching has already made their use prevalent in petrochemical processes such as fluid catalytic cracking,[35] isomerization,[36,37] and alkylation.[38] Earlier studies have identified that alkane adsorption in zeolites is predominantly a function of three interactions: van der Waals forces between the zeolite pore and the adsorbate, electrostatic interactions between the adsorbate

*Reported from Mallon, E. E., Bhan, A., and Tsapatsis, M. *Journal of Physical Chemistry B* **114**(5), 1939-1945 (2010)

and Brønsted acid sites, and adsorbate-adsorbate interactions. It has been shown that the fit between the alkane and zeolite pore has the most significant effect on the enthalpy and entropy of alkane adsorption.[14,15,19,21,22,39] Theoretical and experimental studies have shown that Henry's constant, K_{ads}, increases exponentially with n- and iso-alkane carbon number for several zeolite frameworks including MFI,[14,19,20] MOR,[14,20,21] FAU,[14,15,19,21] FER,[15,39] TON,[15] MTW,[15] UTD-1,[15] MWW,[22] and BEA[20,21] due to an increase in dispersion forces with each additional carbon.

Since dispersion forces are a function of the fit between the adsorbate and zeolite pore, it was found by Eder *et al.* using calorimetry and gravimetry that the heat of adsorption of n- and iso- alkanes decreases in the sequence H-MFI>H-MOR>H-FAU correlating with an increase in pore size.[14] This trend was confirmed by Savitz *et al.* who used a Lennard-Jones 12-6 potential to calculate the heat of adsorption and Henry's constant for methane adsorption in pure silica analogues of the FER, TON, MFI, MTW, UTD-1, and FAU frameworks.[15] The authors obtained an average error of 8% for the enthalpies and 29% for the Henry's constants, between the simulated and experimental results, indicating again that confinement effects are the dominant contributor to the energy of adsorption for n-paraffins.

While extensive experimental and theoretical studies have led to well-defined structure-property correlations for the adsorption of linear and branched alkanes on zeolites, analogous relationships for the adsorption of oxygenated molecules have yet to be fully developed. Studies have shown that methanol adsorption is a function of both electrostatic interactions with Brønsted acid sites and van der Waals interactions with the pore walls. Ison and Gorte used gravimetric and spectroscopic techniques to show at an adsorbate pressure of 80 torr on H-ZSM-5 at ambient conditions that methanol hydrogen-bonds with the Brønsted acid site protons and with other methanol molecules thereby forming clusters.[40] Other studies confirmed this result, indicating that electrostatic interactions between Brønsted acid sites and the methanol –OH group control the location of the adsorbate within the zeolite structure.[41,42] The chemical make-up of the zeolite was shown to not only control the location of adsorbed methanol in MFI pores, but also to have a substantial effect on the heat of adsorption of C_1-C_3 alcohols using calorimetry. For all alcohols studied, the heat of adsorption for coverages less than 400 μmol g^{-1} increased by 50-60 kJ mol^{-1} from silicalite-1 to H-ZSM-5.[23] Although the chemical composition was demonstrated to contribute to the enthalpy of adsorption, confinement was also shown to have a significant effect; the heat of adsorption increased 15-20 kJ/mol for each additional carbon irrespective of aluminum content.[23]

Diol adsorption and permeation experiments have given some insight to the interactions that control adsorption for this class of oxygenates. Long *et al.* performed a gravimetric study of oxygenated molecules on pure silica MFI.[43] The authors noted that glycerol,

propylene glycol, and 1,3-propanediol have similar molecular volumes, but the maximum volume of glycerol adsorbed at saturation was one order of magnitude less than the diols which they attributed to an increase in hydrophilicity from the addition of a third hydroxyl group. Li *et al.* have reported results for pervaporation experiments with binary, ternary, and quaternary feeds of 1,3-propanediol, glycerol, glucose, and water across a variety of zeolite membranes at temperatures ranging from 308-328 K.[44–47] It was reported on the basis of these studies that 1,3-propanediol/water separation selectivities for all zeolite membranes were higher than the ratio of their volatilities (0.038) leading to the conclusion that interactions between 1,3-propanediol and water with the membrane are significant.[45] The authors found that 1,3-propanediol selectivity was greater than 1 only for siliceous (Si/Al>600) zeolites and that the highest selectivity was achieved with silicalite-1. It was also noted that the 1,3-propanediol permeate concentration was greater with silicalite-1 than with ZSM-5 (Si/Al=25) which led the authors to conclude that the removal of Brønsted acid sites creates a more hydrophobic surface which facilitates 1,3-propanediol transport through the zeolite pores.[45]

While the aforementioned reports in the literature discuss single-component adsorption of diols on zeolites at saturation loading and the permeation of polyols (hydrocarbons with multiple –OH groups) through zeolite membranes, no relationship between K_{ads} and chemical functionality of the adsorbate has been determined for polyol adsorption on zeolites. The aim of the results and analysis presented herein is to determine structure-property correlations for the adsorption of polyols on zeolites using gravimetry. Specifically, C_2-C_6 diol and triol adsorbates were used in these experiments to isolate the effects of carbon number and functionality on polyol adsorption. In addition, several zeolite frameworks and ordered mesoporous materials with varying Al content were selected as adsorbents to determine the effect of topology and chemical composition on polyol adsorption. We report that K_{ads} increases exponentially with carbon number for C_2-C_6 diols and triols due to an increase in dispersion forces. Our results also show that K_{ads} increases with decreasing pore size and is only weakly dependent on the number of Brønsted acid sites within the range studied emphasizing the dominant role of confinement for polyol adsorption.

2.2 Methods

2.2.1 Materials

All experiments were performed with protonated forms of the different zeolite frameworks. The Si/Al ratio for all zeolite adsorbents used in this study is presented in Table 2.1. FER, MFI, BEA, MOR, and FAU zeolites of varying aluminum content were procured in either their protonated or ammonium form from Zeolyst. Silicalite-1[48] and ITQ-1,[49] pure

silica analogues of the MFI and MWW frameworks, respectively, were synthesized using previously reported procedures. SBA-15 was synthesized using the 2-day aging procedure reported by Kruk *et al.*[50] 3DOm-MFI with a mesopore size of 10 nm was synthesized using the procedure developed by Fan *et al.*[51] and a ZSM-5 synthesis solution (Si/Al=50) prepared according to the method reported by Schmidt *et al.*[52] MCM-22(P) was synthesized in the Na^+ form according to the procedure used by Maheshwari *et al.*; MCM-36 was then obtained using room temperature swelling of MCM-22(P) as described by the authors.[53] This version of MCM-36 exhibits a high degree of structural preservation of the microporous layers compared to previously reported MCM-36 materials. The NH_4^+ form of MCM-22 was obtained via ion exchange with 1 N NH_4NO_3 at ambient conditions for 24 hours.[54] X-ray diffraction was used to confirm the structural integrity of all zeolite adsorbents. Zeolite samples (∼1.5 g) were treated under flowing dry air (Minneapolis Oxygen Industrial, Compressed Industrial Air; 1.67 cm^3 s^{-1}) from ambient temperature to 823 K at a rate of 0.2 K s^{-1}, holding at 823 K for 10 h, and subsequently cooling to ambient temperature.

Table 2.1: Chemical composition of adsorbents.

zeolite name	**framework**	**source**	**Si/Al**	**Al/uc**
CP914	FER	Zeolyst	29[a]	1.2
ITQ-1	MWW	Synthesis	∞	0
MCM-22	MWW	Synthesis	47	1.5
CBV2314	MFI	Zeolyst	13[a]	6.8
CBV8014	MFI	Zeolyst	43[a]	2.2
CBV28014	MFI	Zeolyst	140	0.7
silicalite-1	MFI	Synthesis	∞	0
CP814E	BEA	Zeolyst	12	4.9
CP811E-75	BEA	Zeolyst	48	1.3
CP811C-300	BEA	Zeolyst	100	0.6
CBV21A	MOR	Zeolyst	11[a]	4.0
CBV90A	MOR	Zeolyst	44[a]	1.1
CBV720	FAU	Zeolyst	15	12
CBV760	FAU	Zeolyst	30	6.2
3DOm-MFI	MFI/Meso	Synthesis	50	-
MCM-36	MWW/Meso	Synthesis	47	-
SBA-15	Micro/Meso	Synthesis	∞	0

[a] Si/Al determined using inductively coupled plasma-optical emission spectroscopy by Galbraith. All other Si/Al values from vendor or approximated from synthesis procedure

The adsorbates used for all results presented were in the liquid phase at ambient temper-

ature and atmospheric pressure. Aqueous solutions with a volume of 1 mL and concentrations ranging from 1 to 10 μmol mL^{-1} were prepared in closed glass vials. Approximately 100 mg of zeolite adsorbent was added to each vial and the zeolite-solution mixtures were stirred at 1200 rpm and ambient temperature until equilibration. Each solution was filtered with a 3 mL Monoject syringe fitted with a 0.2 micron GHP (polypropylene) syringe filter to remove the zeolite particles and the filtrate was prepared for analysis with liquid chromatography.

2.2.2 Chromatography

The filtrate concentrations were analyzed using an Agilent 1200 High Performance Liquid Chromatography (HPLC) system equipped with a refractive index detector (RID) and an autosampler. The autosampler removed 20 μL of sample from a single vial and injected the contents into a stream of 0.005 M sulfuric acid (H_2SO_4) in deionized water with a flow rate of 0.008 mL s^{-1}. The stream was passed through a Bio-Rad Aminex HPX-87H polystyrene packed column heated to 333 K at the inlet and 318 K at the outlet and the column pressure was maintained at 40-60 bar. The outlet stream was passed through a refractive index detector (RID) which was heated to 323 K. The RID signal output was recorded and plotted against time and the adsorbate peak was identified from the retention time. The relative signal intensities of the adsorbate and a glycerol or propylene glycol internal standard were used to determine the final concentration of each solution. The difference in the initial and final concentration of the adsorbate and the total volume of the solution was used to calculate the uptake of the adsorbate (note that it was assumed that the solution volume did not change with adsorption in this calculation as described in Section 5.5.3).

2.3 Results and Discussion

2.3.1 Confinement Effects

The adsorption isotherms for ethylene glycol, propylene glycol, and 1,2-butanediol in water on high Si/Al forms (47<Si/Al<∞) of the MFI, BEA, and MWW frameworks are shown in Figures 2.1-2.3. The amount adsorbed increases with increasing carbon number for MFI, BEA, and MWW which implies that confinement affects adsorption uptake at low diol loadings.

This hypothesis was further probed via analysis of the partition coefficients between the bulk and adsorbed phases (K_{ads}) for these systems. Values of K_{ads} were extracted from the adsorption isotherm data presented based on the following assumptions - it has been shown

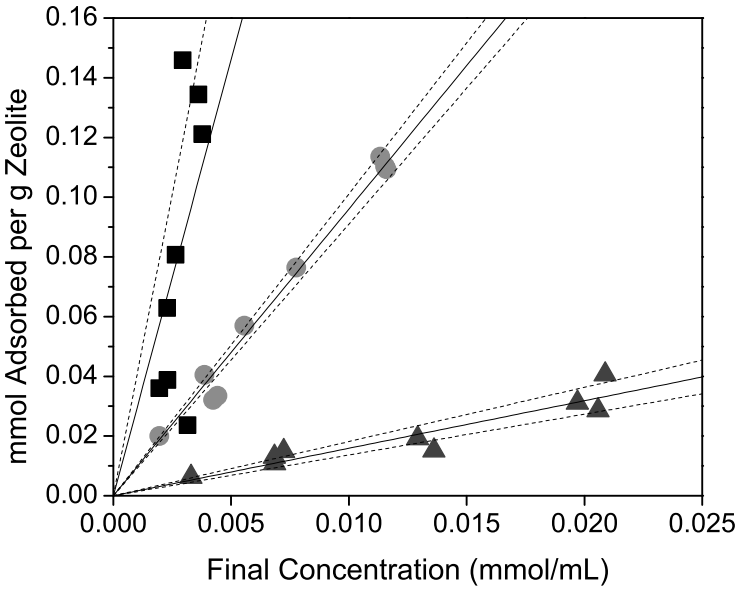

Figure 2.1: Adsorption isotherms at 298 K for 1,2-butanediol (■), propylene glycol (●), and ethylene glycol (▲) on MFI silicliate-1. Solid lines are from unweighted least squares linear regressions. Dashed lines represent 95% confidence intervals.

through gravimetric measurements that water adsorbs in MFI pores only at Brønsted acid sites[41,55,56] and at the silanol groups that arise at the external crystal surface and crystal defects.[23,57] Furthermore, on the basis of single and binary component adsorption studies done using gravimetry, calorimetry, and FTIR spectroscopy, it was shown that water adsorbs with a heat of adsorption of approximately 30 kJ mol^{-1} less than methanol,[23] and when methanol and water are co-fed onto a zeolite, methanol will displace water at Brønsted acid sites.[40] Based upon these experimental observations reported in the literature we assumed in our analysis that water-zeolite interactions are negligible. The solution concentrations used in these experiments (1 to 10 μmol mL^{-1}) are in the infinitely-dilute regime where the activity coefficients are approximately equal to unity.[58] Therefore, water-adsorbate interactions were also neglected and the adsorption isotherms presented herein were treated as single component isotherms. Due to these assumptions, the partition coefficients will be referred to as Henry's constants from this point forward.

It should also be noted that coverages for all data reported were below 4 molecules per unit cell (∼0.001 to 0.02 molecules per unit cell and less than 10% of the total micropore volume) which corresponds with an inflection in the isotherms for hexane, heptane, and C_4-C_7 2-methyl branched alkane adsorption in silicalite-l.[59,60] Smit and Maesen used

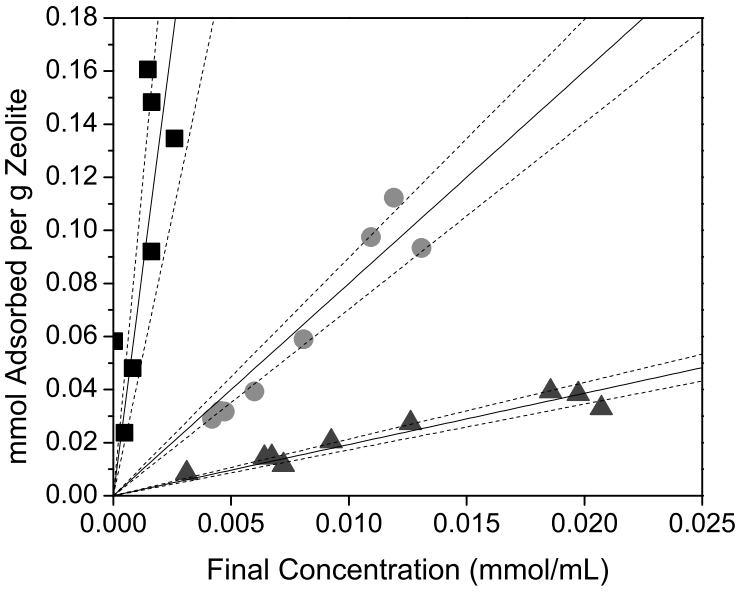

Figure 2.2: Adsorption isotherms at 298 K for 1,2-butanediol (■), propylene glycol (●), and ethylene glycol (▲) on BEA CP811C-300. Solid lines are from unweighted least squares linear regressions. Dashed lines represent 95% confidence intervals.

configurational-bias Monte Carlo (CBMC) simulations to show that the inflection point in hexane and heptane isotherms was due to "commensurate freezing." [59] Similarly, the inflection in the adsorption isotherm for C_4-C_7 2-methyl branched alkane adsorption in silicalite-1 was attributed to preferential adsorption of these bulkier molecules in the channel intersections at low pressures, and that adsorption in the pores, the secondary adsorption site, only occurs when adequate pressure in the bulk phase is achieved. [60] While isotherms with inflection points are typically modeled as dual-site Langmuir isotherms, and it is unknown if polyol adsorption isotherms contain this feature since full isotherms have not been obtained, the isotherms presented herein are for low pressures, when it is likely that the adsorbate molecules occupy one preferred adsorption site, and were therefore modeled as single-component single-site Langmuir isotherms. The data were then fit using least-squares linear regression and values for K_{ads} were determined from the slopes of the lines.

An exponential increase in K_{ads} with 1,2-diol carbon number on silicate-1, BEA, and MWW was noted (Figure 2.4) implying that the free energy of adsorption, ΔG_{ads}, increases linearly with carbon number for C_2-C_4 diols. As with alkane adsorption, this result implies that the energy of adsorption for diols increases by a fixed amount with each additional carbon, and, therefore, dispersion forces are critical for diol adsorption.

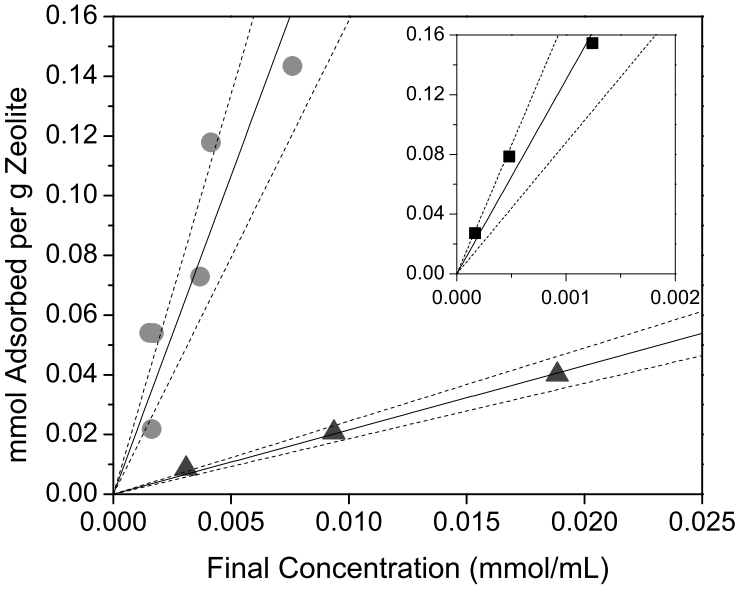

Figure 2.3: Adsorption isotherms at 298 K for 1,2-butanediol (■), propylene glycol (●), and ethylene glycol (▲) on MWW MCM-22. Solid lines are from unweighted least squares linear regressions. Dashed lines represent 95% confidence intervals.

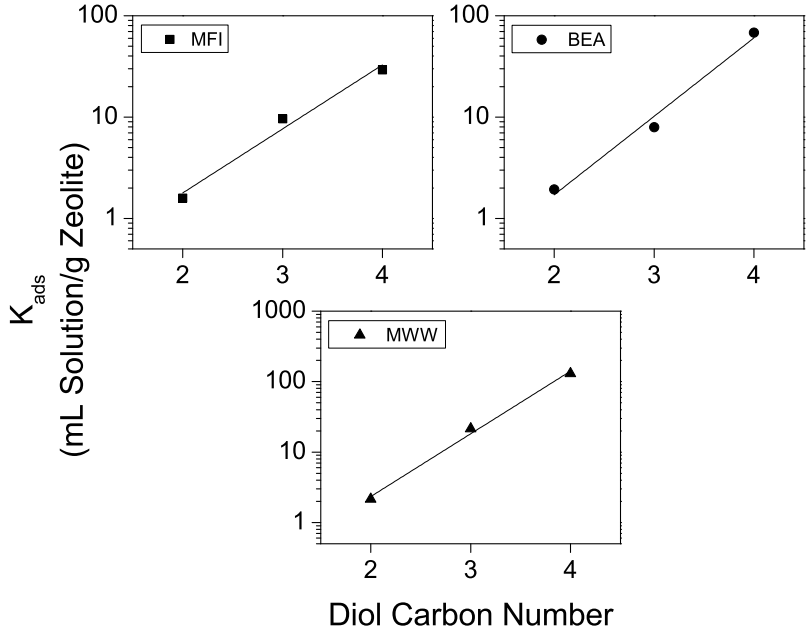

Figure 2.4: K_{ads} versus 1,2-diol carbon number for MFI silicalite-1, BEA CP811C-300, and MWW MCM-22 at 298 K. Solid lines are from unweighted least squares linear regressions.

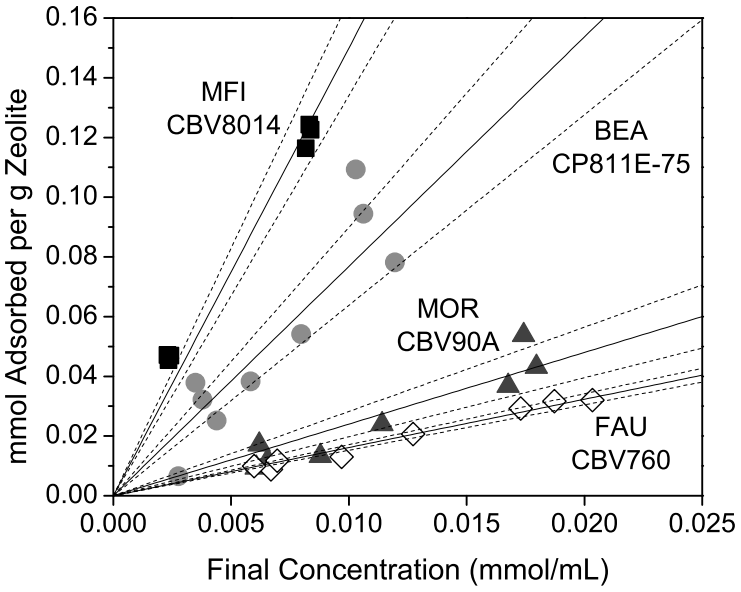

Figure 2.5: Adsorption isotherms at 298 K for propylene glycol on MFI (■), BEA (●), MOR (▲), and FAU (◇) with Si/Al∼40. Solid lines are from unweighted least squares linear regressions. Dashed lines represent 95% confidence intervals.

Since confinement is a function of the fit between the adsorbate and the zeolite pores, the dependency of K_{ads} for propylene glycol adsorption on the material topology was explored. Note that propylene glycol was chosen as the probe molecule since it is a current commodity chemical as well as an appropriate surrogate compound for biomass due its similar chemical functionality. Solutions of propylene glycol and water were adsorbed on different Si/Al ratios of the MFI, BEA, MOR, and FAU frameworks. The adsorption isotherms are grouped by Si/Al∼10 and Si/Al∼40 and are presented in Figures 2.5 and 2.6. Since the aluminum content per unit cell is comparable for the frameworks as shown in Table 2.1, these data demonstrate that the framework geometry has a strong effect on the amount of propylene glycol adsorbed.

Adsorption isotherms for propylene glycol on mesoporous materials MCM-36, 3DOm-MFI, and SBA-15 are shown in Figure 2.7. These are compared with the adsorption isotherms for the pure silica analogue of MWW, ITQ-1, and MFI CBV28014 (Si/Al∼140). It can be observed that MCM-36, which has the MWW micropore structure and 4.2 nm mesopores from silica pillaring between layers, and ITQ-1 have similar adsorption uptake at low concentrations of propylene glycol in water; the same relationship is apparent for propylene glycol adsorption in 3DOm-MFI (MFI micropores and 10 nm mesopores) and

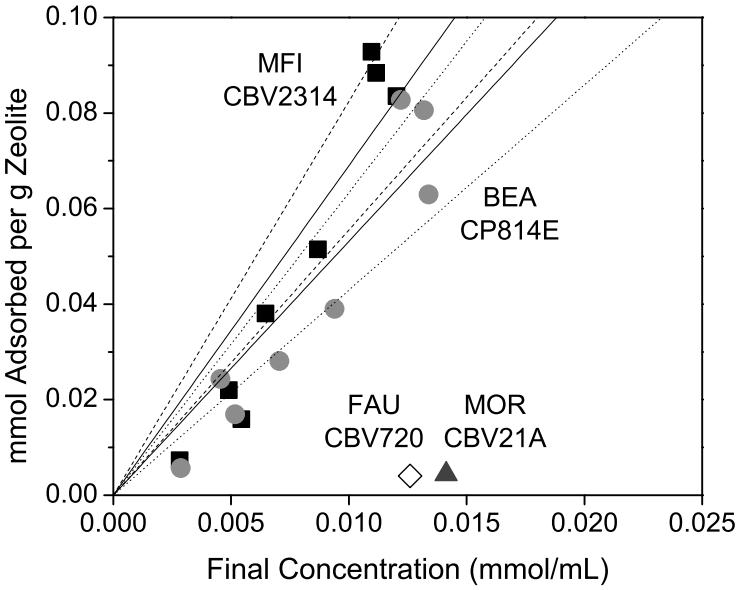

Figure 2.6: Adsorption isotherms at 298 K for propylene glycol on MFI (■), BEA (●), MOR (▲), and FAU (◇) with Si/Al∼10. Data points for FAU and MOR represent average values. Solid lines are from unweighted least squares linear regressions. Dashed lines represent the 95% confidence interval for MFI. Dotted lines represent the 95% confidence interval for BEA.

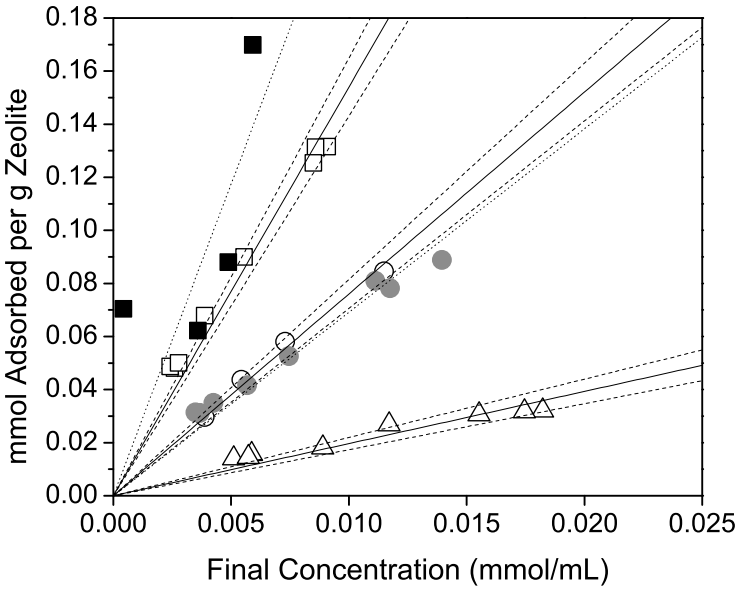

Figure 2.7: Adsorption isotherms at 298 K for propylene glycol on mesoporous materials MCM-36 (□), 3DOm-MFI (○), and SBA-15 (△) and on ITQ-1 (■), the pure silica analogue of MWW, and MFI CBV28014 (●). Solid lines are from unweighted least squares linear regressions for the mesoporous materials. Dotted lines are unweighted least squares linear regressions for ITQ-1 and MFI. Dashed lines represent 95% confidence intervals for the mesoporous materials.

MFI. This indicates that propylene glycol preferentially adsorbs in the micropores of these materials.

K_{ads} for propylene glycol adsorption on all Si/Al forms of the MWW, MFI, BEA, MOR, and FAU zeolite frameworks as well as the mesoporous materials MCM-36, 3DOm-MFI, and SBA-15 are plotted in Figure 2.8. The minimum accessible pore diameters were estimated from the unit cell structure of MWW, MFI, BEA, and FAU as reported by the International Zeolite Association.[12] Since it has been observed that straight alkanes with a carbon number greater than 4 preferentially adsorb in the 12 MR of MOR at saturation conditions,[61] it was assumed that the 8 MR ring pockets are inaccessible to propylene glycol and therefore the minimum pore dimension for MOR was taken to be 6.5 Å. MCM-36 and 3DOm-MFI were assigned minimum pore sizes corresponding to MWW and MFI, respectively, since propylene glycol adsorption on these materials resulted in isotherms comparable to their zeolite counterparts as shown in Figure 2.7. SBA-15 synthesized in the aforementioned procedure[50] contains micropores with an average pore diameter of 17 Å, so this value was taken as the minimum pore diameter.[62,63]

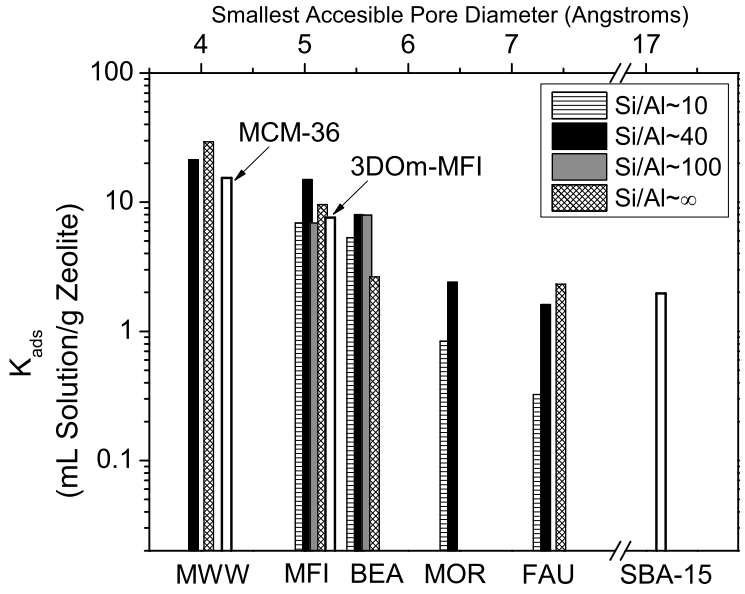

Figure 2.8: K_{ads} 3DOm-MFI versus smallest accessible zeolite pore diameter for propylene glycol on the MWW, MFI, BEA, MOR, and FAU zeolite frameworks and mesoporous materials MCM-36, 3DOm-MFI, and SBA-15.

It can be observed from the data reported in Figure 2.8 that K_{ads} decreases with increasing pore size for all zeolite frameworks and mesoporous materials explored. Taking into account the exponential dependence of K_{ads} on diol carbon number, it is likely that the decrease in K_{ads} with increasing pore size is caused by a decrease in dispersion forces.

2.3.2 Shape Selectivity Effects

While it has been noted that diol adsorption increases with carbon number on silicalite-1, MWW, and BEA, this trend is not found with FER (Figure 2.9). In an effort to better understand the cause of this result, adsorption isotherms for 1,2-hexandiol and 1,3-propanediol on FER were developed as shown as in Figure 2.9. Values for K_{ads} were obtained using the procedure described previously and are compared in Figure 2.10. It can be observed that K_{ads} increases exponentially with carbon number for C_3-C_6 1,2-diols, but ethylene glycol has a higher K_{ads} than propylene glycol. Also, it is found that K_{ads} for 1,3-propanediol is one order of magnitude greater than propylene glycol (1,2-propanediol).

Similar trends have been identified for linear and di-branched alkane adsorption in FER.[61,64] ^{13}C NMR and FT-Raman studies have shown that linear alkanes with 6 or more carbon atoms cannot access the 8 member ring channels of FER.[61] Pieterse *et al.* compared

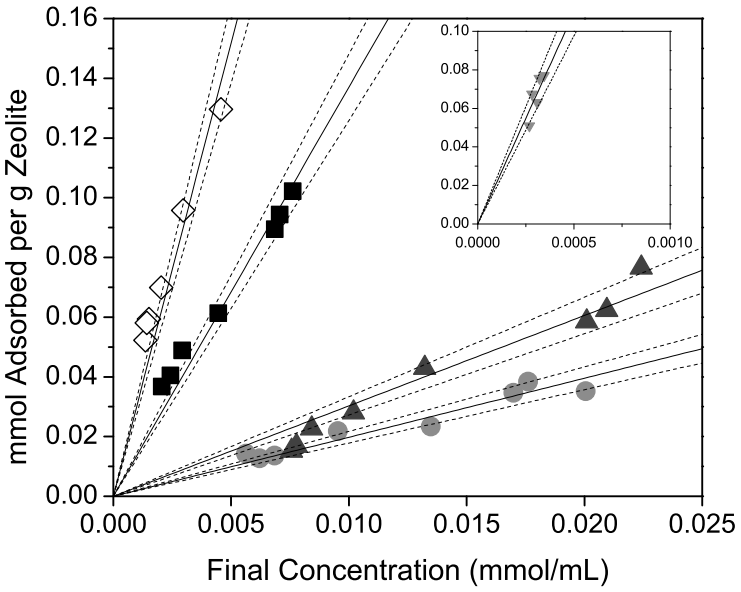

Figure 2.9: Adsorption isotherms at 298 K for 1,2-hexanediol (▼), 1,2-butanediol (■), propylene glycol (●), 1,3-propanediol (◇), and ethylene glycol (▲) on FER CP914. Solid lines are from unweighted least squares linear regressions. Dashed lines represent 95% confidence intervals.

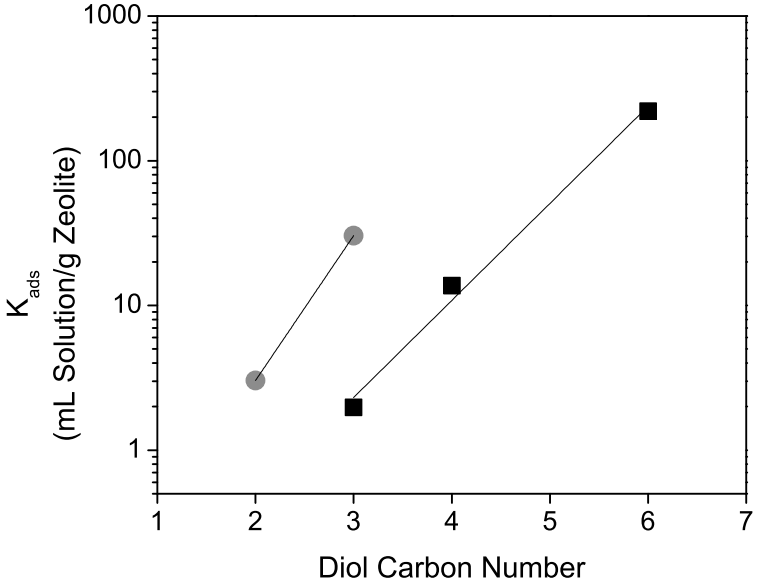

Figure 2.10: K_{ads} versus diol carbon number for 1,ω-diols (●) and 1,2-diols with carbon number greater than 3 (■) on FER CP914 at 298 K. Solid lines are from unweighted least squares linear regressions.

adsorption enthalpies between linear and di-branched alkanes in FER using gravimetry and calorimetry to find that the heat of adsorption decreases with an increase in branching.[64] The authors also noted using a combination of IR spectroscopic, gravimetric, calorimetric, and computational methods that the appended methyl groups inhibit the alkanes from fully entering the zeolite pores, and at coverages greater than 0.02 mmol per gram, 2,2-deimethylpentane and 2,2-dimethylhexane adsorb on the external crystal surface with the propyl and butyl groups pointing into the zeolite pores.[64] Since the data presented herein is for similar coverages (see Figure 2.9), it is hypothesized that adsorption of 1,2-diols with carbon numbers greater than 3 is hindered by the hydroxyl group on the secondary carbon but the hydrocarbon chains of the C_3-C_6 1,2-diols can penetrate the pores of FER leading to the observed exponential dependence of K_{ads} on carbon number. Also, it is proposed that 1,3-propanediol can fully diffuse into the pores of FER leading to greater values for K_{ads} than 1,2-propanediol

2.3.3 Effects of Brønsted Acid Sites

Henry's constants for propylene glycol adsorption on zeolites and mesoporous materials with varying aluminum content (Figure 2.8) can also be inspected to discern the effect of

the framework chemical composition on propylene glycol adsorption. From these data we note that a change in pore size from 4-7 Å results in a reduction of K_{ads} by an order of magnitude, but varying the aluminum content (and the synthesis method as shown in Table 2.1) results in an average standard deviation of less than 50% from the mean K_{ads} value for any given zeolite framework. This demonstrates that the fit between the adsorbate and zeolite pore is the most critical parameter for diol adsorption in zeolites at ambient temperature; the aluminum content for the range studied appears to only have a marginal effect.

A possible explanation for the weak dependence of K_{ads} on Si/Al ratio is a compensation effect. Eder *et al.* plotted the enthalpy of adsorption versus the entropy of adsorption for adsorption of C_3-C_6 n-alkanes on silicalite-1 and an aluminum containing MFI zeolite.[19] A comparison of the points corresponding to hexane show that both the enthalpy and entropy of adsorption increase with an increase in aluminum content, leading to approximately the same value of K_{ads} for both frameworks. It is possible that a similar compensation effect is occurring for polyol adsorption resulting in only a small change in K_{ads} with Si/Al ratio.

Despite being a weak dependence, the trend of K_{ads} on Si/Al ratio is clear - K_{ads} decreases with decreasing Si/Al ratio. It is possible that this decrease is from competitive adsorption with water, although the low aluminum content of the adsorbents (see Table 2.1,) and the observation that water adsorbs with a heat of adsorption ∼30 kJ mol^{-1} less than methanol[23], and is, therefore, displaced at Brønsted acid sites during co-adsorption with methanol,[40] indicates that this is unlikely to have a significant effect. Another possible cause of the decrease in K_{ads} with increasing aluminum content is partial blockage of the preferred adsorption sites of propylene glycol by the Brønsted acid site protons. Beerdsen *et al.* used configurational bias Monte Carlo (CBMC) simulations to identify that isobutane adsorption in MFI is inhibited by a decrease in Si/Al at pressures ranging from 10^{-3} to 10^{5} kPa at 296 K.[65] Henry's constants calculated by the authors also decreased as Si/Al decreased for all non-framework cations (cations balancing negatively charged framework oxygens) studied. The authors concluded that the non-framework cations, which mainly reside at the channel intersections, inhibit isobutane from fitting into the channel intersections where it preferentially adsorbs at low pressures, thereby decreasing K_{ads}. It is possible that diols also adsorb preferentially at channel intersections due to the appended hydroxyl groups, and, therefore, a decrease in Si/Al would result in a decrease in the available adsorption sites at low concentrations and a concomitant decrease in K_{ads}.

2.3.4 Effects of Adsorbate Hydroxyl Groups

The adsorption isotherms for glycerol, 1,2,4-butanetriol, and 1,2,6-hexanetriol in water on silicalite-1 are shown in Figure 2.11. As with the 1,2-diols, the amount adsorbed increases

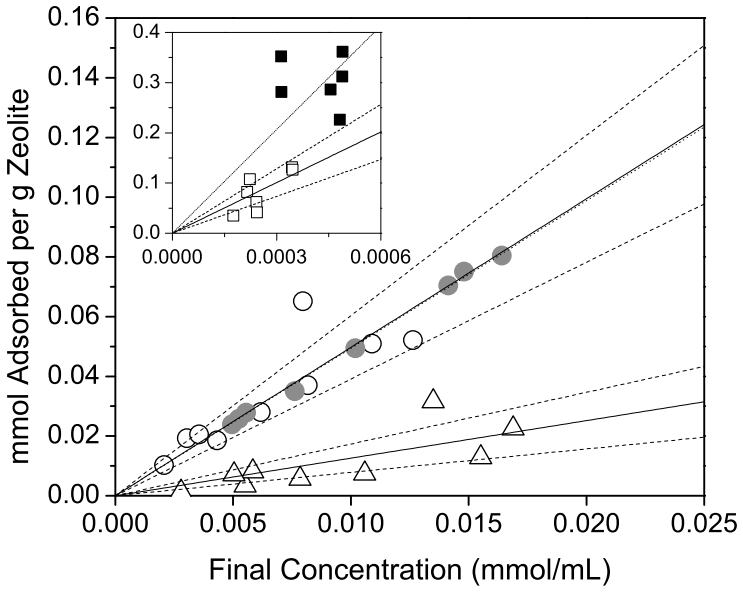

Figure 2.11: Adsorption isotherms at 298 K for 1,2,6-hexanetriol (□), 1,2,4-butanetriol (○), glycerol (△), 1,2-hexanediol (■), and 1,3-propanediol (•) on MFI silicliate-1. Solid lines are from unweighted least squares linear regressions of the triols. Dotted lines are from unweighted least squares linear regressions of the diols. Dashed lines represent 95% confidence intervals for the triols.

with increasing carbon number reaffirming confinement as the primary driving force for adsorption. Also shown in Figure 2.11 are the adsorption isotherms for 1,2-hexanediol and 1,3-propanediol. It can be observed from the isotherms there is a greater uptake of 1,2-hexanediol than 1,2,6-hexanetriol at low coverages. This indicates that the addition of an –OH group decreases the affinity for adsorption. It is also interesting to note that the adsorption isotherms of 1,3-propanediol and 1,2,4-butanetriol are collinear illustrating that increasing carbon number and decreasing hydroxyl number by the same amount may result in similar adsorption configurations in MFI.

A comparison of the K_{ads} values for propylene glycol (1,2-propanediol) and 1,3-propanediol in Figure 2.12 indicates that the location of the –OH groups does not have a significant effect on the strength of diol adsorption in silicalite-1. Based upon this result, we postulate that C_3 diols have similar configurations within the zeolite pores at low coverages regardless of the location of the hydroxyl groups.

The adsorption isotherms for C_3, C_4 and C_6 triols on silicalite-1 were also analyzed as single component single-site Langmuir isotherms allowing us to determine K_{ads}. A plot of K_{ads} versus carbon number for C_2-C_6 diols and triols shows that K_{ads} increases expo-

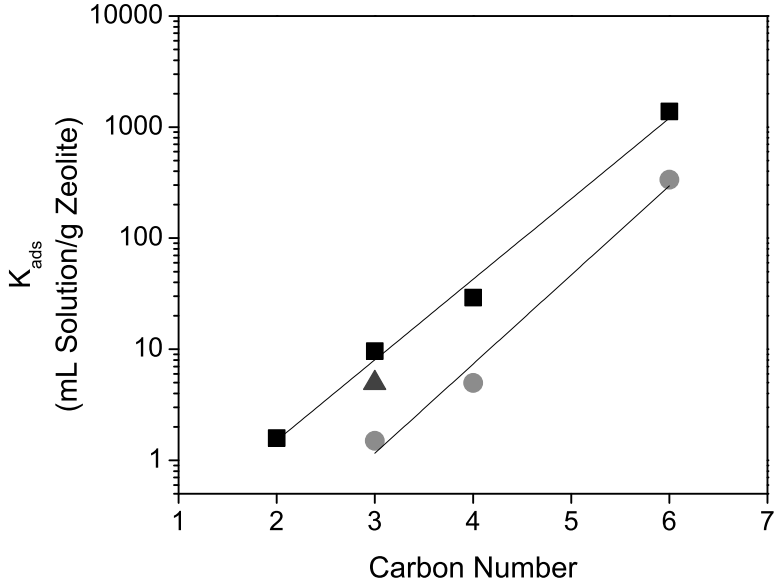

Figure 2.12: K_{ads} versus carbon number for 1,2-diols (■), 1,2,ω-triols (●), and 1,3-propanediol (▲) on MFI silicalite-1 at 298 K. Solid lines are from unweighted least squares linear regressions.

nentially with carbon number for both classes of adsorbates (Figure 2.12), and that K_{ads} for any triol is lower than the value for the diol with a corresponding number of carbons. The change in K_{ads} with the addition of an –OH group indicates that diols and triols have different adsorption configurations within the pore network.

Differences in triol and diol configurations can be hypothesized from the trends observed for n- and iso-alkane adsorption on MFI.[20,39] Denayer *et al.* used the pulse chromatographic technique to measure equilibrium adsorption coverages and found that on MFI the Henry's constant for a given carbon number alkane decreased with increased branching.[20] This result indicates a change in the preferred configuration of alkanes with an increase in branching. This was confirmed via Monte Carlo simulations by June *et al.* who found that n-hexane adsorbs in the pores of silicalite-1 with a heat of adsorption of 68 kJ mol^{-1} while 2- and 3-methyl pentane adsorb at the channel intersections with a 5 kJ mol^{-1} lower heat of adsorption.[66] The authors also found that K_{ads} values for methylpentanes are lower than those for n-hexane, indicating that the configuration of the branched alkanes in the channel intersections results in weaker interactions with the pore walls. CBMC work performed by Smit *et al.* confirmed the results of June *et al.*, and identified that monomethyl branched alkanes with a carbon number of 5 and 6 will reside completely in the MFI channel intersections,

whereas the branched alkanes with carbon numbers ranging from 7-10 will adsorb with the bulky head group in the channel intersection and the slender tails in the straight channel. Based upon these results for alkane adsorption, we postulate that diols and triols may also arrange themselves with the branched groups in the pore intersections and the hydrocarbon tails in the channels. This hypothesis is supported by two major features of Figure 2.12 - the decrease in K_{ads} from a diol to a triol with a corresponding number of carbons and the comparable increase in K_{ads} with carbon number for diols and triols. The decrease in K_{ads} from diols to triols could be caused by a decrease in the interactions with the pore walls from the addition of a hydroxyl group, while the increase of K_{ads} with carbon number could be caused by an increase in van der Waals interactions between the hydrocarbon chain and the zeolite channel walls.

It is also noteworthy that the lower value of K_{ads} for glycerol when compared with 1,2- and 1,3-propanediol corresponds well with the silicalite-1 adsorption results of Long *et al.* The authors found that the glycerol saturation coverage was an order of magnitude lower than that of the diols.[43] The results presented herein show that glycerol adsorption is less favorable than diol adsorption at low coverages, and this is likely due to a change in the preferential adsorption configuration due to hindrance from the third –OH group.

Our results also demonstrate that the high 1,3-propanediol/glycerol selectivity observed by Li *et al.* in the permeate feed may be partially due to the greater affinity of MFI for diol adsorption.[45] Our observation that K_{ads} decreases with a decrease in Si/Al also corroborates the result that 1,3-propanediol/water selectivity was greatest with silicalite-1 and that the removal of Brønsted acid sites increases the affinity for diol adsorption.[45]

2.4 Conclusions

Liquid phase adsorption isotherms of diols and triols were analyzed with respect to the known primary influences on the adsorption of alkanes in zeolites at low coverages: adsorbate-zeolite interactions related to the confinement of the adsorbate in the zeolite pore and hydrogen bonding between the adsorbate and zeolite Brønsted acid sites.

The logarithm of Henry's constants increased monotonically with carbon number for diol and triol adsorbates irrespective of the chemical identity of the framework implying that dispersion forces are the primary factor for adsorption in zeolites. This conclusion was supported by the result that the Henry's constants for propylene glycol adsorption on different zeolite frameworks and mesoporous materials decrease with an increase in adsorbent pore size. Adsorption isotherms for diols on FER indicate that 1,2-diols with carbon numbers greater than 3 cannot diffuse into the zeolite pore network and are likely adsorbed on the external crystal surface with the long hydrocarbon tail confined in the zeolite pore.

Henry's constants for triol adsorption on silicalite-1 were systematically lower than diols of the same carbon number leading to the hypothesis that the addition of –OH groups hinders interactions with the zeolite pore wall whereas K_{ads} for 1,2- and 1,3-propanediol adsorption on silicalite-1 was approximately the same indicating that the location of the –OH does not significantly change the diol configuration in the zeolite pores. Computational studies could be used to test these hypotheses and elucidate the changes in adsorbate configuration with respect to carbon number, zeolite topology, and number of hydroxyl groups.

Acknowledgment: The authors acknowledge the financial support from a Discovery Grant from the Institute on the Environment. Partial support for this work was also provided by the National Science Foundation: CBET 0855863.

CHAPTER

THREE

CORRELATIONS FOR ADSORPTION OF OXYGENATES ONTO ZEOLITES FROM AQUEOUS SOLUTIONS*

3.1 Introduction

The ability of zeolites to discriminate between alkanes of differing carbon number and degree of branching has led to their prevalent use as cracking, isomerization, and alkylation catalysts, and, in turn, inspired fundamental research on the interactions between zeolites and alkanes. It has been shown using calorimetric, gravimetric, spectroscopic, and computational studies that the enthalpy of adsorption of linear and branched alkanes increases with carbon number on several zeolite frameworks including MFI,[14,18–20] MOR,[20,21,39] FAU,[14,15,19,21] FER,[15,67] TON,[15] MTW,[15] UTD-1,[15] MWW,[22] and BEA,[20] which is due to an increase in dispersion interactions between the adsorbate and zeolite pore walls with increasing carbon number. The conclusion that confinement of the adsorbate in the zeolite pores is a significant contributor to the energy of adsorption is also supported by the observation in a calorimetric study that the enthalpy of adsorption of linear and branched alkanes decreases with an increase in zeolite pore size when comparing the MFI, MOR, and FAU frameworks.[14]

The effect of chemical composition on alkane adsorption has also been explored. Eder *et al.* obtained the enthalpy and Henry's constants for adsorption of C_3-C_9 linear alkanes on pure silica and aluminum containing samples of the MFI and FAU frameworks using calorimetry.[14,19] The authors noted that the materials with aluminum incorporated in the framework, which gives rise to Brønsted acid sites, exhibited a 10 kJ mol^{-1} and 6 kJ mol^{-1} increase in the adsorption enthalpy on the MFI and FAU frameworks, respectively, for all alkanes studied when compared with the siliceous materials. The contribution of acid site interactions to the energy of adsorption was low; it ranged from ∼10-20% of the total

*Reported from Mallon, E. E., Babineau, I.J., Kranz, J. I., Guefrachi, Y., Bhan, A., and Tsapatsis, M. *Journal of Physical Chemistry B* **115**(39), 11431-11438 (2011)

enthalpy measured for C_3-C_9 linear alkanes on H-MFI. This increase in adsorption enthalpy was compensated by a commensurate increase in adsorption entropy, and, therefore, a comparable free energy of adsorption was obtained on materials with the same framework irrespective of the number of acid sites at ambient temperatures. Overall, these studies show that the chemical composition of the zeolite framework has an effect on the enthalpy and entropy of adsorption for saturated hydrocarbons, but the energy of adsorption is primarily affected by the dispersion interactions between the adsorbate and zeolite pore walls.

Several authors have probed the primary interactions for adsorption of alcohols, which contain the additional functionality of a polar –OH group when compared with alkanes, on zeolites. Multiple studies have noted using gravimetry combined with calorimetric[23] and spectroscopic[40,42] approaches that alcohols preferentially adsorb via hydrogen bonding of the –OH group with the zeolite Brønsted acid sites. Although this results in an enthalpy of adsorption 50-60 kJ mol^{-1} greater for coverages less than 400 μmol g^{-1} when comparing siliceous and aluminum-containing MFI zeolites, the free energy of adsorption is relatively similar due to compensation from the entropy of adsorption.[23] This result, in conjunction with the finding that the heat of adsorption of alcohols increases 15-20 kJ mol^{-1} with each additional carbon,[23] highlights that dispersion forces, which arise from interaction between the adsorbate and the zeolite pore walls, are also a crucial factor in the adsorption affinity of alcohols.

Recently, we identified that many of the trends observed for the vapor phase adsorption of alkanes and alcohols on zeolites are also found for the adsorption of polyols, hydrocarbons functionalized with multiple –OH groups, onto zeolites from aqueous solutions. Specifically, we found that K_{ads} for these systems increases exponentially with carbon number on the MFI, BEA, and MWW frameworks[68] which is in accordance with observations made for the adsorption of alkanes, olefins, and epoxides onto TS-1 from a variety of solvents.[69,70] When this result was considered along with the observation that K_{ads} for propylene glycol adsorption on the FAU, MOR, BEA, MFI, and MWW materials increases with a decrease in zeolite pore size, it was concluded that dispersion forces between the adsorbate and the zeolite pore wall are a primary driving force for polyol adsorption.

For MFI materials it was found that changing the Si/Al from 10 to infinity resulted in a maximum increase in K_{ads} of only 50%; a similar indifference to MFI chemical composition was noted by Ramachandran *et al.* for the adsorption of hexene onto MFI from methanol.[71] When compared with the order of magnitude increase in K_{ads} with a decrease in zeolite pore size (compare FAU with MWW), it was concluded that dispersion interactions between the adsorbate and the zeolite pore wall are dominant compared to electrostatic interactions for polyol adsorption. Another outcome of our study was identification that the affinity for polyol adsorption from aqueous solutions decreases an order of magnitude with the

addition of an –OH group.[68] However, the origin of such a marked effect of C/OH ratio as well the effects of changing oxygen functionality and solution phase thermodynamics on zeolite adsorption affinity remained unclear at the end of Chapter 2.

Here, we show on the basis of a linear correlation between K_{ads} and the octanol-water partition coefficient, K_{ow}, that the effects of C/OH ratio and chemical functionality on oxygenate adsorption are the result of both interactions in the solution phase as well as strong dispersion interactions in the zeolite. This novel correlation enables the facile and accurate prediction of K_{ads} for polyfunctional C_2-C_6 molecules on zeolites varying in pore size and connectivity; also presented are data for some adsorbate-zeolite systems that do not obey this correlation, demonstrating that size exclusion can play a critical role in oxygenate adsorption, which allows for enhanced separation of molecules with similar K_{ow} values. We also show that solution non-idealities do not significantly perturb the correlation for C_2-C_4 diols on H-ZSM-5, indicating that the relationship between K_{ads} and K_{ow} is a strong function of dispersion forces in the lipophilic octanol/zeolite phase.

3.2 Methods

3.2.1 Adsorption Experiments

All experiments were completed using the protonated form of the FER, MFI, BEA, MWW, and FAU frameworks which had Si/Al ratios ranging over 29 to ∞ (6.2 to 0 Al/unit cell) as shown in Table 3.1. Sources for procured materials, methods for synthesized materials, and the pre-treatment conditions are reported in Chapter 2. X-ray diffraction was used to verify the structure of all zeolites.

Table 3.1: Structure and chemical composition of adsorbents

zeolite name	**framework**	**Si/Al**	**Al/uc**
CP914	FER	29[a]	1.2
ITQ-1	MWW	∞	0
CBV28014 (H-ZSM-5)	MFI	140	0.7
CP811C-300	BEA	100	0.6
CBV760	FAU	30	6.2

[a] Si/Al determined using inductively coupled plasma-optical emission spectroscopy by Galbraith. All other Si/Al values from vendor or approximated from synthesis procedure

All adsorbates were C_2-C_6 hydrocarbons with 2-3 oxygen functional groups. The adsorbates hydroxyacetone (Sigma Aldrich, 90%), propylene glycol (Fischer Scientific, >99%), and glycerol (Sigma-Aldrich, >99.5%) were in the liquid phase at ambient temperature and

atmospheric pressure. Dihydroxyacetone (Acros Organics USA, >98.5%, dimer) and glyceraldehyde (Sigma Aldrich, >90%, dimer) were in the solid phase at ambient temperature and atmospheric pressure. Sources and purities of the other oxygenate adsorbates can be found in reference.[68] Dihydroxyacetone stock solutions were prepared 24 hours in advance of the start of the experiment to allow dimers to dissociate into monomers at ambient temperature, as confirmed by C^{13} NMR analysis.[72,73]

Aqueous solutions with a volume of 1 mL were prepared in closed glass vials. Zeolite samples were added to each solution in the amount of 100±5 mg after the solutions had been chilled for 1 hour at 278±0.5 K. The slurries were stirred at 600 rpm for approximately 24 hours while maintaining a temperature of 278±0.5 K. The slurries were then filtered using a 3 mL Monoject syringe fitted with a 0.2 μm GHP (polypropylene) syringe filter to remove the zeolite particles and the filtrates were prepared for analysis with liquid chromatography.

The filtrate concentrations were analyzed using an Agilent 1200 High Performance Liquid Chromatography (HPLC) system equipped with a refractive index detector (RID) and an autosampler. The autosampler removed 75μL of sample from a single vial and injected the contents into a stream of 0.005 M sulfuric acid (H_2SO_4) in deionized water with a flow rate of 0.008 $cm^3\ s^{-1}$. The stream passed through a Bio-Rad Aminex HPX-87H polystyrene packed column heated to 333 K, and the column pressure was maintained at 40-60 bar. The outlet stream passed through the RID which was heated to 323 K. The RID signal output was recorded and plotted against time, and the adsorbate peak was identified from the retention time. No reaction products that would indicate chemisorption of the adsorbates on the zeolites were identified. The relative signal intensities of the adsorbate and a glycerol (or propylene glycol) internal standard were used to determine the final concentration of each solution. The difference in the initial and final concentrations and the total volume of the solution were used to calculate the amount of compound adsorbed onto the zeolite. Note that it was assumed that the solution volume is constant in this calculation as described in Section 5.5.3.

3.2.2 Computation of Octanol-Water Partition Coefficients (K_{ow})

Multiple methods were tested for their accuracy in computing the experimental K_{ow} values (obtained from the SRC PhysProp[74] or Sangster Research Laboratories LOGKOW[75] databases) for 22 C_1-C_6 polyols, aldehydes, ketones, and ethers which have functionality representative of the adsorbates used in this study as shown in Table 3.4. All computational methods explored and the root mean square errors (RMSE) between the computed and experimental PhysProp values for the test set of molecules are shown in Table 3.2. The ClogP method achieved the lowest RMSE regardless of the experimental database used and was, therefore, chosen for calculation of the K_{ow} values for the C_3 adsorbates used in this

study. This approach is supported by the observation that the ClogP algorithm produces the lowest RMSE for molecules with less than 20 atoms when compared with other widely available methods.[76,77]

Table 3.2: Sources of log P computational methods and comparison of results for the test set of experimental values from the SRS PhysProp database

model	**software**	**access**	**rmse**
ClogP[78]	ClogP 4.0	ChemBioDraw Ultra 11.0	0.114
AlogP[79]	DragonX	www.vcclab.org	0.236
LogKow[80]	KowWin 1.67	www.chemspider.com	0.175
ACD/LogP	ACD/LogP	www.chemspider.com	0.189
XlogP3[76]	XlogP3 3.3.2	www.vcclab.org	0.118
MlogP[81]	DragonX	www.vcclab.org	0.297
ALOGPS[82,83]	ALOGPS 2.1	www.vcclab.org	0.203

3.3 Results and Discussion

3.3.1 Effect of Adsorbate Functionality

Adsorption isotherms for the C_3 polyfunctional adsorbates on the H-ZSM-5 (MFI), BEA, FAU, and ITQ-1 (MWW) materials are shown in Figures 3.1, 3.2, 3.3, and 3.4, respectively. On these four frameworks, the affinity for adsorption at low concentrations increases in the order glyceraldehyde< glycerol< dihydroxyacetone< propylene glycol< hydroxyacetone which indicates that the affinity for adsorption is dependent on the oxygen functional groups since all adsorbates of interest contain three carbons each. The order of magnitude decrease in adsorption with increasing –OH number (compare glycerol with propylene glycol and dihydroxyacetone with hydroxyacetone) has been observed previously on the MFI framework,[68] and from these data it is noted that the trend is consistent on BEA, FAU, and ITQ-1. Exchanging an –OH group with a =O also has a significant effect on adsorption affinity. The exchange of –OH for =O on a primary carbon (compare glycerol and glyceraldehyde) decreases adsorption 10-90% whereas the exchange at a secondary carbon *increases* adsorption 200-400% as evidenced by comparing glycerol/dihydroxyacetone and propylene glycol/hydroxyacetone on H-ZSM-5, BEA, FAU, and ITQ-1.

It was of interest to compare the adsorption isotherm results with the octanol-water partition coefficient, K_{ow}, for the adsorbates since this is a well-established method for assessing the hydro- or lipophilicty of organic molecules. The K_{ow} values calculated with the ClogP group contribution method for the C_3 oxygenate adsorbates in this study are

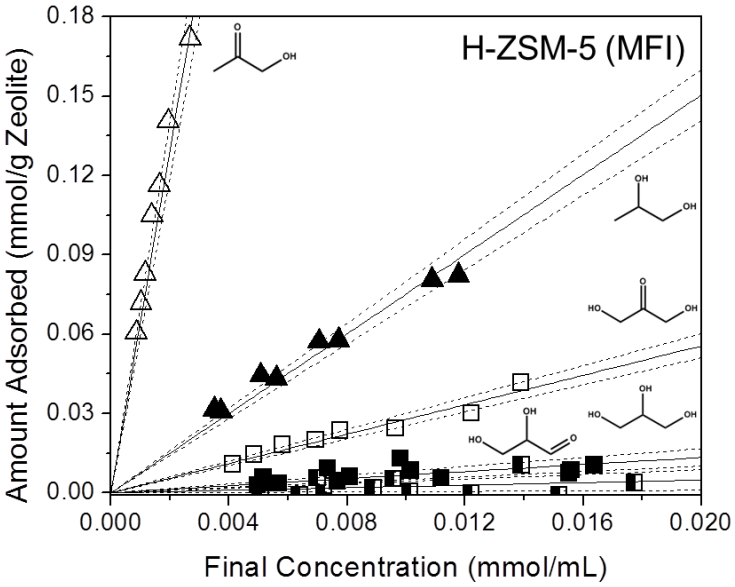

Figure 3.1: Adsorption isotherms at 278 K for hydroxyacetone (△), propylene glycol (▲), dihydroxyacetone (□), glycerol (■), and glyceraldehyde (◧) on H-ZSM-5. Solid lines represent least-squares linear regressions. Dashed lines represent 95% confidence intervals.

shown in Table 3.3. Inspection of these values reveals that they increase in the order: glyceraldehyde <glycerol <dihydroxyacetone <propylene glycol <hydroxyacetone, which is the same as the rank for adsorption strength observed on the H-ZSM-5, BEA, FAU, and ITQ-1 indicates that K_{ow} can be used to predict relative adsorption, and affinities of oxygenates onto zeolites.

3.3.2 Correlating K_{ads} for Polyfunctional Adsorbates

In order to better compare K_{ow} with the adsorption results, K_{ads} values were extracted from the adsorption isotherms. Using gravimetric methods, it has been shown that water adsorption on zeolites only occurs at the Brønsted acid sites that arise from incorporation of aluminum into the zeolite framework[41,55,56] and silanol groups at the external crystal surface and defects.[23,57] It has also been observed with gravimetric, calorimetric, and FTIR spectroscopy methods that water adsorbs with a heat of adsorption ∼30 kJ mol^{-1} less than methanol,[23] and, during competitive adsorption, methanol will displace water physisorbed on Brønsted acid sites.[40] Although water may not be competing for adsorption sites, it is important to note that water is possibly hydrogen bound to the adsorbed oxygenates as demonstrated by Krishna and van Baten using CBMC simulations.[84] This interaction

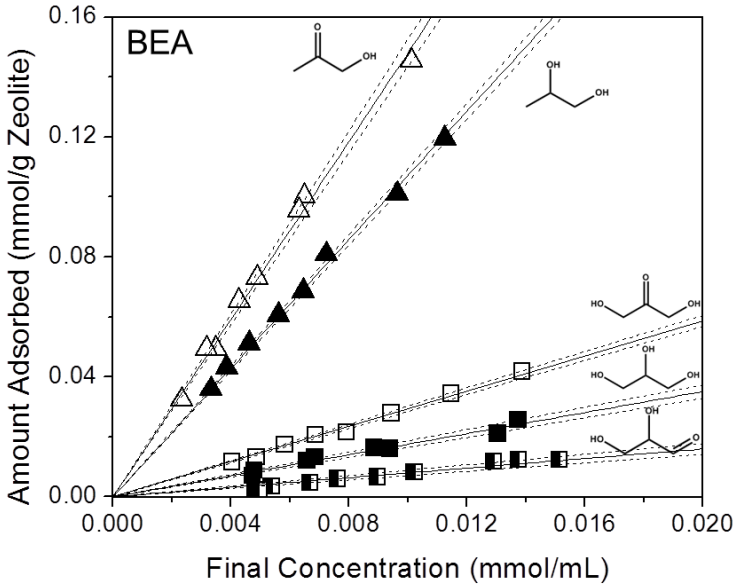

Figure 3.2: Adsorption isotherms at 278 K for hydroxyacetone (△), propylene glycol (▲), dihydroxyacetone (□), glycerol (■), and glyceraldehyde (■) on BEA. Solid lines represent least-squares linear regressions. Dashed lines represent 95% confidence intervals.

Table 3.3: K_{ow} values for the adsorbates.

adsorbate	**molecular formula**	$\boldsymbol{K_{ow}}$ [a]
Hydroxyacetone[b]	CH_3COCH_2OH	0.294
Propylene glycol[b,c]	$CH_3CH(OH)CH_2OH$	0.087
Dihydroxyacetone[b]	$HOCH_2COCH_2OH$	0.055
Glycerol[b,c]	$HOCH_2CH(OH)CH_2OH$	0.029
Glyceraldehyde[b]	$HOCH_2CH(OH)CHO$	0.018
1,2-Hexanediol[c]	$CH_3(CH_2)_3CH(OH)CH_2OH$	3.364
1,2-Butanediol[c]	$CH_3CH_2CH(OH)CH_2OH$	0.294
1,3-Propanediol[c]	$HO(CH_2)_3OH$	0.092
Ethylene glycol[c]	$HO(CH_2)_2OH$	0.043
1,2,6-Hexanetriol[c]	$HO(CH_2)_4CH(OH)CH_2OH$	0.035
1,2,4-Butanetriol[c]	$HO(CH_2)_2CH(OH)CH_2OH$	0.014

[a]Calculated using the ClogP[78] group contribution method. [b]Adsorbate in this study. [c]Adsorbate in this study and Mallon *et al.*[68]

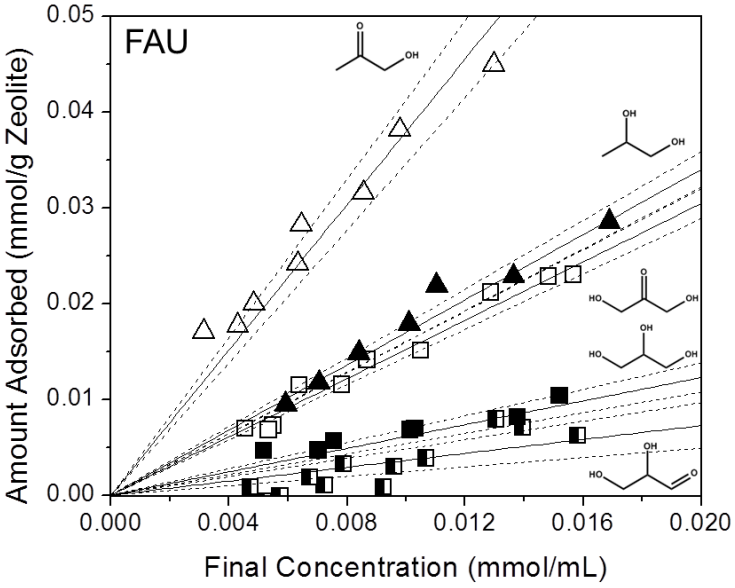

Figure 3.3: Adsorption isotherms at 278 K for hydroxyacetone (△), propylene glycol (▲), dihydroxyacetone (□), glycerol (■), and glyceraldehyde (◧) on FAU. Solid lines represent least-squares linear regressions. Dashed lines represent 95% confidence intervals.

would have an effect on the energetics of adsorption and, therefore, on K_{ads}. However, we cannot discern the magnitude of these effects and have, therefore, adopted an initial approach where we have neglected adsorbate-water interactions within the zeolite pores and are treating the adsorption isotherms here as single-component adsorption isotherms.

The data here are for coverages between ∼0.001 to 1 oxygenates per unit cell which represents less than 10% of the total micropore volume and is well below the maximum site occupancy and the regime where site heterogeneity or oxygenate-oxygenate interactions are expected to have an effect on adsorption based upon computational studies on the siting of straight and branched alkanes in MFI.[85,86] At these low coverages, it is expected that the molecules preferentially adsorb in one type of adsorption site and adsorption is linearly correlated with concentration. Therefore, the data were fit using least-squares linear regression and the K_{ads} values were determined from the slope of the line.

Plotting K_{ads} versus K_{ow} for adsorption on H-ZSM-5 at 278 K reveals a linear correlation between affinity for adsorption and hydro-/lipophilicty, as shown in Figure 3.5. K_{ads} values for C_2-C_6 diols on H-ZSM-5 at 278 K (isotherms presented in Figure 3.9) also fall on this linear correlation between K_{ads} and K_{ow}. It is clear that K_{ow}, which can be readily calculated using available software, is an accurate predictor of the adsorption affinity of

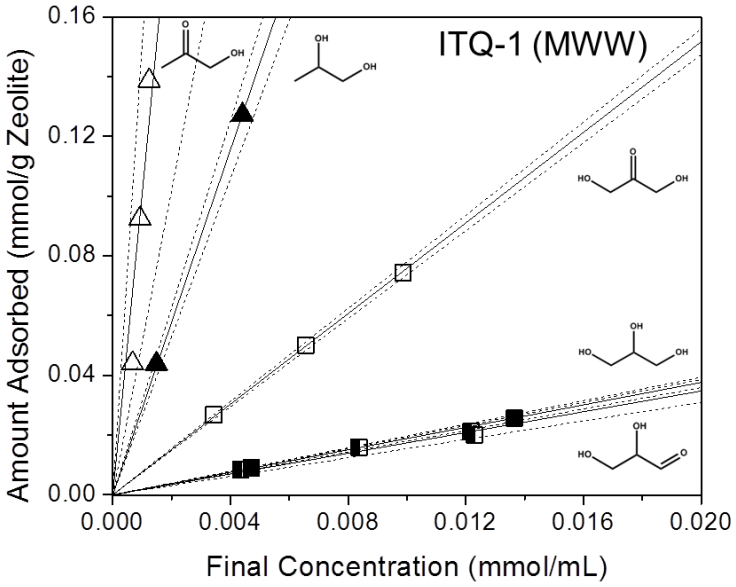

Figure 3.4: Adsorption isotherms at 278 K for hydroxyacetone (△), propylene glycol (▲), dihydroxyacetone (□), glycerol (■), and glyceraldehyde (◧) on ITQ-1. Solid lines represent least-squares linear regressions. Dashed lines represent 95% confidence intervals.

polyfunctional oxygenates onto H-ZSM-5 from aqueous solutions with K_{ads} values spanning at least 5 orders of magnitude. This is the first demonstration of the predictive nature of K_{ow} for K_{ads} on zeolites from aqueous solutions.

3.3.3 Effect of Solution Thermodynamics

Although the linear correlation between K_{ads} and K_{ow} is practically useful, the interactions responsible for the trend are unknown. That is, hydrophobic interactions in water or dispersion forces in the lipophilic octanol/zeolite phase could both be used to explain the observed linear correlation between K_{ads} and K_{ow} for the diols, hydroxy-ketones, and glyceraldehyde. Thermodynamic definitions of chemical potential and equilibrium can be used to decouple the interactions, that is,

$$\mu_{ads} = \mu_{bulk}, \tag{3.1}$$

where μ_{ads} and μ_{bulk} are the chemical potentials of the adsorbate in the adsorbed and bulk phases, respectively. For a system of M identical adsorption sites, N adsorbate molecules with N<M, and negligible adsorbate-adsorbate interactions, one can use statistical mechanics to derive the expression,

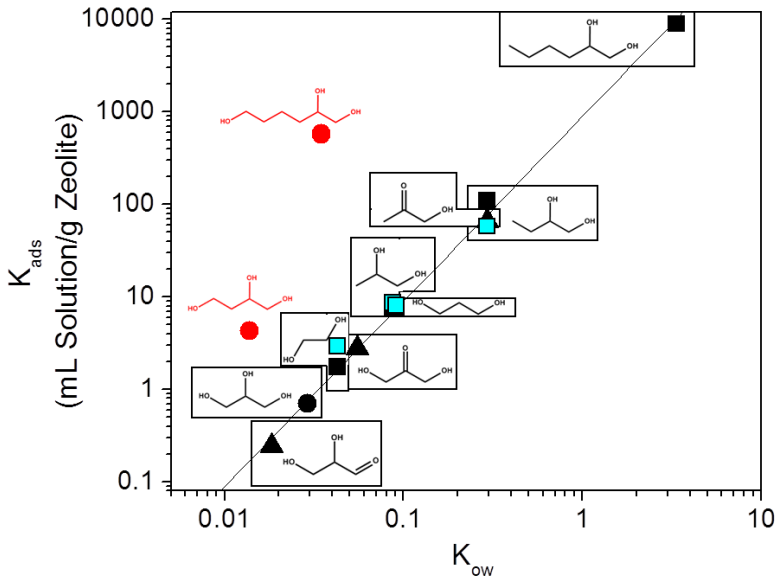

Figure 3.5: Measured K_{ads} versus K_{ow} on MFI CBV28014 at 278 K for carbonyl-containing molecules (▲), diols (■), and 1,2,ω-triols (● and ●). The solid line represents the least-squares linear regression on the black data points. Diol $K_{\text{ads,intrinsic}}$ values (■) obtained by decoupling the solution activity coefficients from the measured water-zeolite partition coefficients.

$$\mu_{ads} = kT \ln \left[\frac{\theta}{(1-\theta)f} \right], \tag{3.2}$$

where $\theta = N/M$, k is the Boltzmann constant, and f is the partition function associated with a single adsorbed molecule.[9] Furthermore, if one considers equilibrium between the adsorbed phase and an ideal gas phase one obtains

$$\theta = \frac{bp}{1+bp}, \tag{3.3}$$

where $b(T) = f(T)e^{\mu^0/kT}$ is an equilibrium constant and p is the pressure. This is the form of the Langmuir isotherm model. We use the same approach, but for equilibrium between the adsorbed phase and a solution phase, that is,

$$kT \ln \left[\frac{\theta}{(1-\theta)f} \right] = \mu^0(T) + kT \ln a_i^l, \tag{3.4}$$

where a_i^l is the activity of component i in solution and is defined as the product between the pure species fugacity (f_i^l), mole fraction (x_i), and activity coefficient (γ_i) normalized to a reference fugacity (f_i^0). This expression simplifies to

$$kT \ln \left[\frac{\theta}{(1-\theta)f} \right] = \mu^*(T) + kT \ln x_i \gamma_i, \tag{3.5}$$

where $\mu^*(T)$ is the chemical potential of the pure liquid species. Following the same procedure as for the Langmuir isotherm one obtains

$$\theta = \frac{b\gamma_i x_i}{1+b\gamma_i x_i}, \tag{3.6}$$

where $b(T) = f(T)e^{\mu^*/kT}$ is now defined as the equilibrium constant.

At low concentrations, where $1 >> b\gamma_i x$, we find that $\theta = b\gamma_i x_i$ or that the coverage, θ, is directly proportional to the solution mole fraction, x_i, with a slope equal to $b\gamma_i$. This equation has the same form as Henry's law, which we have applied to the isotherms presented here. Therefore, the proportionality constant in our experiments, K_{ads}, for the linear relationship between the amount adsorbed and the final solution concentration, is not the intrinsic K_{ads} value for adsorption from an ideal gas phase. Rather, this value is a combination of interactions in the solution phase and the adsorbed phase, that is $K_{\text{ads,measured}} = \gamma_i K_{\text{ads,intrinsic}}$.

Now that it has been shown that the K_{ads} value measured is the result of the product between the solution activity coefficient and the true K_{ads} value, it follows that if the activity coefficient is known then the true K_{ads} can be determined. Since the concentrations used for

this and the study presented in Chapter 2 range from 1-25 μmol cm^{-3}, which is below the concentration used by Suleiman and Eckert[87] to obtain infinite dilution activity coefficients using a dew point technique, we considered infinite dilution activity coefficients, which are essentially a measure of interactions between a single solute molecule surrounded by solvent, as appropriate for decoupling $K_{\text{ads,measured}}$ and $K_{\text{ads,intrinsic}}$. The $K_{\text{ads,intrinsic}}$ values obtained are also plotted in Figure 3.5, and it can be deduced from this analysis that increasing diol carbon number decreases water solubility, which has an effect on $K_{\text{ads,measured}}$, but the systematic increase in K_{ads} with diol carbon number can be attributed to increased dispersion interactions. This result for diol adsorption is consistent with the well-documented literature on single component alkane adsorption on the MFI framework, where it has been shown that K_{ads} increases exponentially with carbon number.[19,20] Furthermore, it has been shown using density functional calculations that the increasing stability of both physi- and chemisorbed C_1-C_4 alcohols on H-ZSM-5 with increasing carbon number is due to dispersive van der Waals interactions consistent with our hypothesis that the increase in K_{ads} with increasing 1,2-diol carbon number is due to confinement in the zeolite pore.[26]

When the infinite dilution coefficients at 298 K for 1-propanol[88] (13.8) and 1,2-propanediol (1.0) are compared, it can be deduced that the addition of an –OH group decreases the activity coefficient by an order of magnitude. This trend also holds when 1-butanol[88] (55.2) is compared with 1,2-butanediol (2.0).[68] Therefore, interactions between water and the adsorbate in the bulk, as measured by the activity coefficient, may be responsible for the inversely proportional relationship between K_{ads} and –OH number.

3.3.4 Effect of Zeolite Structure

The zeolite topology can also play a significant role in the adsorption of oxygenates. For example, it can be noted from Figure 3.5 that the K_{ads} values for 1,2,4-butanetriol and 1,2,6-hexanetriol are higher than what is expected from their K_{ow} values. This implies that K_{ads} is not a function of hydro-/lipophilicity alone, and K_{ow} does not adequately capture a critical component of 1,2,4-butanetriol and 1,2,6-hexanetriol adsorption on H-ZSM-5. Although errors in K_{ow} estimation may be partially responsible for this deviation (the XlogP3 method[19] yields K_{ow} values for these two compounds that are larger by factors of 3 and 6, respectively; see Table 3.5), it could also arise due to differences in the adsorption environments of H-ZSM-5 and octanol. While adsorption in both phases is primarily driven by dispersion forces,[68,89] the strength of these non-polar interactions are significantly different as shown in Figure 3.5. The addition of a single methyl group leads to an increase in K_{ads} by an order of magnitude, whereas K_{ow} only increases approximately 5-fold. This disparity in adsorption environment may be even more pronounced for 1,2,4-butanetriol and 1,2,6-hexanetriol than glycerol, the only triol that falls on the correlation, due to pref-

erential siting in H-ZSM-5. It has been shown via Monte Carlo simulations that iso-alkanes with a carbon number less than 6 will completely reside within the channel intersection, whereas the longer (C_7-C_{10}) alkanes adsorb with the bulky branched segment in the channel intersection, and the slender hydrocarbon tail in the straight channel.[66,86] Therefore, we postulate that the long hydrocarbon chains of 1,2,4-butanetriol and 1,2,6-hexanetriol can reach into the straight channel, where they have closer interaction with the pore walls, resulting in the observed higher K_{ads} value than what is predicted by the correlation with K_{ow}. Exploration of the water-adsorbate and zeolite-adsorbate interactions using computational methods would best elucidate the cause of K_{ads} dependence on –OH number.

As shown in Figure 3.6, the linear increase in K_{ads} with increasing K_{ow} for the C_3 polyfunctional adsorbates in this study is observed not only on H-ZSM-5 but also on FAU, BEA, and ITQ-1 (MWW framework). It should also be noted that K_{ads} for each adsorbate increases as the smallest accessible pore size decreases from 6 Å (FAU) to 4 Å (ITQ-1). This effect is also evidenced by the increase in the correlation slope with decreasing pore size as shown in the top inset of Figure 3.6, a trend which can be utilized to adjust the correlation to predict adsorption on zeolites with a variety of pore sizes. The observed increase in adsorption affinity with decreasing zeolite pore size is not surprising. This result is in agreement with what has been found for C_1-C_6 alkane[15,67] and propylene glycol[68] adsorption, which supports the conclusion that adsorption of polyfunctional molecules from aqueous solutions is a strong function of dispersion forces between the adsorbate and the zeolite pore walls.

After noting the versatility of K_{ow} as a predictor for K_{ads} of polyfunctional molecules in water over medium and large pore zeolites, it was of interest to employ a smaller, 8-member ring (MR) zeolite adsorbent to determine if shape selectivity effects could be used to disrupt this correlation and lead to large K_{ads} differences which may be desirable for highly selective separation processes. An analogous situation with hydrocarbons is the use of ITQ-12 (ITW framework) to achieve a high propylene/propane separation selectivity partially due to an order of magnitude difference in the Henry's constants as shown by gravimetry and Monte Carlo calculations at 353 K.[90,91] A strong effect of molecular size was also noted via thermogravimetry,[64,67,92] ^{13}C NMR,[92] and FTIR[64,67,93] for alkane adsorption on FER, a zeolite containing narrow 8-MR (3.5 Å) and 10-MR (4.2 Å) channels. Linear alkanes with a carbon number of 5 or greater adsorb preferentially in the 10 MR channel,[67,92] while branched alkanes adsorb on the exterior of the crystal with the longest alkyl chain either parallel to the surface or protruding into the pore mouth.[64,93]

As anticipated, the trend observed on the other frameworks does not hold for FER as shown in Figure 3.7. FER is the only zeolite in this study on which adsorption of dihydroxyacetone surpasses that of propylene glycol, and, therefore, adsorption does not

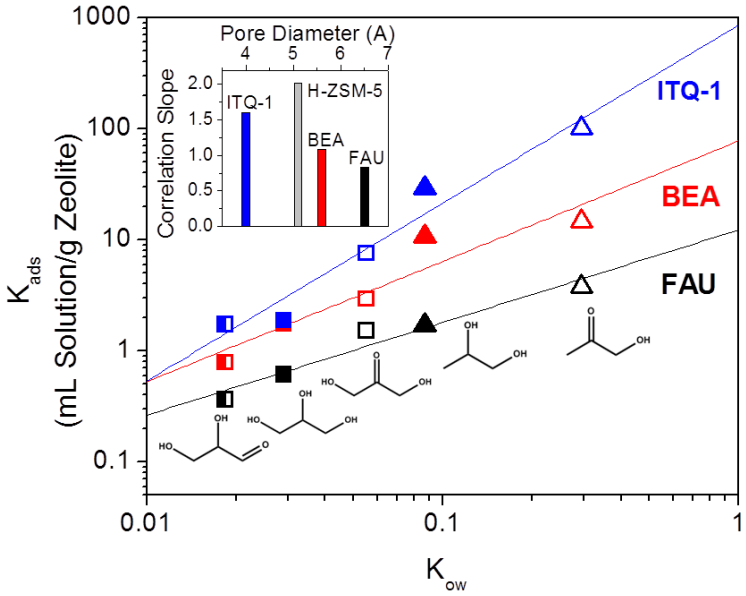

Figure 3.6: Measured K_{ads} versus K_{ow} for the carbonyl-containing adsorbates and their polyol counterparts on FAU, BEA, and ITQ-1 at 278 K. Solid lines represent least-squares linear regressions. (Inset at top) K_{ads}-K_{ow} correlation slopes versus pore size for FAU, BEA, H-ZSM-5, and ITQ-1.

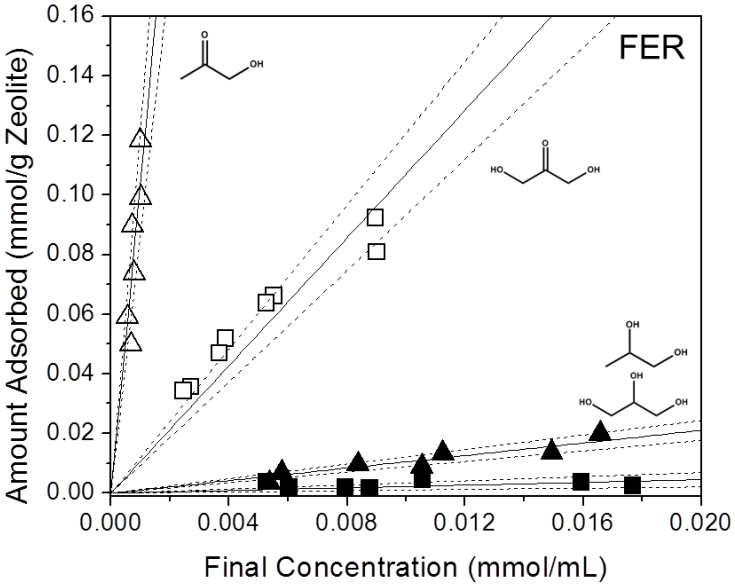

Figure 3.7: Adsorption isotherms at 278 K for hydroxyacetone (△), propylene glycol (▲), dihydroxyacetone (□), and glycerol (■), on FER. Glyceraldehyde adsorption was negligible. Solid lines represent least-squares linear regressions. Dashed lines represent 95% confidence intervals.

consistently increase with an increase in K_{ow}. Similarly, adsorption of C_2-C_6 polyols on FER does not increase with K_{ow} as shown in Figures 3.10 and 3.11, and the systematic increase in adsorption affinity with carbon number noted on MFI, BEA, and ITQ-1 framework materials is also not observed on FER as shown in our previous work.[68]

Furthermore, a single linear correlation between K_{ads} and K_{ow} is not obtained on FER as shown in Figure 3.8. C_3 ketones and 1,ω-diols have an adsorption affinity 1-2 orders of magnitude greater than their branched polyol counterparts (compare dihydroxyacetone/glycerol, hydroxyacetone/propylene glycol, and 1,3-propanediol/propylene glycol); glyceraldehyde adsorption was negligible on this zeolite framework. We postulate that the decrease in K_{ads} with an increase in branching, which is equivalent to an energy difference of 7-11 kJ mol^{-1}, is driven by differences in adsorption configurations. As shown in Figure 3.8, the ketone correlation on FER is approximately collinear with the correlation found for the 10-MR framework, ITQ-1, indicating that these molecules preferentially adsorb in the 10-MR channel of FER. Since hydroxyacetone and dihydroxyacetone are the only adsorbates in this study that have sp^2 hybridized secondary carbons, it is plausible that their planar molecular configurations allow them to adsorb in the 10-MR channel of FER. It is proposed that branched polyols, like iso-alkanes, cannot fully access the 10-MR channel of

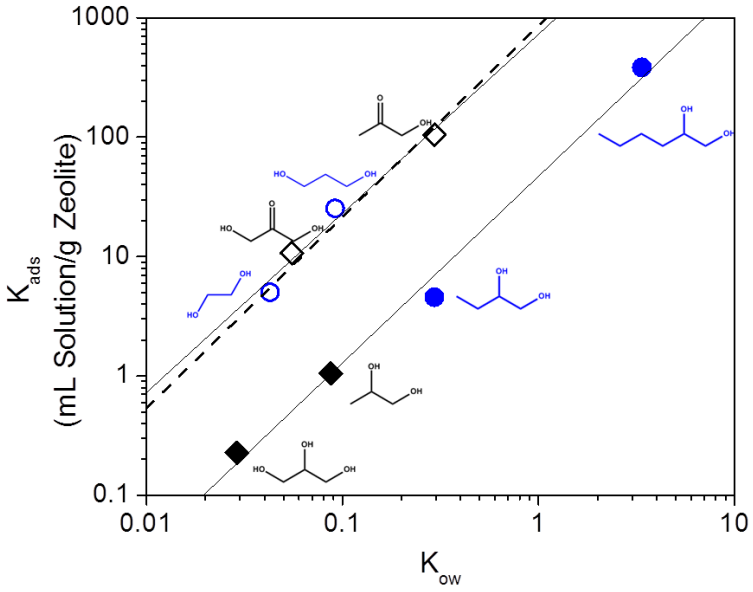

Figure 3.8: Measured K_{ads} versus K_{ow} for the carbonyl-containing adsorbates (♢), their polyol counterparts (♦), and other 1,2- (•) and 1,$\omega-$diols (○) on FER at 278 K. Solid lines represent least-squares linear regressions. Dashed line represents the correlation found on ITQ-1.

FER and only adsorb on the external crystal surface resulting in an order of magnitude lower number of adsorption sites[64] as well as a lower heat of adsorption,[64,67] both of which are reflected in the observed decrease in K_{ads}.

3.4 Conclusions

A linear correlation between K_{ads} of C_2-C_6 oxygenates on H-ZSM-5 and the readily calculated octanol-water partition coefficient, K_{ow}, was presented which allows for simple prediction of K_{ads} for these molecules. Decoupling the intrinsic K_{ads} values from the adsorbate infinite dilution activity coefficient in water revealed that although water-adsorbate interactions in the bulk phase have an effect on zeolite adsorption, an exponential dependence of K_{ads} on adsorbate carbon number is still observed which indicates that confinement of the adsorbate in the zeolite pore is a critical factor in adsorption. This conclusion is also supported by the observation that there is an increase in K_{ads} with decreasing zeolite pore size for all C_3 adsorbates in this study.

Correlations between K_{ads} and K_{ow} were also identified for the FAU, BEA, and ITQ-1 (MWW) zeolites, indicating the applicability and tunability of the K_{ads}-K_{ow} correlation for

a variety of zeolite frameworks. The only exceptions to the correlation were found for bulky 1,2,ω-triols on H-ZSM-5 and all adsorbates on the FER framework, which emphasizes not only the effect of adsorbate functionality on adsorption, but also the role of zeolite topology on adsorption. Overall, these data may be applied to elucidate the interactions responsible for separations of oxygen-containing molecules using zeolite adsorbents.

3.5 Supporting Information

Table 3.4: Molecules used to calculate RMSE values for the K_{ow} calculation methods.

class	**molecule**	**molecular formula**	$\boldsymbol{K_{ow}}$ [a]
polyols	ethylene glycol	$HO(CH_2)_2OH$	0.044
	propylene glycol	$CH_3CH(OH)CH_2OH$	0.120
	1,3-propanediol	$HO(CH_2)_3OH$	0.091
	glycerol	$HOCH_2CH(OH)CH_2OH$	0.017
linear alcohols	methanol	CH_3OH	0.170
	ethanol	CH_3CH_2OH	0.490
	propanol	$CH_3(CH_2)_2OH$	1.778
	butanol	$CH_3(CH_2)_3OH$	7.586
	pentanol	$CH_3(CH_2)_4OH$	32.36
	hexanol	$CH_3(CH_2)_5OH$	107.2
branched alcohols	2-propanol	$CH_3CH(OH)CH_3$	1.122
	isobutanol	$CH_3CH(CH)_3CH_2OH$	5.754
	tert-butyl alcohol	$(CH_3)_3C(OH)$	2.239
ketones	acetone	CH_3COCH_3	0.575
	2-butanone	$CH_3COCH_2CH_3$	1.950
	2-pentanone	$CH_3CO(CH2)_2CH3$	8.128
	2-hexanone	$CH_3CO(CH2)_3CH3$	23.99
aldehydes	acetaldehyde	CH_3CHO	0.457
	propionaldehyde	CH_3CH_2CHO	3.890
	butyraldehyde	$CH_3(CH_2)_2CHO$	7.586
glycol ethers	methoxyethanol	$CH_3O(CH_2)_2OH$	0.170
	2-ethoxyethanol	$CH_3CH_2O(CH_2)_2OH$	0.479

[a] SRS PhysProp[74] database experimental K_{ow} values

3.5.1 Extracting K_{ads} for C_6 Polyfunctional Adsorbates

Due to the strong adsorption affinity of 1,2-hexanediol and 1,2,6-hexanetriol on H-ZSM-5 and 1,2-hexanediol adsorption on FER (see Figure 3.10) as well as the limits of detection for the HPLC, the isotherms for these systems include both Henry's Law and saturation

Table 3.5: K_{ow} values for the adsorbates from the XLogP3 and LogKow computational methods.

adsorbate	**molecular formula**	**XLogP3**[76] K_{ow}	**LogKow**[80] K_{ow}
Hydroxyacetone[a]	CH_3COCH_2OH	0.195	N/A
Propylene glycol[b]	$CH_3CH(OH)CH_2OH$	0.120	0.166
Dihydroxyacetone[a]	$HOCH_2COCH_2OH$	0.044	0.195
Glycerol[b]	$HOCH_2CH(OH)CH_2OH$	0.017	0.022
Glyceraldehyde[a]	$HOCH_2CH(OH)CHO$	0.026	0.085
1,2-Hexanediol[b]	$CH_3(CH_2)_3CH(OH)CH_2OH$	N/A	4.898
1,2-Butanediol[b]	$CH_3CH_2CH(OH)CH_2OH$	0.661	0.513
1,3-Propanediol[b]	$HO(CH_2)_3OH$	0.091	0.195
Ethylene glycol[b]	$HO(CH_2)_2OH$	0.044	0.063
1,2,6-Hexanetriol[b]	$HO(CH_2)_4CH(OH)CH_2OH$	0.204	0.170
1,2,4-Butanetriol[b]	$HO(CH_2)_2CH(OH)CH_2OH$	0.040	0.017

[a]Adsorbate in this study. [b]Adsorbate in this study and Mallon *et al.*[68]

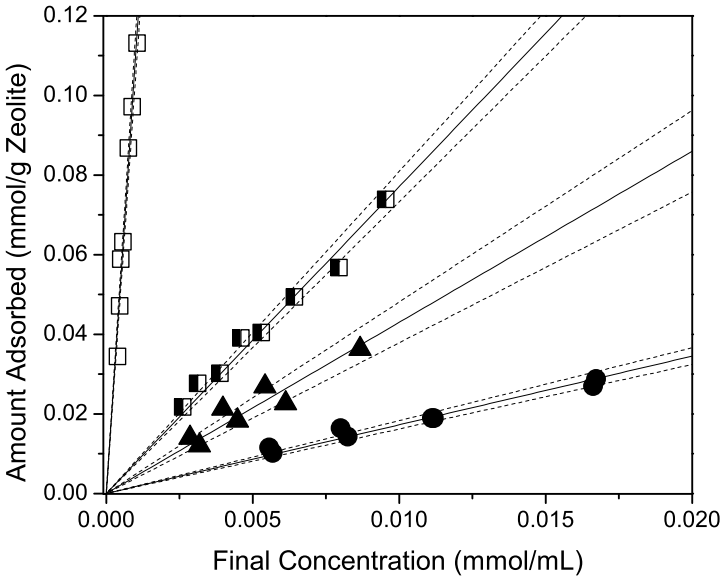

Figure 3.9: Adsorption isotherms at 278 K for ethylene glycol (•), 1,3-propanediol (▲), 1,2-butanediol (□), and 1,2,4-butanetriol (■) on H-ZSM-5. Solid lines represent least-squares linear regressions. Dashed lines represent 95% confidence intervals.

features. Therefore, the data were fit with the Langmuir linear equation,

$$\frac{[A]}{[A*]} = \frac{[A]}{[*]_0} + \frac{1}{K[*]_0}, \tag{3.7}$$

where $[A]$ is the final concentration of species A in solution, $[A*]$ is the amount of A adsorbed on the surface at that bulk concentration, $[*]_0$ is the maximum amount of A that can be adsorbed on the surface, and K is the equilibrium constant between the bulk and adsorbed species, A and A* respectively. The K_{ads} values reported here, which are the product of K and $[*]_0$, could then be calculated using the slope and intercept of the linearized adsorption isotherm.

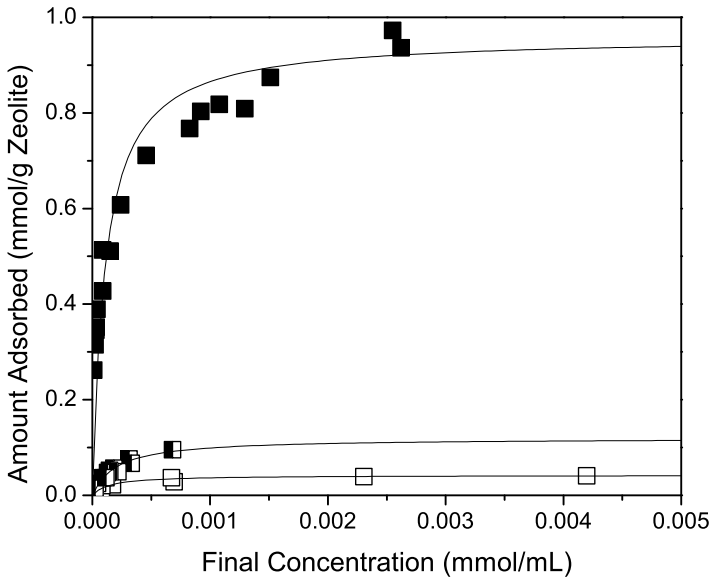

Figure 3.10: Adsorption isotherms at 278 K for 1,2-hexanediol (■) and 1,2,6-hexanetriol (■ □) on H-ZSM-5 and 1,2-hexanediol (□) on FER. Solid lines represent Langmuir isotherms calculated using parameters obtained from Langmuir linear regressions of the data.

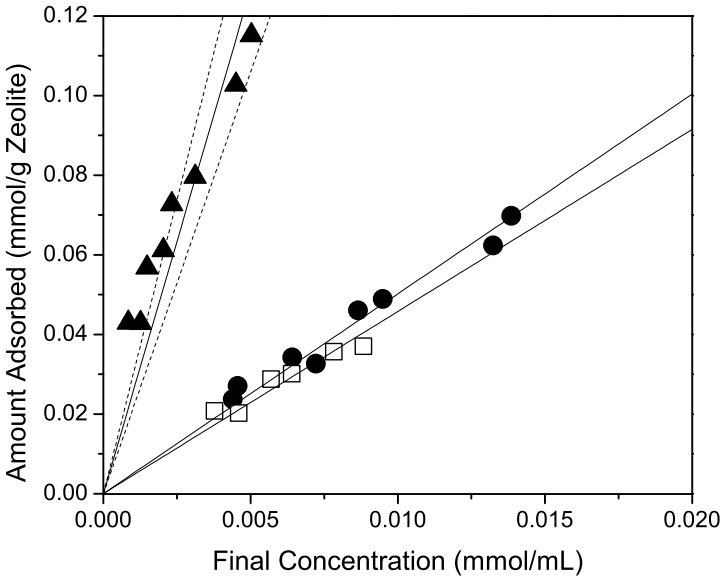

Figure 3.11: Adsorption isotherms at 278 K for ethylene glycol (•), 1,3-propanediol (▲), and 1,2-butanediol (□) on FER. Solid lines represent least-squares linear regressions. Dashed lines represent 95% confidence intervals.

Acknowledgment: This material is based upon work supported in part by the Catalysis Center for Energy Innovation, an Energy Frontier Research Center funded by the U.S. Department of Energy under Award No. DE-SC0001004. E.E.M. was supported by the National Science Foundation: CBET 0855863.

CHAPTER

FOUR

TEMPERATURE EFFECTS ON ADSORPTION OF OXYGENATES ONTO ZEOLITES FROM AQUEOUS SOLUTIONS

4.1 Introduction

The relationship between aqueous oxygenate adsorption affinity and oxygenate functionality was investigated in Chapters 2 and 3, and it was found that K_{ads} increases exponentially with polyol carbon number demonstrating that adsorption of these molecules is highly dependent on dispersion interactions with the zeolite pore walls. This conclusion was further supported by solution thermodynamic analyses that indicate that this trend holds regardless of interactions between the adsorbate and water in the bulk. This same analysis led to the hypothesis that variations in K_{ads} with the number and location of adsorbate polar functional groups are likely due to hydrogen bonding with water.

Through the acquisition and analysis of K_{ads} values at multiple temperatures, one can decouple K_{ads} into its enthalpic and entropic contributions thus enabling a deeper understanding of the driving forces for aqueous polyol adsorption onto zeolites. Specifically, the hypothesis that polyol adsorption is the result of strong dispersion interactions would be tested by quantifying the adsorption enthalpies. Entropic effects in the bulk and in the zeolite, both of which would impact polyol adsorption affinity, could also be probed to discern the influence of topology on entropic/enthalpic drivers of adsorption.

Determination of polyol transfer enthalpies and entropies from aqueous solutions onto zeolites would also enable calculation of vapor adsorption enthalpies and entropies useful for catalysis. Ma and Yang proposed a thermodynamic cycle to extract vapor adsorption enthalpies from adsorption isotherms of thiophenic compounds from n-octane and hexadecane on NaY, 13X, and Cu(I)-Y zeolites.[27,28] The authors calculated average thiophene adsorption enthalpies on NaY and Cu(I)-Y that were within 4% of the values obtained

experimentally from vapor adsorption isotherms thus demonstrating the viability of their approach.

Aqueous adsorption isotherms for C_3 diols, propylene glycol and 1,3-propanediol, on aluminium-containing H-MFI and H-BEA were measured at temperatures ranging from 298-303 K. It was found that adsorption for these systems is exothermic, with transfer enthalpies ranging from -4 to -10 kJ mol^{-1}. While transfer entropy losses were identified for adsorption of the diols on H-MFI, it was found that propylene glycol gains 5 J mol^{-1} K^{-1} upon transfer to H-BEA, which is likely due to strong hydrogen bonding with water in the bulk. Vapor adsorption enthalpies and entropies for these systems were calculated to find that the propylene glycol adsorption enthalpy changed by -5 kJ mol^{-1} from H-BEA to H-MFI, while the entropic change was -19 J mol^{-1} K^{-1}, which is in quantitative agreement with trends found for alkanes. The adsorption enthalpies for propylene glycol and 1,3-propanediol on H-MFI were calculated at -90 kJ mol^{-1}, and this result was accompanied by a -9 J mol^{-1} K^{-1} change with increasing branching, thus indicating that hydroxyl group location may not have a significant effect on vapor adsorption affinity. Future work encompassing vapor gravimetric and calorimetric experiments would test the validity of the vapor adsorption enthalpies and entropies reported here.

4.2 Methods

All experiments were completed using protonated zeolites procured from Zeolyst. CBV28014 is an MFI zeolite with a Si/Al ratio of 140 (0.7 Al/uc). CP811C-300 has the BEA framework with Si/Al$\sim$100 (0.6 Al/uc). Both materials were characterized via X-ray diffraction and nitrogen physisorption. Pre-treatment conditions for the zeolite adsorbents, and sources and purities of the propylene glycol and 1,3-propanediol adsorbates can be found in Chapter 2.

Preparation of the water/adsorbate/zeolite slurries is described in detail in Chapter 3. Adsorption isotherms here were measured at 278-303 K at 5 K intervals. The slurries were filtered and analyzed with high performance chromatography (per the procedure described in Chapter 3) in order to determine the final concentration. The amount adsorbed was calculated with the assumption that the solution volume does not change with adsorption (see Section 5.5.3).

4.3 Results and Discussion

4.3.1 Effect of Temperature on Adsorption

Adsorption isotherms at 278-303 K for propylene glycol and 1,3-propanediol on H-MFI and H-BEA are reported in Figures 4.1-4.3. Although the amount adsorbed only varies 1-10%

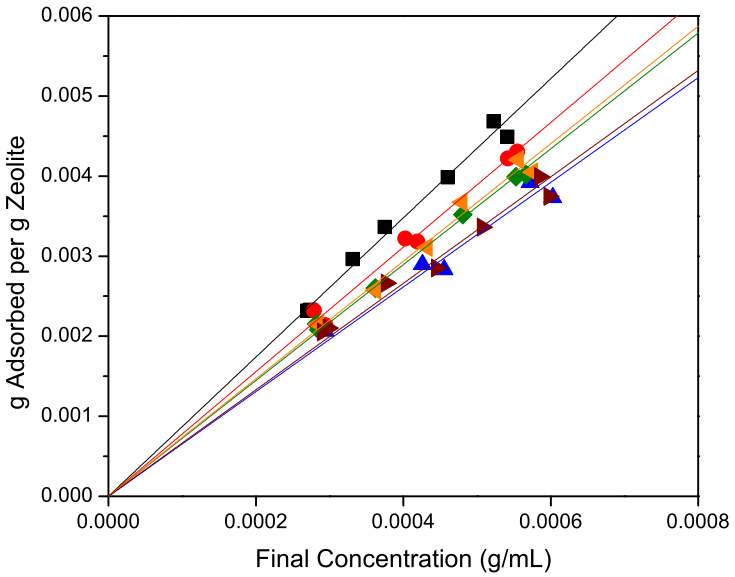

Figure 4.1: Adsorption isotherms for propylene glycol on H-MFI at 278 (■), 283 (●), 288 (◀), 293 (♦), 298 (▶), and 303 (▲) K. Solid lines represent least-squares linear regressions.

with each 5 K temperature increase, it is clear that the amount adsorbed decreases as temperature increases, and, therefore, adsorption is exothermic for these systems.

As discussed in Section 2.3.1, the Henry's constants, K_{ads}, can be determined by fitting each isotherm with a least-squares linear regression. Furthermore, since we now have K_{ads} at a range of temperatures, we can calculate the enthalpy change associated with transfer of these C_3 diols to zeolites from aqueous solutions. According to the van't Hoff equation,

$$\ln\left(\frac{K_{ads,2}}{K_{ads,1}}\right) = -\frac{\Delta H}{R}\left(\frac{1}{T_2} - \frac{1}{T_1}\right), \tag{4.1}$$

where $K_{\text{ads},2}$ and $K_{\text{ads},1}$ are the equilibrium or Henry's constants at temperatures T_2 and T_1, respectively, ΔH is the enthalpy change for the process, and R is the universal gas constant. The van't Hoff plots for each adsorbate/zeolite system can be found in Figures 4.4 and 4.5.

As can be observed from the data reported in Figure 4.4, although K_{ads} only changes 12-30% with a temperature increase from 278 to 303 K, the van't Hoff plots for propylene glycol on H-MFI and H-BEA are different with 95% confidence, indicating that the enthalpies for transfer from the bulk to the zeolite for each system are statistically different.

Since the Henry's constant, enthalpy, and temperature are known for each system, the

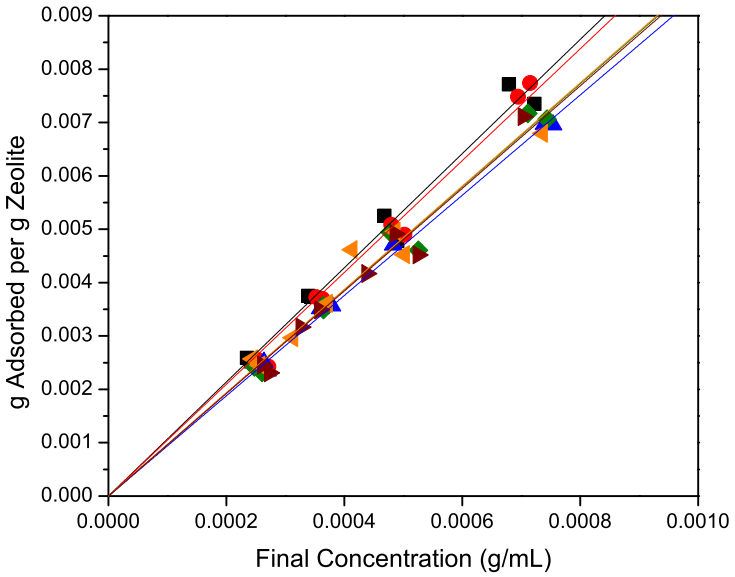

Figure 4.2: Adsorption isotherms for propylene glycol on H-BEA at 278 (■), 283 (●), 288 (◀), 293 (♦), 298 (▶), and 303 (▲) K. Solid lines represent least-squares linear regressions.

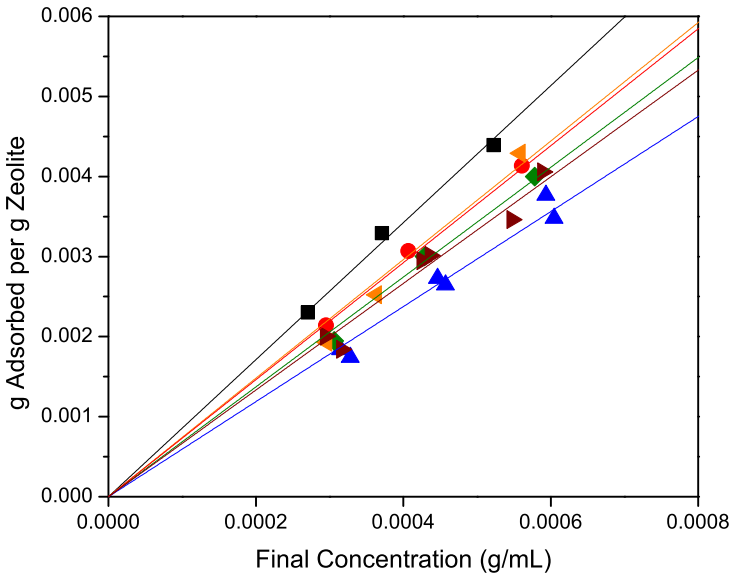

Figure 4.3: Adsorption isotherms for 1,3-propanediol on H-MFI at 278 (■), 283 (●), 288 (◀), 293 (♦), 298 (▶), and 303 (▲) K. Solid lines represent least-squares linear regressions.

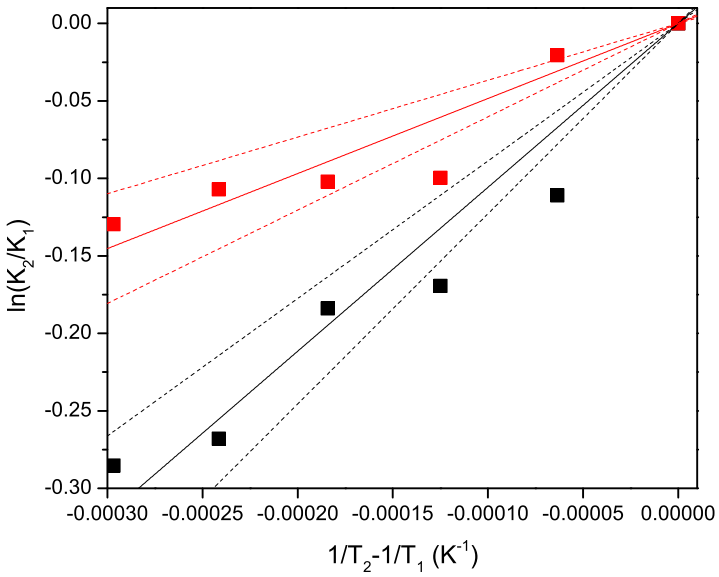

Figure 4.4: van't Hoff plots for propylene glycol transfer to H-MFI (■) and H-BEA (■) from aqueous solutions when T_1 is set as 278 K. Solid lines represent least-squares linear regressions and dashed lines represent 95% confidence intervals.

process entropy change (ΔS) can be calculated for each isotherm using

$$\ln K_{ads} = \Delta H - T\Delta S. \tag{4.2}$$

The entropies calculated at each temperature for a single zeolite/adsorbate system were averaged and are reported with their corresponding enthalpies in Figure 4.6. It can be observed for all systems that transfer from the bulk to the zeolite is slightly exothermic with enthalpies ranging from -4 to -10 kJ mol^{-1}.

It can also be noted that propylene glycol and 1,3-propanediol lose entropy upon transfer to H-MFI (-14 and -18 J mol^{-1} K^{-1}, respectively) whereas an entropy gain of 5 J mol^{-1} K^{-1} is found for propylene glycol transfer to H-BEA. This is surprising since the propylene glycol molecule should be highly confined in the 5.6 Å [12] pores of H-BEA. Clearly, strong hydrogen-bonding between propylene glycol and water in the bulk results in a highly constrained configuration for propylene glycol in solution. It is possible that the hydrophobic zeolite pores prohibit significant water adsorption, thereby allowing propylene glycol to acquire more degrees of freedom upon transfer from solution to the zeolite.

There is a precedence for positive transfer entropies of a solute from an aqueous phase to a hydrophobic zeolite phase. Ching and Ruthven obtained positive enthalpies for transfer of

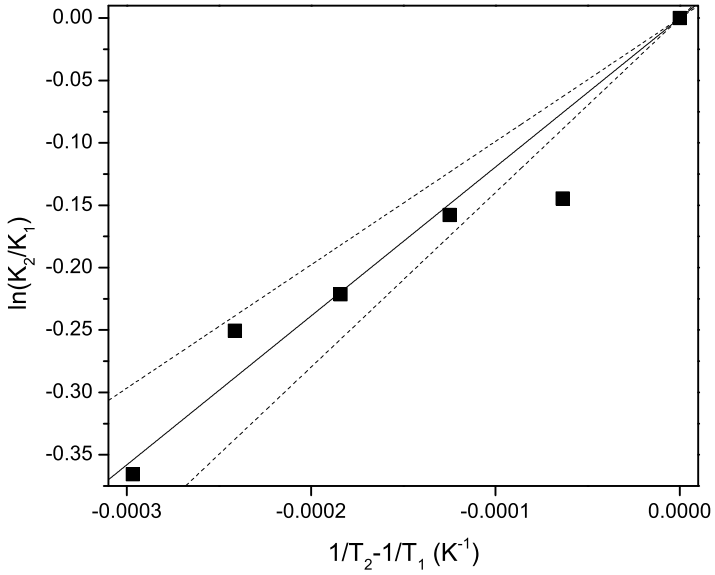

Figure 4.5: van't Hoff plot for 1,3-propanediol transfer to H-MFI (■) from aqueous solutions when T_1 is set as 278 K. Solid lines represent least-squares linear regressions and dashed lines represent 95% confidence intervals.

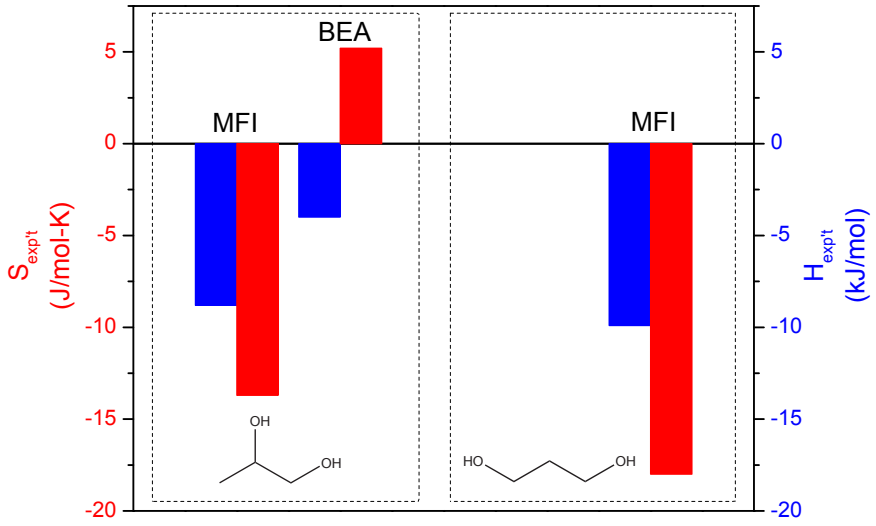

Figure 4.6: Enthalpies and entropies for transfer of propylene glycol (left) and 1,3-propanediol (right) onto H-MFI and H-BEA from aqueous solutions.

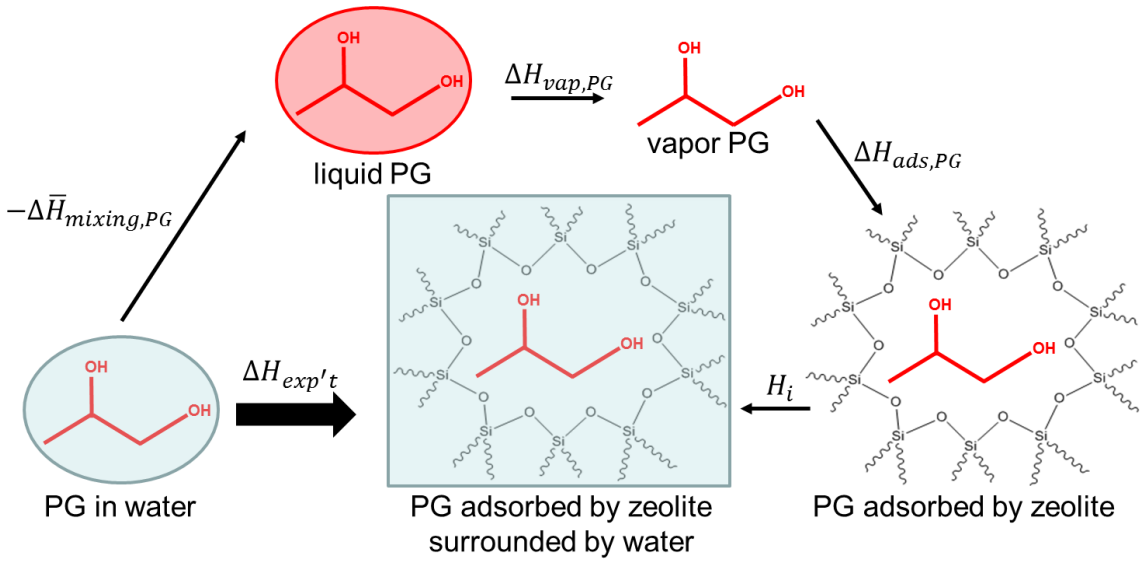

Figure 4.7: Proposed thermodynamic cycle for extraction of ΔH_{ads} for propylene glycol (PG)

glucose (27 kJ mol^{-1}) and fructose (21 kJ mol^{-1}) onto NaX from aqueous solutions through modeling of chromatography response curves at temperatures ranging from 274-225 K.[94] Although the authors did not report entropies, they can be calculated from their data and are found to be 67 and 51 J mol^{-1} K^{-1} for glucose and fructose on NaX, respectively, thus indicating that transfer of these sugars from water to NaX is an entropically driven process.

4.3.2 Calculating ΔH_{ads} from Aqueous Solution Adsorption Isotherms

A thermodynamic cycle is proposed in Figure 4.7 in order to obtain vapor adsorption enthalpies and entropies for the C_3 diols which are necessary for interpretation of reaction kinetic data.

The steps in the cycle include: 1) removal of the diol from the aqueous solution, 2) vaporization of the diol, and 3) adsorption of the diol into the zeolite pores. A fourth step, immersion of the zeolite into water (H_i), is neglected in our calculations since a calorimetric study by Barrer and Cram[95] found water immersion enthalpies of NaX, NaY, NaA, and (Ca,Na) chabazite ranging from 1.2-2.9$\times 10^{-5}$ kJ (mol H_2O)$^{-1}$, which only amounts to 0.01 kJ (mol propylene glycol)$^{-1}$. This assumption is further supported on the basis of a transmission infrared spectroscopy study that showed water does not disrupt adsorbed methanol on H-MFI ,[40] and a combined thermogravimetric-calorimetric (TGA-DSC) study that found methanol adsorbs with an enthalpy up to 40 kJ mol^{-1} greater than water on H-MFI.[23] Therefore, the vapor adsorption enthalpy for the C_3 diols, $\Delta H_{\text{ads,diol}}$, can be

calculated as

$$\Delta H_{ads,diol} = \Delta H_{exp't} + \Delta \bar{H}_{mixing,diol} - \Delta H_{vap,diol}, \tag{4.3}$$

where $\Delta H_{\mathrm{exp't}}$ is the enthalpy calculated from the aqueous adsorption isotherms, $\Delta \bar{H}_{\mathrm{mixing,diol}}$ is the diol partial molar heat of mixing, and $\Delta H_{\mathrm{vap,diol}}$ is the diol heat of vaporization.

Each enthalpic change outlined in Figure 4.7 and Equation 4.3 needs to be determined in order to calculate the enthalpy of adsorption. Separation of the diol from water is defined as $-\Delta \bar{H}_{\mathrm{mixing,diol}}$, which is equal to $\bar{H}^{\mathrm{E}}_{\mathrm{diol}}$, the diol partial molar excess enthalpy, as shown in Section 4.5.1. Matsumuto *et al.* used solution calorimetry to obtain excess enthalpies for propylene glycol and 1,3-propanediol in binary solutions with water at 298 K.[96] The authors obtained excess enthalpies as a function of diol mole fraction, fit the data with a Redlich-Kister equation, and reported the fitting parameters obtained. These same parameters were used to calculate excess enthalpies of -10.3 kJ (mol propylene glycol)$^{-1}$ and -8.4 kJ (mol 1,3-propanediol)$^{-1}$ for our systems as reported in Table 4.1. It should be noted that these values are equal to the infinite-dilution excess enthalpies calculated by Matsumoto *et al.* , which considers that our isotherms were measured under infinite-dilution conditions. The vaporization enthalpies of propylene glycol (71 kJ mol^{-1})[97] and 1,3-propanediol (72 kJ mol^{-1})[98] were taken from the NIST WebBook[99], and these values were originally obtained by Knauth and Sabbah using calorimetry.

Table 4.1: Enthalpies for propylene glycol and 1,3-propanediol adsorption on H-MFI and H-BEA reported in units of kJ mol^{-1}.

adsorbate	**zeolite**	$\Delta H_{\mathrm{exp't}}$	$\Delta \bar{H}_{\mathrm{mixing}}$ [96]	ΔH_{vap} [99]	ΔH_{ads}
Propylene glycol	H-MFI	-9	-10.3	71	-90
	H-BEA	-4			-85
1,3-Propanediol	H-MFI	-10	-8.4	72	-90

The heat of adsorption of propylene glycol for H-MFI calculated from the proposed thermodynamic cycle is ∼5 kJ mol^{-1} more exothermic than the enthalpy obtained on H-BEA (see Table 4.1). This result is consistent with the trends observed for alkane adsorption on zeolites. TGA-DSC studies found that alkane adsorption enthalpies become more exothermic with a decrease in zeolite pore size, and this has been attributed to an increase in dispersion forces due to confinement.[14,15] Denayer *et al.* used tracer and perturbation chromatographic techniques to obtain Henry's constants for C_5 to C_8 linear and branched alkanes on H-MFI and H-BEA at 473-648 K.[20] The adsorption enthalpies calculated from the temperature dependence of the Henry's constants on H-MFI were, in all cases, 3-10 kJ

mol^{-1} more exothermic then the enthalpies found with H-BEA, which supports the trend identified for propylene glycol in this study. Furthermore, the adsorption enthalpies for isopentane, which has a molecular weight within 5% of propylene glycol and comparable symmetry, were reported to be -51 and -56 kJ mol^{-1} on H-BEA and H-MFI, respectively, which represents a -5 kJ mol^{-1} change, and thus is in quantitative agreement with the results for propylene glycol adsorption.

Comparison of the isopentane adsorption enthalpies reported by Denayer *et al.*[20] with the propylene glycol adsorption enthalpies also allows for a quantitative assessment of the effect of exchanging terminal and secondary methyl (-CH_3) groups with polar hydroxyl (-OH) groups. It is found that the adsorption enthalpy of propylene glycol is 34 kJ mol^{-1} more exothermic than that of isopentane on both H-MFI and H-BEA, which is a -17 kJ mol^{-1} change upon exchange of a methyl group with a hydroxyl group.

This increase in exothermicity with the addition of hydroxyl groups is alluded to in alkane and alcohol adsorption literature, but our findings are quantitatively disparate. For example, Lee *et al.* reported an initial heat of adsorption (less than 0.3 molecules adsorbed per unit cell) for propanol on H-MFI of -145 kJ mol^{-1} at 400 K.[23] Quantitative comparison of this value with the -54 kJ mol^{-1} adsorption enthalpy reported by Eder *et al.* for butane on H-MFI at 323 K[14] indicates that exchanging a methyl group with a hydroxyl group results in a -87 kJ mol^{-1} change in adsorption enthalpy, which is more than 5 times greater than the number we report here. Vapor phase calorimetric measurements of alkanes and polyols on a single H-MFI material would not only elucidate the actual enthalpy change associated with exchange of methyl and hydroxyl functional groups, they would also test the validity of calculating vapor adsorption enthalpies from aqueous solution isotherms.

The effect of branching can also be explored through the diol adsorption enthalpies presented here. The adsorption enthalpies of propylene glycol and 1,3-propanediol on H-MFI are both found to be -90 kJ mol^{-1}, so a change in adsorption enthalpy with hydroxyl group location is not discerned with this method. This is in contrast with what has been observed for linear and branched alkane adsorption on H-MFI. Eder *et al.* used TGA-DSC to find that the adsorption enthalpies for butane (-58 kJ mol^{-1}) and pentane (-70 kJ mol^{-1}) are -6 kJ mol^{-1} more exothermic than their branched counterparts, iso-butane (-52 kJ mol^{-1}) and iso-pentane (-64 kJ mol^{-1}), respectively.[14]

It should be noted that errors in the other enthalpic terms in Equation 4.3 could obscure heat of adsorption differences due to branching. When making quantitative comparisons of the calculated heats of adsorption for a single adsorbate across different zeolites, errors with the solution mixing or vaporization enthalpies do not have an effect. That is, any difference in the adsorption enthalpies calculated are attributable only to differences in the zeolites, not inaccuracies in the mixing or vaporization enthalpies. However, a small error associated

with the heat of mixing or heat of vaporization of either propylene glycol or 1,3-propanediol would convolute any heat of adsorption differences between these two molecules on H-MFI. For example, a vaporization enthalpy of 71 kJ mol^{-1} was used for propylene glycol; but, if the value reported by the Dow Chemical Company was used (67 kJ mol^{-1} at 298 K)[100], this would result in an adsorption enthalpy of -86 kJ mol^{-1}, and hence a 4 kJ mol^{-1} shift due to exchange of a terminal with a secondary hydroxyl group. Therefore, the effect of hydroxyl group location on diol adsorption enthalpy would be best identified through vapor calorimetric experiments.

4.3.3 Calculating ΔS_{ads} from Aqueous Solution Adsorption Isotherms

It is also possible to calculate the entropy of adsorption, $\Delta S_{\text{ads,diol}}$, from aqueous solution isotherms. The same thermodynamic cycle (see Figure 4.7) is applied to obtain a relationship analogous to that reported in Equation 4.3 between $\Delta S_{\text{ads,diol}}$, the transfer entropy ($S_{\text{exp't}}$), partial molar entropy of mixing ($\Delta \bar{S}_{\text{mixing,diol}}$), and entropy of vaporization ($\Delta S_{\text{vap,diol}}$):

$$\Delta S_{ads,diol} = \Delta S_{exp't} + \Delta \bar{S}_{mixing,diol} - \Delta S_{vap,diol}. \tag{4.4}$$

Note that entropy contributions from immersion of the zeolite in water (S_i) have been neglected. $\Delta S_{\text{vap,diol}}$ can be readily calculated from $\Delta H_{\text{vap,diol}}$ and the boiling point, $T_{\text{B,diol}}$, at ambient conditions, since

$$\Delta G_{vap,diol} = \Delta H_{vap,diol} - T_{B,diol}\Delta S_{vap,diol} = 0. \tag{4.5}$$

Since the heat of vaporization is not a strong function of temperature, the $\Delta H_{\text{vap,diol}}$ values at 298 K (see Table 4.1) were used with the diol boiling points (461 and 488 K for propylene glycol and 1,3-propanediol, respectively) to calculate the $\Delta S_{\text{vap,diol}}$ values reported in Table 4.2

Table 4.2: Entropies for propylene glycol and 1,3-propanediol adsorption on H-MFI and H-BEA reported in units of J mol^{-1} K^{-1}.

adsorbate	**zeolite**	$\Delta S_{\text{exp't}}$	$\bar{S}^{\text{E}}$	$\Delta \bar{S}^{id}_{\text{mixing}}$	$\Delta \bar{S}_{\text{mixing}}$	ΔS_{vap}	ΔS_{ads}
Propylene glycol	H-MFI	-14	-35	-77±5	-112±5	154	-280±5
	H-BEA	5					-261±5
1,3-Propanediol	H-MFI	-18	-28		-105±5	148	-271±5

Calculation of $\Delta \bar{S}_{\text{mixing,diol}}$ is different from calculation of $\Delta \bar{H}_{\text{mixing,diol}}$ since the entropy

of mixing for an ideal solution, $\Delta\bar{S}^{\mathrm{id}}_{\mathrm{mixing,diol}}$, is non-zero (recall from Section 4.5.1 that enthalpy of mixing is zero for ideal solutions). That is,

$$\Delta\bar{S}_{mixing,diol} = \bar{S}^{E}_{diol} + \Delta\bar{S}^{id}_{mixing,diol}, \tag{4.6}$$

where $\bar{S}^{\mathrm{E}}_{\mathrm{diol}}$ is the diol partial molar excess entropy and $\Delta\bar{S}^{\mathrm{id}}_{\mathrm{mixing,diol}}$ is defined as

$$\Delta\bar{S}^{id}_{mixing,diol} = -R\ln x_{diol}, \tag{4.7}$$

where R is the universal gas constant and x_{diol} is the diol mole fraction in solution. Mole fractions of the C_3 diols in water ranged from 5×10^{-5} to 2×10^{-4} (see Figures 4.1-4.3) giving $\Delta\bar{S}^{\mathrm{id}}_{\mathrm{mixing,diol}}$ values ranging from -72 to -82 J mol^{-1} K^{-1}, and the average value is reported in Table 4.2.

$\bar{S}^{\mathrm{E}}_{\mathrm{diol}}$, the diol partial molar excess entropy, can be obtained from the diol partial molar excess enthalpy ($\bar{H}^{\mathrm{E}}_{\mathrm{diol}}$) and activity coefficient (γ_{diol}), since

$$\bar{G}^{E}_{diol} = \bar{H}^{E}_{diol} - \mathrm{T}\bar{S}^{E}_{diol} = RT\ln\gamma_{diol}, \tag{4.8}$$

where $\bar{G}^{\mathrm{E}}_{\mathrm{diol}}$ is the diol partial molar excess energy and T is the system temperature. Since it was shown in Section 4.3.2 that infinite dilution excess enthalpies were appropriate for our analysis, infinite dilution activity coefficients reported by Suleiman *et al.* (equal to 1 for propylene glycol and 1,3-propanediol)[87] were used in the calculation of $\bar{S}^{\mathrm{E}}_{\mathrm{diol}}$ from Equation 4.8, and these are also reported in Table 4.2.

Using Equation 4.4, ΔS_{ads} values of -280 and -261 J mol^{-1} K^{-1} were obtained for propylene glycol on H-MFI and H-BEA, respectively, and a value of -271 J mol^{-1} K^{-1} was obtained for 1,3-propanediol on H-MFI. A brief analysis demonstrates that the entropies calculated are reasonable. Molar entropies for liquid ethanol, ethylene glycol, propanol, and isopentane at standard conditions reported in the NIST WebBook[101] are shown in Table 4.3. Although molar entropy for propylene glycol is not available, on the basis of the entropies in Table 4.3 it is expected that this C_3 diol will have a molar entropy of $\sim$200 J mol^{-1} K^{-1}. Since ΔS_{vap} for propylene glycol has been identified as 154 J mol^{-1} K^{-1}, this means that vapor propylene glycol has a molar entropy of $\sim$200+154=354 J mol^{-1} K^{-1} which is reasonable since the vapor molar entropy for the smaller C_2 diol, ethylene glycol,[101] is 312 J mol^{-1} K^{-1}. Furthermore, if vapor propylene glycol has a molar entropy of 354 J mol^{-1} K^{-1}, then a ΔS_{ads} value of -261-280 J mol^{-1} K^{-1} is possible.

Like ΔH_{ads}, trends for ΔS_{ads} with changing zeolite or adsorbate can be analyzed relative to literature for alkane adsorption to elucidate the roles of zeolite and adsorbate properties on adsorption. Although Denayer *et al.*[20] did not calculate ΔS_{ads} values with their chromatographic adsorption study, they did report pre-exponential factors, K'_0, defined as

Table 4.3: Vapor phase molar entropy values reported by NIST WebBook

Molecule	**Molecular entropy S^0 (J/mol-K)** [101]
Ethanol	159.86 - 177.0
Ethylene glycol	166.9 – 179.5
Propanol	192.8 – 214.2
Isopentane	254.4 – 261.04

$$K_0' = \exp\left[\frac{\Delta S^{\ominus}_{0,local}}{R} + \ln\left(\frac{n_T}{2p^{\ominus}}\right)\right], \tag{4.9}$$

where $\Delta S^{\ominus}_{0,\text{local}}$ is the entropy of adsorption at zero coverage, n_T is the total number of adsorption sites, and $p^{\ominus}$ is ambient pressure. From Equation 4.9, one can see that as $\Delta S^{\ominus}_{0,\text{local}}$ becomes more negative (greater loss of entropy upon adsorption), K_0' decreases. Denayer *et al.* found smaller K_0' values on H-MFI than on H-BEA for all C_5-C_8 linear and branched alkanes studied indicating that alkanes lose more entropy upon adsorption on H-MFI than on H-BEA, and this is in agreement with our findings for propylene glycol. A comparison of the K_0' values reported for isopentane adsorption on H-MFI and H-BEA provide further support for our findings. If one makes the assumption that the n_T values for isopentane on H-MFI and H-BEA are equal, then one can calculate the difference between the $\Delta S^{\ominus}_{0,\text{local}}$ values for each system, since

$$\frac{K_{0,1}'}{K_{0,2}'} = \exp\left[\frac{\Delta S^{\ominus}_{0,local,1} - \Delta S^{\ominus}_{0,local,2}}{R}\right]. \tag{4.10}$$

Using Equation 4.10, it is found that 22 J mol^{-1} K^{-1} more entropy is lost for isopentane adsorption on H-MFI than on H-BEA, which validates the 19 J mol^{-1} K^{-1} greater entropy loss identified for propylene glycol on H-MFI versus H-BEA (see Table 4.2).

When making the same comparison between K_0' values for n- and iso-pentane, it is found that the pre-exponential factors for isopentane are smaller than those for n-pentane on H-MFI and H-BEA, meaning that isopentane loses more entropy upon adsorption than its linear counterpart (note that this difference is not greater than the measurement error reported by Denayer *et al.*). This is again in agreement with our results wherein it was identified that propylene glycol loses more entropy than the linear diol, 1,3-propanediol. The entropic differences due to increasing alkane branching calculated using Equation 4.10 only amount to -0.2 and -1.7 J mol^{-1} K^{-1} on H-BEA and H-MFI, respectively. While a -9 J mol^{-1} K^{-1} entropic difference is found with increasing diol branching in this study, it should be noted that this value is very sensitive to errors in the terms in Equation 4.4. Therefore,

it is recommended that vapor adsorption calorimetry is performed to obtain ΔS_{ads} values, which can be used to validate the results presented here.

4.4 Conclusions

Aqueous adsorption isotherms for propylene glycol and 1,3-propanediol on commercial H-MFI and H-BEA, from 293-303 K, were presented, and it was identified that transfer from the bulk to the zeolite is an exothermic process ranging from -4 to -10 kJ mol^{-1} for all systems studied. While the process was exothermic in all cases here, it was found that transfer of propylene glycol from the bulk to H-BEA is partially driven by an entropy increase of 5 J mol^{-1} K^{-1}, while transfer of propylene glycol and 1,3-propanediol to H-MFI resulted in entropy decreases of -14 and -18 J mol^{-1} K^{-1}, respectively.

A thermodynamic cycle was proposed which allowed for calculation of vapor adsorption enthalpies from aqueous adsorption isotherms. As with branched alkanes, propylene glycol adsorption enthalpy became -5 kJ mol^{-1} more exothermic from H-BEA to H-MFI, indicating that the increase in K_{ads} is partially driven by enthalpy. Vapor heats of adsorption for propylene glycol and 1,3-propanediol on H-MFI were calculated as -90 kJ mol^{-1}, which was unexpected since an adsorption enthalpy change of -6 kJ mol^{-1} is associated with increasing alkane branching on H-MFI.

Extraction of ΔS_{ads} values using the same thermodynamic cycle resulted in a 19 J mol^{-1} K^{-1} greater entropy loss for propylene glycol on H-MFI than on H-BEA, which also demonstrates increased confinement on H-MFI. A -9 J mol^{-1} K^{-1} change was found with increasing branching by comparing entropies for 1,3-propanediol and propylene glycol adsorption on H-MFI. This result, like the adsorption enthalpies described above, indicates that hydroxyl group location does not have a significant effect on adsorption affinity

Solution calorimetric studies could be performed to verify the transfer enthalpies reported here. Vapor phase isotherms at multiple temperatures or vapor phase TGA-DSC could be used to assess the accuracy of the calculated adsorption enthalpies. Agreement between vapor phase measurements and the adsorption enthalpies calculated here would validate this approach.

4.5 Supporting Information

4.5.1 Relationship between Solution Excess Enthalpy (H^{E}) and the Heat of Mixing (ΔH_{mixing})

Excess enthalpy, H^{E}, is defined as

$$H^E = H - H^{id}, \tag{4.11}$$

where H is the actual solution enthalpy and H^{id} is the ideal solution enthalpy. The enthalpy of mixing, $\Delta H_{\mathrm{mixing}}$, is defined as

$$\Delta H_{mixing} = H - H_{pure}, \tag{4.12}$$

where H_{pure} is a linear combination of the pure component enthalpies. For an ideal mixture, $\Delta H_{\mathrm{mixing}}$ is 0, and Equation 4.12 becomes

$$0 = H^{id} - H_{pure}. \tag{4.13}$$

Therefore, $H^{\mathrm{id}} = H_{\mathrm{pure}}$, and, from Equations 4.11 and 4.12, it is clear that $H^{\mathrm{E}} = \Delta H_{\mathrm{mixing}}$. This means that an analogous relationship is defined for individual species in solution, or

$$\Delta \bar{H}_{mixing,diol} = \bar{H}^E_{diol}, \tag{4.14}$$

where $\Delta \bar{H}_{\mathrm{mixing,diol}}$ is the diol partial molar heat of mixing, and $\bar{H}^{\mathrm{E}}_{\mathrm{diol}}$ is the diol partial molar excess enthalpy.

4.5.2 Errors Associated with van't Hoff Plot Normalization

The Henry's constants, K_{ads}, obtained from the adsorption isotherms in Figures 4.1-4.3 were normalized to the Henry's constant at 278 K for each adsorbate/zeolite system, and these ratios were presented in the van't Hoff plots in Figures 4.4 and 4.5. Van't Hoff plots, obtained when each K_{ads} is normalized to the Henry's constant at 293 K, are shown in Figures 4.8 and 4.9.

Transfer enthalpies were calculated using Equation 4.1, and resulted in adsorption enthalpies of -89 kJ mol^{-1} and -85 kJ mol^{-1} for propylene glycol on H-MFI and H-BEA, respectively, and -89 kJ mol^{-1} for propylene glycol on H-MFI. All these values are within 1 kJ mol^{-1} of the values calculated with 278 K as the reference temperature (see Table 4.1), and, therefore, the reference temperature does not significantly impact the analyses.

4.5.3 Design of Aqueous Solution Calorimetry Experiments

It was proposed that aqueous solution calorimetric experiments could be performed to verify the enthalpies reported from solution adsorption isotherms in Section 4.3.2. In order to determine the feasibility of using solution calorimetry to measure transfer enthalpies, the

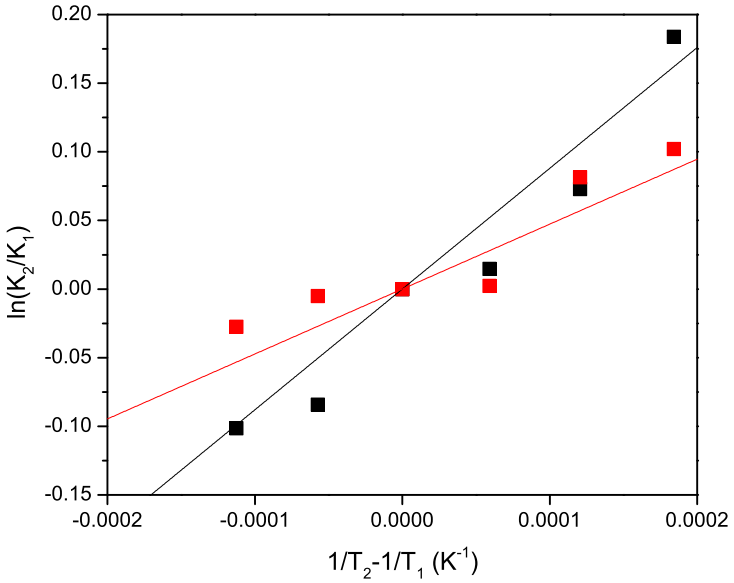

Figure 4.8: van't Hoff plots for propylene glycol transfer to H-MFI (■) and H-BEA (■) when T_1 is set as 293 K. Solid lines represent least-squares linear regressions.

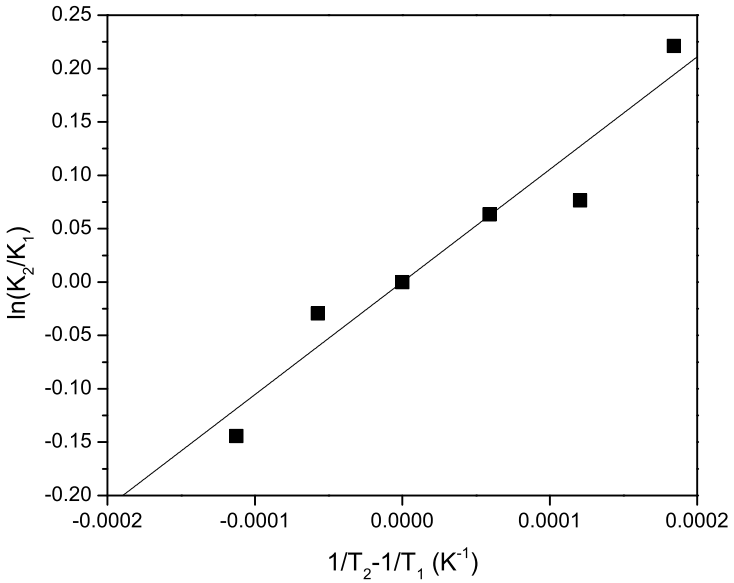

Figure 4.9: van't Hoff plot for 1,3-propanediol transfer to H-MFI (■) when T_1 is set as 293 K. The solid line represents a least-squares linear regression.

amount of heat evolved needs to be calculated.

The relationship between the system heat, Q, and the transfer enthalpy, ΔH, is

$$dQ = C_p dT + \Delta H dn, \tag{4.15}$$

where C_p is the system heat capacity, T is temperature, and n are moles. By differentiating this equation with respect to a reference condition one obtains

$$\Delta Q = Q_f - Q_i = C_p(T_f - T_i) + \Delta H(n_f - n_i), \tag{4.16}$$

where Q_i, T_i, and n_i are the initial system heat, temperature, and number of moles, respectively, and Q_f, T_f, and n_f are the final system heat, temperature, and number of moles, respectively. If the calorimeter is isothermal, $T_f = T_i$ and Equation 4.16 becomes

$$\Delta Q = \Delta H(n_f - n_i). \tag{4.17}$$

Professor Alex Navrotsky's group has studied thermodynamics of zeolite formation by measuring their heats of dissolution in aqueous hydrofluoric acid (HF) with solution calorimetry. As a reference, the typical heat evolved in their experiments is calculated here. Piccione *et al.* performed these experiments with 0.18 mmol SiO_2 (10.8-13.7 mg zeolite) dissolved in 5.4 g of 25 wt% HF at 323 K.[102] A typical heat of dissolution reported by the group was -150 kJ (mol SiO_2)$^{-1}$, which results in a heat evolution of

$$\Delta Q = \left(\frac{-150kJ}{mol\ SiO_2}\right)(0.18\ mmol\ SiO_2)\left(\frac{1\ mol\ SiO_2}{1000\ mmol\ SiO_2}\right) = -27\ J. \tag{4.18}$$

When measuring the heat of adsorption in the Henry's law regime for propylene glycol (PG), the amount adsorbed on the surface amounts to ∼0.03 mmol PG per g zeolite. Using 1 mL of solution with 0.1 g of zeolite, this gives $\sim 3\times10^{-6}$ mol PG adsorbed. It is assumed on the basis of the results in Section 4.3.1 that the transfer enthalpy is -5 kJ (mol PG)$^{-1}$; so one obtains

$$\Delta Q = \left(\frac{-5kJ}{mol\ PG}\right)(3\times10^{-6}\ mol\ PG) = -0.015\ J. \tag{4.19}$$

If the solution volume and zeolite amount were scaled up 5-fold, this would result in -0.075 J evolved. Furthermore, if the solution concentration was raised, the amount adsorbed and, therefore, the heat evolution would increase. For example, if a coverage of 0.2 mmol PG per g zeolite was reached with 0.1 g of zeolite, this would give a heat evolution of -0.1 J. Again, if the solution volume and zeolite amount were scaled up by a factor of 10, this

would result in a factor of 10 increase in the heat released to -1 J.

Personal communication with Professor Alex Navrotsky indicates that a heat evolution of -1 J is within the limits of detection of their solution calorimeter, and, therefore, this is a potential method for validating the transfer enthalpies presented here.

CHAPTER

FIVE

PROBING THE RELATIONSHIP BETWEEN SILANOL DEFECTS, SILICALITE-1 SYMMETRY, AND POLYOL ADSORPTION PROPERTIES

5.1 Introduction

Zeolites can discriminate between molecules on the basis of size and functionality which has led to their use as highly selective catalysts and adsorbents in petroleum refining, petrochemical synthesis, and environmental protection applications.[13] This capability also gives zeolites the potential to be effective adsorbent and membrane materials for the separation of organic molecules from water which has applications in the conversion of biomass to chemicals and fuels.[8,103] Separation performance of zeolite membranes is described by the separation factor, α, which is a function of species volatility, diffusivity, and adsorption affinity.[17,104] A zeolite membrane with pores that are large enough to allow diffusion of organic molecules, but limit water adsorption, is required to achieve a high separation factor of organic molecules from water.

Silicalite-1, the siliceous analogue of the MFI framework, has been pursued as a potential membrane material due to its medium pore size ($\sim$ 5.6 Å)[12] and hydrophobic properties. Silicalite-1 does not contain Brønsted acid sites that can hydrogen bond with water, resulting in less than 3 molecules of water adsorbed per unit cell (representing only 10% of the total pore volume) at a reduced pressure of 0.5 as measured by gravimetry.[17] Although silicalite-1 does not adsorb appreciable amounts of water, it has been shown to adsorb C_2-C_6 polyols from aqueous solutions due to non-polar dispersion interactions between the adsorbate molecules and zeolite pore walls.[68,105] Silicalite-1 membranes also have a high separation selectivity (>100)[106] for ethanol removal from aqueous solutions due to this low affinity for water adsorption.[103]

Although silicalite-1 does not contain hydrophilic Brønsted acid sites, it has been shown to contain silanol defects which can also participate in hydrogen bonding with water.[17,29] The formation of zeolitic defect sites (siloxy groups and silanol nests) depends on factors such as the synthesis pH, temperature, and duration, as well as the number of alkali cations and the type of structure directing agent.[107] Silicalite-1 is commonly synthesized in basic media with OH^- ions as the mineralizing agent, which can result in as many as ∼17 silanol defects per unit cell.[108] Flanigen and Patton first synthesized silicalite-1 in presence of fluoride anions by a hydrothermal process,[109] and it was later shown by Chezeau *et al.* using ^{29}Si MAS NMR that the fluoride material does not contain Q^3 Si atoms, and is, therefore, free of Si-OH defects.[107]

While it has been determined that silanol defects increase water adsorption, the effect of these defects on polyol adsorption needs to be understood to fabricate efficient zeolite membranes for separation of oxygenates from water. Several authors have observed a decrease in alcohol adsorption enthalpy with increasing coverage on silicalite-1, which they have postulated to be the result of interactions between alcohol molecules and silanol defects. Lee *et al.*[23], Dubinin *et al.*[25], and Thamm[24] used calorimetry and gravimetry to find that the heats of adsorption for linear C_1-C_3 alcohols on silicalite-1 were -90-100 kJ mol^{-1} at initial loadings (less than 0.3 molecules per unit cell) and decreased monotonically with coverage. Thamm also observed that the differential enthalpy of adsorption for methanol and 1-propanol on silicalite-1 decreased by 40-50% in a step-like transition with an inflection at 0.17 mmol g^{-1}, or approximately 1 molecule per unit cell, and suggested that this coverage could be commensurate with the number of internal silanol defects. These observations are consistent with initial interactions of alcohols with silanols that would result in the highest adsorption enthalpy, and the filling of less favorable sites with increasing coverage.

The effect of silanols on the uptake of ethanol on silicalite-1 has been probed in two studies that provide contrasting results. Although characterization data are not included, Chen *et al.* claim to have healed defects by treating silicalite-1 with steam saturated air at 1073 K for 100 h.[30] They then show that vapor ethanol adsorption at 293 K is suppressed by ∼25% at all pressures studied (∼0.03-0.94 reduced pressure) by the steam-healing of defects. Zhang *et al.* recently used gravimetry to obtain vapor adsorption isotherms for water and ethanol at 298-328 K on silicalite-1 materials synthesized via alkaline and fluoride routes.[17] The authors found that water adsorption capacity on the fluoride material was only 12.6% of the capacity of the alkaline material at a reduced pressure of 0.95, and attributed this decrease in capacity to a decrease in the number of hydrophilic silanol groups. However, they found that ethanol adsorption at pressures greater than 0.05 P/P_0 was insensitive to the silicalite-1 synthesis method, and thus concluded that the number of hydrophilic groups on the zeolite surface does not affect ethanol uptake.

Here we present vapor phase and aqueous solution adsorption isotherms on several silicalite-1 materials to quantify the effect of silanol defects on polyol adsorption. We show via SEM, XRD, and ^{29}Si MAS NMR that we have synthesized a series of silicalite-1 materials with silanol groups that vary in concentration from ∼8.5 to 0 (undetectable) Si-OH per unit cell. We demonstrate that a decrease in the number of defects is correlated with the evolution of a step in the Ar 87 K adsorption isotherm at 10^{-3} reduced pressure, which may indicate a relationship between the number of Si-OH groups and the dominant silicalite crystal structure. Aqueous solution and vapor adsorption data for a variety of polyol/silicalite-1 systems are presented to show that silanol defects enhance adsorption by over an order of magnitude in the Henry's law regime for all molecules studied. K_{ads} for C_2-C_4 aqueous polyol adsorption is found to be linearly correlated with the number of silanol defects, which demonstrates that the adsorbates preferentially interact with defect sites.

5.2 Methods

Two silicalite-1 synthesis procedures employing different silica sources, mineralizers, synthesis times, and temperatures were followed to obtain silicalite-1 materials with different properties and structures (see Table 5.1).

Table 5.1: Summary of the synthesis methods, material treatments, and structural and chemical characterization data for the silicalite-1 adsorbents.

Silicalite-1 name	Synthesis procedure	Post treatment[a]	Crystal symmetry at ambient temperature[b]	Si-OH/uc[c]	Pore volume (cc/g)[d]
Si[OH]	Alkaline	Calcined	Orthorhombic	8.5	0.345
S1	Alkaline	Calcined, Steamed 1 hr	Orthorhombic/ Monoclinic	3.9	0.312
S2	Alkaline	Calcined, Steamed 2hrs	Monoclinic	2.9	0.404
Si[F]	Fluoride	Calcined	Monoclinic	0	0.216

[a]Calcination and steaming procedures described in Section 5.2. [b]Symmetry inferred from XRD and ^{29}Si MAS NMR. [c]Calculated from ^{29}Si MAS NMR spectra. [d]Obtained from NLDFT fitting of Ar 87 K adsorption isotherms.

The starting molar ratio for the Si[F] silicalite-1 solution was $1SiO_2$: $0.08TPABr$: $0.4NH_4F$: $20H_2O$. Tetrapropylammonium bromide (1.66 g, TPABr, 98%, Aldrich) was added to 27.62 g of distilled water, followed by the addition of 1.15 g of ammonium fluoride (NH_4F,

98%, J.T. Baker, Baker analyzed) and vigorously stirred at ambient conditions for 15 minutes. Then, 4.61 g of Silica (SiO_2, Cabosil M5, Riedel de Haën) was added, and the whole solution was mixed by hand with a spatula until the dense solution was homogeneous in color and texture. The dispersion was transferred into a 45 mL Teflon lined stainless steel autoclave and heated at 448 K for 7 days without rotation.[110]

The Si[OH] silicalite-1 was synthesized according to a previously published procedure.[111] Deionized water (28.95 g) was mixed with 3.54 g of tetrapropylammonium hydroxide (TPAOH, 1M, Aldrich) under stirring at room temperature. Then, 2.51 g of tetraethylorthosilicate (TEOS, 98 wt%, Aldrich) was slowly added, drop by drop, under stirring to obtain the final molar composition $1SiO_2$: 0.3TPAOH: $150H_2O$. After all of the TEOS had been added, the synthesis gel was stirred vigorously for 4 hours at room temperature. The resultant transparent solution was aged for 4 hours at 343 K in an oil bath without stirring. This final solution (35 ml) was filtered through a syringe membrane filter (nominal pore size 0.2 mm), sealed into a Teflon-lined stainless-steel autoclave, and crystallized for 24 hours at 454 K without rotation.

The zeolite powder obtained by these two different procedures was purified by repeated washing (dispersion in deionized water for 5 min in an ultrasonic bath) and centrifugation at ambient temperature until the supernatant pH was neutral (approximately 3 cycles). The solids were dried at 343 K in an oven for 48 h.

The silicalite-1 materials were ground with a mortar and pestle, and 0.6-1 g of material was placed in a $2\,{}^5/_8$"L $\times$ ${}^5/_8$"W $\times$ ${}^3/_8$"D quartz boat with 1-2 boats inserted in a horizontal 1" diameter quartz tube approximately 30" in length. The tube was heated by a cylindrical clamshell furnace equipped with 3 heating zones (Applied Test Systems, Inc., Series 3210 furnace). The silicalite-1 materials were treated under dry air flowing at $\sim$100 cm^3 min^{-1} by heating from ambient temperature to 823 K at a rate of 1 K min^{-1}, holding at 823 K for 20 h, and subsequently cooling to ambient temperature also under dry flowing air.

Silicalite-1 samples S1 and S2 were obtained by steaming the Si[OH] material with the same furnace set-up used for calcination; the synthesis conditions and properties for these materials are listed in Table 5.1. Approximately 0.6 g of Si[OH] material was placed in a single quartz boat and heated to 1073 K at a rate of 1 K min^{-1} under dry air flowing at 100 $cm^3\,min^{-1}$, steam treated by vaporizing water with a syringe pump at a rate of 0.2 cm^3 h^{-1} at 1073 K for 1 and 2 hours, respectively, and upon stopping water flow, cooling under dry air for 2 hours.

Scanning electron microscopy (SEM) observations were performed on the samples coated with platinum, using an Inspect F50 field emission gun scanning electron microscope operated at 5 and 10 kV. The phase purity and crystallinity of the samples were checked by powder X-ray diffraction (XRD) in a Bruker-AXS (Siemens) D5005, using CuKα radia-

tion (λ = 1.5418 Å), a graphite monochromator, 0.02° step size and 1 s integration time (dwell). Simulated XRD patterns for orthorhombic and monoclinic MFI were produced in Accelyrs' Materials Studio[112] using unit cell parameters and atomic positions reported by Van Koningsveld *et al.*[2,3]

^{29}Si magic angle spinning nuclear magnetic resonance spectroscopy (^{29}Si MAS NMR) spectra of the solids were performed at the Caltech Solid State NMR Facility on a Bruker DSX-500 spectrometer equipped with a Bruker 4 mm MAS NMR probe. The spectra were recorded with an 8 kHz spinning rate at a frequency of 99.5 MHz. The pulse length was 4.0 ms with a 60 s recycle delay. Quantification of the Q^3 (non-bonding Si defects) and Q^4 (Si-[$(OSi)_4$]) was performed by fitting the peaks using the Gaussian and Lorentz multiple peak fitting tool in Origin.[113]

Argon adsorption/desorption experiments were performed on the powdered zeolite samples at 87 K using a Quantachrome AS-iQ system. The materials were degassed and heated at a rate of 10 K min^{-1} to 323 K, soaking at 323 K for 30 minutes, heating at 10 K min^{-1} to 573 K, and soaking at 573 K for 1-5 hours until the outgassing rate was reduced below 50 mtorr min^{-1}. The samples were then analyzed for Ar adsorption and desorption in the range of 10^{-7} to 1 reduced pressure. Pore volumes were determined by fitting the adsorption isotherms with a non-local density functional theory (NLDFT) isotherm for Ar adsorption at 87 K on a zeolite with cylindrical pores.

Aqueous solution adsorption experiments were performed as described in Section 1.3. Vapor adsorption isotherms were collected with a Shimadzu TGA-50 thermobalance. Propylene glycol vapor was generated by flowing helium through two jacketed glass saturators in series held at a constant temperature ranging from 273-335 K using a Lauda Eco Gold RE 630 circulating chiller. The vapor pressure at each bubbler temperature was obtained by interpolating the vapor pressure data reported by Curme and Johnston.[114] Approximately 10 mg of calcined zeolite was placed in the balance and pretreated under helium flowing at 150 cm^3 min^{-1} to 773 K at a rate of 1 K min^{-1}. The zeolite was held at this temperature for 6 hours and subsequently the temperature was reduced to 333 K for the adsorption measurements. When a stable baseline was established, propylene glycol vapor was introduced to the sample chamber, and the equilibrium weight was recorded to calculate the amount adsorbed. The partial pressure of propylene glycol was then increased by increasing the saturator temperature to obtain additional points on the adsorption isotherm.

5.3 Results and Discussion

5.3.1 Effect of Synthesis and Steaming Conditions on Zeolite Structure and Defect Density

SEM and XRD analyses in Figures 5.1 and 5.2 indicate that all materials are crystalline MFI. The average crystal size along the *c*-axis of the crystals for Si[F] and Si[OH] were identified from SEM as ∼50 μm and ∼0.5 μm, respectively. Samples S1 and S2 have similar crystal shape and size as the parent sample, Si[OH], so it can be concluded that steaming does not affect the crystal morphology down to the 1 μm scale. The XRD patterns for the calcined silicalite-1 samples in Figure 5.2 indicate that all materials have the MFI framework.[12]

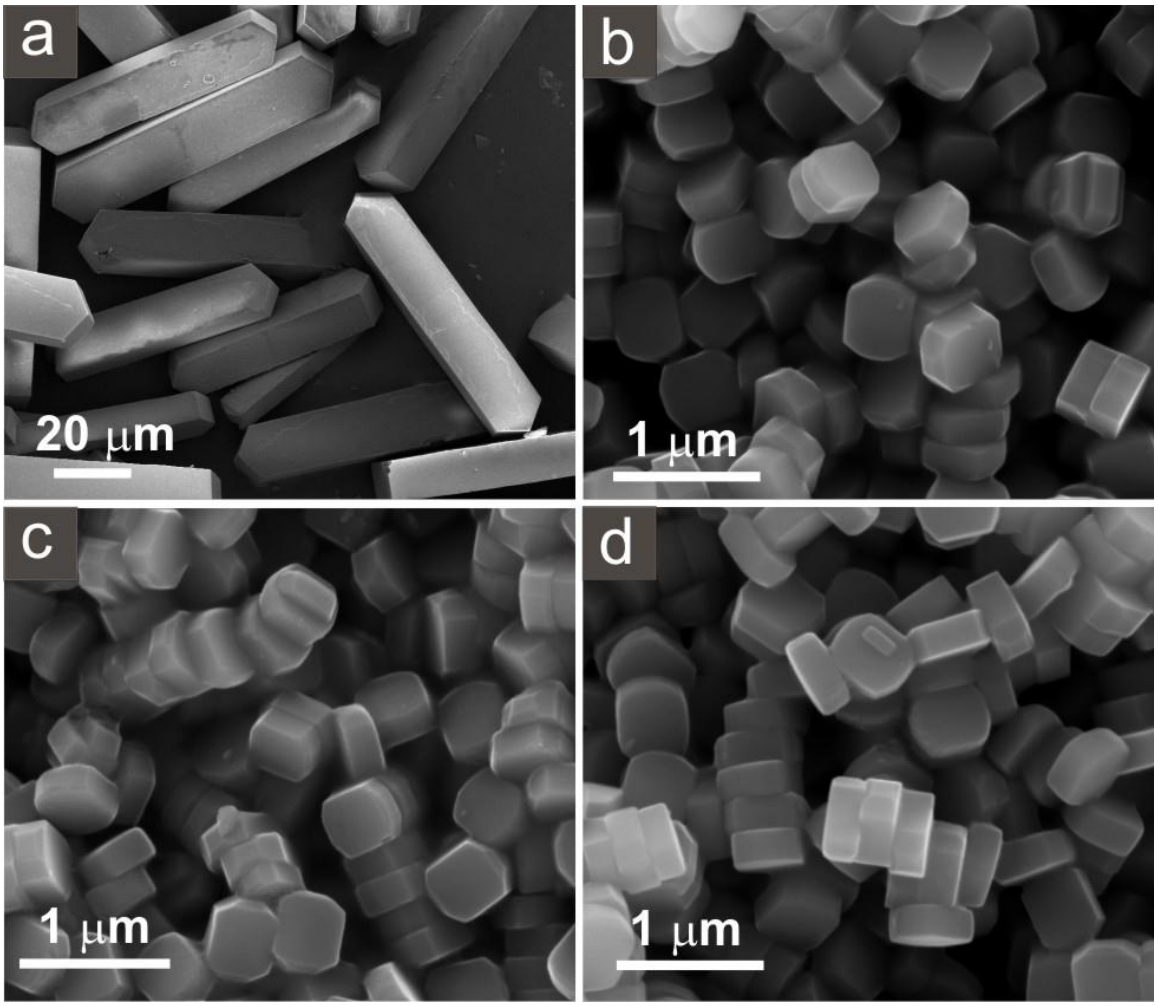

Figure 5.1: SEM images of the a) Si[F], b) Si[OH], c) S1, and d) S2 silicalite-1 crystals prepared using the conditions described in Table 5.1.

A comparison of the XRD patterns for the silicalite-1 materials, in the range of 22-25.2°

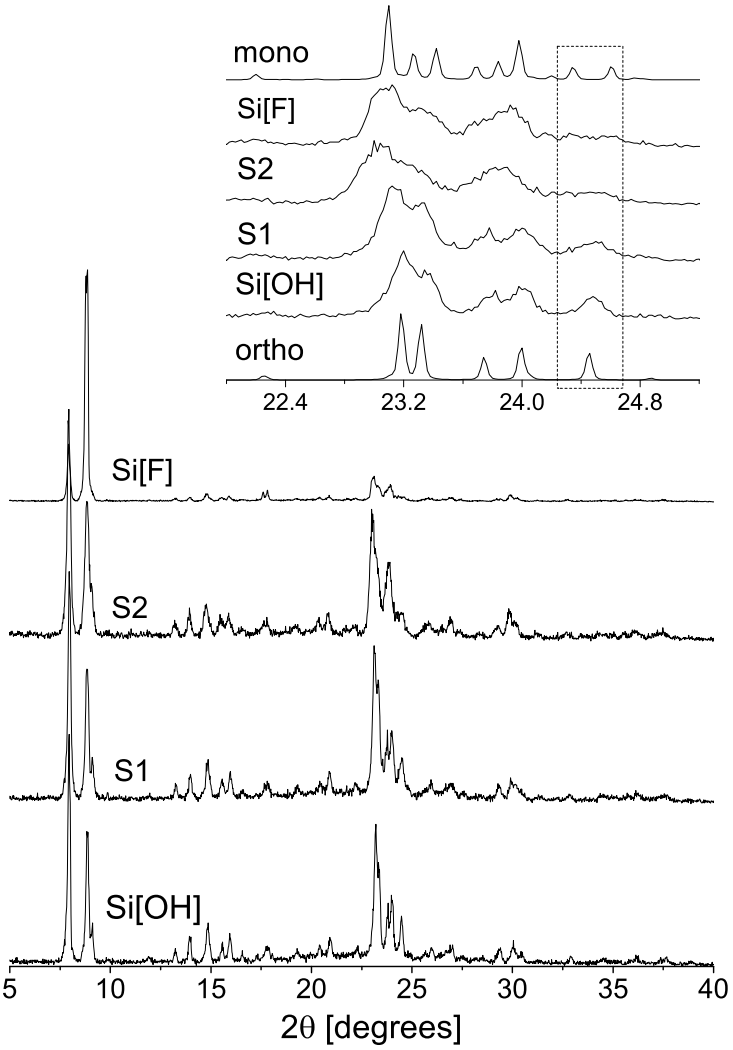

Figure 5.2: XRD of Si[OH], S1, S2, and Si[F]. Inset: Magnified view of Si[OH], S1, S2, and Si[F] XRD data compared with simulated monoclinic[2] and orthorhombic[3] MFI patterns.

2θ (see inset Figure 5.2) with simulated diffraction patterns for orthorhombic[3] and monoclinic[2] MFI, provide evidence that these materials, after calcination, differ in symmetry. It can be noted from the simulated orthorhombic and monoclinic diffraction patterns that a single peak is observed at $\sim$24.4° 2θ for the orthorhombic symmetry and this peak splits into a doublet for the monoclinic symmetry.[115–117] The single $\sim$24.4° 2θ peak is observed for Si[OH] silicalite indicating that this material is orthorhombic at ambient conditions. Other features which change with a transition from orthorhombic to monoclinic symmetry are splitting of the doublet peaks in the 23.0-23.5° and 23.6-24.2° 2θ ranges into triplets. Doublets are noted for Si[OH] and S1 silicalite samples indicating that these materials contain the orthorhombic phase, whereas triplets are found for S2 and Si[F] silicalite samples leading us to postulate these materials to be predominantly monoclinic as listed in Table 5.1

The silicalite-1 materials differ in both long- and short-range order as demonstrated by the ^{29}Si MAS spectra in Figure 5.3. The Si[OH] material has a main peak at -113 with a large shoulder at -115 ppm, which corresponds to Q^4 (Si-[$(OSi)_4$]) groups. The resolution of these lines increases with the steaming duration, which is indicative of an increase in local structural order. The Si[F] material exhibits the greatest number of resonances in this ppm range, 13, which is consistent with 24 crytallographically unique silicon sites for defect-free monoclinic silicalite-1.[118] As the resolution of the Q^4 lines increases, it can be observed that the non-bonded Si-OH defect (Q^3) peak at -103 ppm decreases in intensity (inset of Figure 5.3). The silanol concentrations for all samples were calculated from the relative peak areas and are reported in Table 5.1. The number of defects range from $\sim$8.5 to 0 per unit cell, and it is clear that steam treatment has partially healed the defects for S1 and S2.[119]

^{1}H-^{29}Si CPMAS and ^{1}H MAS spectra were also obtained for all silicalite-1 materials and are presented in Section 1.3. A peak at -102 ppm can be observed in the ^{1}H-^{29}Si CPMAS spectrum for the Si[OH] silicalite-1 (Figure 5.13) which is attributed to silanol defects.[29] The chemical shifts observed in the ^{1}H MAS NMR in Figure 5.14 result from either Si-OH defects ($\sim$1.3 ppm) or water molecules adsorbed on the surface (above 3 ppm).[119] These peaks are most prominent for the Si[OH] silicalite-1 material, and reduce in intensity and line width with an increase in steaming time. These data show that the defect density decreases in the order Si[OH] >S1 >S2 >Si[F] which is in agreement with the findings from the ^{29}Si MAS NMR experiments.

It is clear upon inspection of the Ar 87 K adsorption isotherms in Figure 5.4 that the number of defects is correlated with the evolution of a step at a reduced pressure of 10^{-3}. The Si[OH] argon adsorption isotherm is smooth with pore filling occurring at approximately 120 cc g^{-1}. Upon steamed treatment, a small step or hysteresis, which corresponds with 23-30 argon molecules per unit cell, can be observed. This step becomes larger with longer

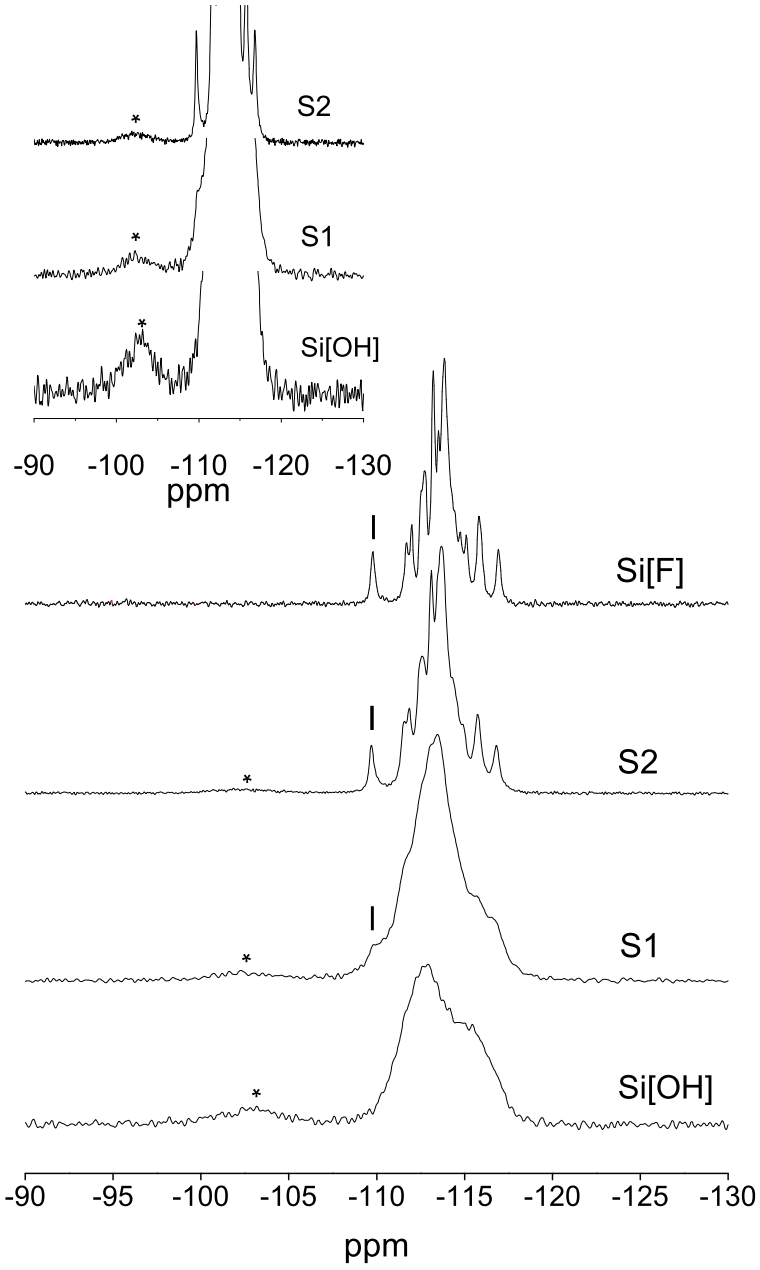

Figure 5.3: ^{29}Si MAS NMR of Si[OH], S1, S2, and Si[F]. Inset: Magnified view of the ^{29}Si MAS NMR Q^3 peak at -103 ppm of Si[OH], S1, and S2.

steaming time and is most prominent for the S2 and Si[F] materials.

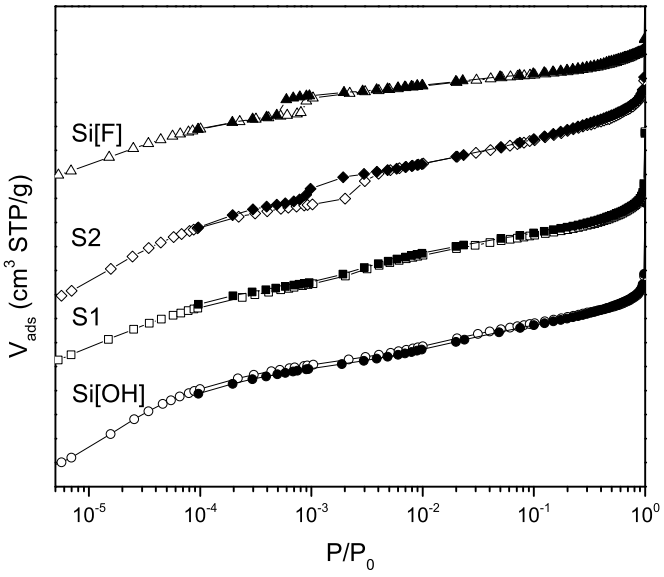

Figure 5.4: Argon adsorption (open symbols) and desorption (closed symbols) on Si[OH], S1, S2, and Si[F] at 87 K.

This step has been noted for volumetric argon adsorption on high silica H-ZSM-5[120–123] and silicalite-1.[117,120] Muller and Unger[124] and Llewellyn *et al.*[120] proposed that the step evolution corresponds to a fluid- to solid-like phase transition in the adsorbate. Muller and Unger were the first to report that argon adsorption at 77 K on H-ZSM-5 (alkaline-free synthesis, Si/Al>1000, 180 μm)[125] results in a Type I adsorption isotherm with an additional step at 10^{-3} reduced pressure (argon loading of 100 $cm^3\ g^{-1}$).[124] Llewellyn *et al.* later observed this step with silicalite-1 and H-ZSM-5 (fluoride synthesis, Si/Al>60, >27 μm)[126] to coincide with the development of neutron diffraction peaks in the scattering vector range of 1.8-2.0 $Å^{-1}$, as well as a 2 kJ mol^{-1} increase in the heat of adsorption leading them to also conclude that the adsorption isotherm step was the result of argon crystallization in the zeolite pores.[120] Development of the step in the Ar adsorption isotherm has also been correlated with a decrease in H-ZSM-5 aluminum content as measured by chemical analysis.[120–123] Although the heat of argon adsorption has been measured by calorimetry to be constant at 14 kJ mol^{-1} for loadings below 95 $cm^3\,g^{-1}$ for all H-ZSM-5 samples, Llewellyn *et al.* proposed that aluminum induces a moment in argon causing it to preferentially adsorb at aluminum atoms and therefore a disappearance of the isotherm step.[120,122]

Pellenq and Nicholson found that they could not reproduce the silicalite-1 structure

neutron diffraction peaks (1.6 and 1.8 $Å^{-1}$) reported by Llewellyn *et al.* for Ar 77 K adsorption using their grand canonical Monte Carlo (GCMC) simulations without allowing zeolite framework relaxation.[127] Thus, the authors concluded that the Ar 77 K isotherm step is the result of changes in the adsorbent structure, which may induce restructuring of the adsorbate. García-Pérez also arrived at this conclusion through GCMC simulations of their experimental Ar adsorption results on silicalite-1 at 77 K with rigid orthorhombic, rigid monoclinic, and flexible zeolite structures.[128] They found that a flexible zeolite framework reproduces the argon loadings within ∼30% for the whole range of pressures, which suggests that framework changes are responsible for the step in the adsorption isotherm.

Although we did not perform XRD measurements of Ar-loaded silicalite, we also surmise that the step is the result of a reversible monoclinic-orthorhombic transformation based on the symmetry features inferred by the XRD patterns collected after calcination, and this hypothesis is further supported by the Q^4 peaks in the ^{29}Si MAS NMR spectra (see Figure 5.3). Engelhardt and van Koningsveld used a quantitative correlation between tetrahedral bond angles and chemical shift to simulate the ^{29}Si MAS NMR patterns for orthorhombic and monoclinic silicalite-1.[129] They showed that upon transformation from an orthorhombic to monoclinic symmetry, not only does the number of possible resonances increase from 9 to 20, but all lines shift downfield due to the larger bond angles and decrease in chemical shielding. They also identified a peak at approximately -110 ppm that is indicative of the monoclinic symmetry. This peak is not observed in the defective Si[OH] -110 ppm peak begins to evolve in the S1 sample, which is likely to contain both orthorhombic and monoclinic phases, and then is clearly resolved for both the S2 and Si[F] materials which we conclude are monoclinic.

It has been noted by several authors that orthorhombic alkaline-synthesized silicalite-1 can undergo a reversible phase change to the monoclinic symmetry with a decrease in temperature, and the temperature of this transition has been shown to range from 303-333 K with the synthesis method.[115,116] Therefore, XRD and ^{29}Si MAS NMR observations at 87 K, confirming that the silicalite-1 materials still exhibit different predominant phases at this temperatur,e would provide additional evidence for the relationship between symmetry and the Ar 87 K hysteresis.

5.3.2 Effect of Defects on Vapor Propylene Glycol Adsorption

It can be seen in Figure 5.5 that propylene glycol adsorption in the vapor phase is promoted across all pressure ranges up to saturation by the presence of silanol defects. A maximum increase in adsorption by a factor of 6 is found at 10^{-3} kPa from the defect-free fluoride synthesized silicalite-1 (∼0.005 g adsorbed/g zeolite) to the defective S1 silicalite-1 (∼0.03 g adsorbed/g zeolite). The isotherms saturate between 0.13 g propylene glycol per g zeolite

(9.9 molecules per unit cell) to 0.15 g per g zeolite (11.4 molecules per unit cell) which are in agreement with the values of 11.5 and 9.9 molecules per unit cell reported by Xiong *et al.*[4] and Long *et al.*[43] using GCMC and gravimetric experiments, respectively.

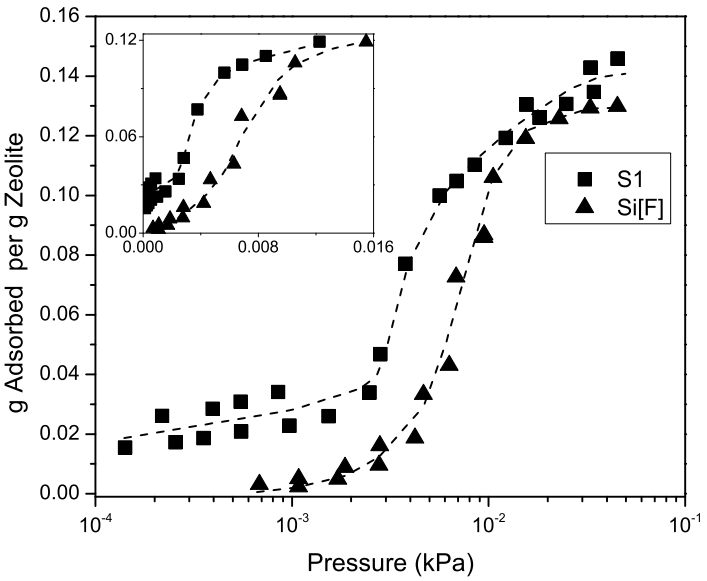

Figure 5.5: Vapor propylene glycol adsorption on S1 and Si[F] at 333 K (logarithmic pressure scale). Inset: Data plotted on a linear pressure scale. Dashed lines are a guide to the eye.

Vapor propylene glycol adsorption on defect-free silicalite-1 exhibits a Type V isotherm (inset Figure 5.5). The primary features of a Type V isotherm are 1) a convex isotherm curve relative to the pressure axis, and 2) a saturation plateau at high pressures. These isotherms are most commonly reported for water adsorption on hydrophobic carbons and are indicative of weak adsorbate-adsorbent interactions and favorable adsorbate-adsorbate interactions or clustering of adsorbate molecules.[130] By taking the first derivative of the adsorption isotherm with respect to the adsorbate pressure, it is identified that the inflection in the isotherm correlates with a pressure of $\sim 6\times 10^{-3}$ kPa and an uptake of 3-5 propylene glycol molecules per unit cell.

It is likely that propylene glycol is forming clusters; similar observations have been made regarding the modes of water and alcohol adsorption on zeolites. Examples of Type V isotherms on zeolites include adsorption of methanol on dealuminated zeolite Y,[131] water adsorption/intrusion on hydrophobic defect-free silicalite-1,[17,29,132] and water adsorption on all-silica DD3R.[133] Plotting of the vapor propylene glycol adsorption data obtained by Xiong *et al.* on silicalite-1 on a linear pressure axis reveals that their simulations also result

in a Type V isotherm[4] (see Figure 5.15). Using the same computational approach, these authors also noted that alcohol molecules cluster in defect-free silicalite-1,[5] therefore it is plausible that hydrogen bonding of propylene glycol with other propylene glycol molecules could occur within Si[F], and result in a Type V isotherm.

5.3.3 Comparison of Vapor and Aqueous Propylene Glycol Adsorption

Aqueous propylene glycol adsorption increases across all concentrations, up to saturation, in the order Si[F]< S1< Si[OH], demonstrating that silanol defects also promote adsorption in the presence of water (Figure 5.6; see Section 5.5.3 for calculations of the amount adsorbed in aqueous solutions). The amount adsorbed increases by a maximum factor of 20 from Si[F] to Si[OH] at concentrations less than 10^{-3} g/mL. The effect of silanol density on adsorption becomes less pronounced as the pressure increases - adsorption is increased by a factor of 3.5 between Si[F] and Si[OH] in the moderate concentration range (10^{-2} g/mL) and the coverages at concentrations greater than 10^{-1} g/mL differ by less than 0.02 g adsorbed per g zeolite.

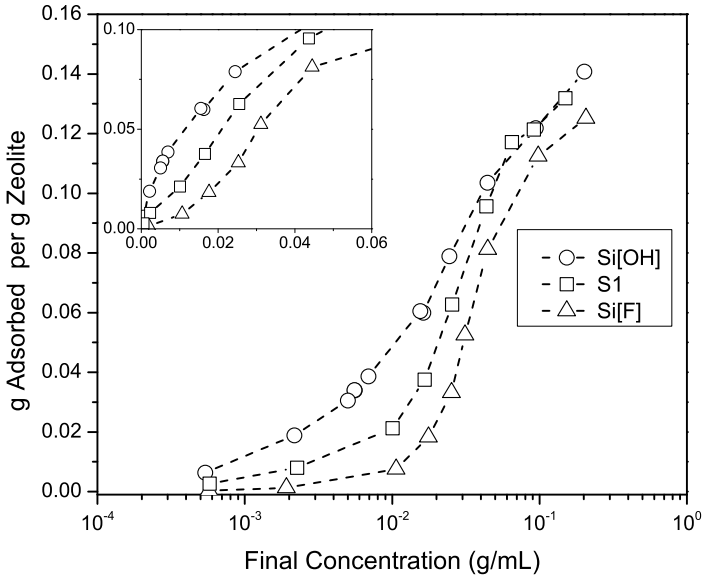

Figure 5.6: Aqueous propylene glycol adsorption isotherms on Si[OH], S1, and Si[F] 333 K (logarithmic concentration scale). Inset: Data plotted on a linear concentration scale. Dashed lines are a guide to the eye.

Plotting of the aqueous propylene glycol adsorption isotherms on a linear concentration scale (see inset of Figure 5.6) reveals that the isotherm shape changes with the number

of silanol defects. The most defective material, Si[OH], exhibits a Type I isotherm which indicates that adsorption sites available to propylene glycol are energetically equivalent across all concentrations shown. It is known from ^{29}Si MAS NMR that there are ∼8.5 Si-OH per unit cell (see Table 5.1) and the Type I isotherm behavior is exhibited through a loading of 0.1 g propylene glycol per g zeolite or 7.6 molecules per unit cell. Since there is less than one molecule adsorbed per Si-OH, it is reasonable that all sites are energetically equivalent and that a Langmuir adsorption isotherm is observed for this system. As with vapor propylene glycol adsorption, aqueous propylene glycol adsorption on Si[F] is of the Type V character indicating weak adsorbate-zeolite and the onset of strong adsorbate-adsorbate interactions as represented by the isotherm inflection at a loading of 2-4 propylene glycol molecules per unit cell.

The aqueous solution data were converted into units of pressure by assuming ideal vapor/non-ideal solution equilibrium (see Section 5.5.4) and these data are compared with vapor adsorption isotherms in terms of both concentration and pressure in Figures 5.7 and 5.8. A comparison of the aqueous and vapor propylene glycol adsorption isotherms in Figure 5.7 demonstrates that propylene glycol adsorption on defect-free Si[F] is promoted by the presence of water at pressures up to saturation, with a maximum increase in adsorption by a factor of 4 at approximately 3×10^{-3} kPa. Note that this difference is found regardless of the method for converting aqueous concentration to partial pressure as described in Section 5.5.4.

Adsorption enhancement in the presence of water has been noted in the simulation of methanol and ethanol adsorption on all-silica DDR,[84,133] FAU,[84] and MFI,[5] and was recently predicted by Xiong *et al.* for polyol adsorption on defect-free silicalite-1.[4] Xiong *et al.* found that K_{ads} increases by a factor of 2.3 from 740 to 1700 mol kg^{-1} kPa^{-1} for propylene glycol adsorption on perfect silicalite-1 at 298 K upon introduction of water (note that this comparison required unit conversions which are outlined in Section 5.5.4). Here, we find K_{ads} values of 62 and 140 mol kg^{-1} kPa^{-1} for vapor and aqueous propylene glycol adsorption at 333 K, respectively, which also represents a 2.3-fold increase in adsorption due to incorporation of water in the system.

Xiong *et al.* found clustering between water and polyol molecules to be responsible for promotion of polyol adsorption on defect-free zeolites.[4,5] The authors showed that pure methanol and ethanol adsorption at a fugacity of 1 Pa occurs only in the zig-zag channels of defect-free silicalite-1. When water is introduced to the system, it hydrogen bonds with the alcohol inside the zeolite pores resulting in an increase in the cluster size at the original adsorption sites as well as the development of new water-alcohol clusters in the straight channels.[5] The importance of alcohol-water interactions on adsorption was also highlighted by a CBMC study by Krishna *et al.* who identified that the number of hydrogen bonds

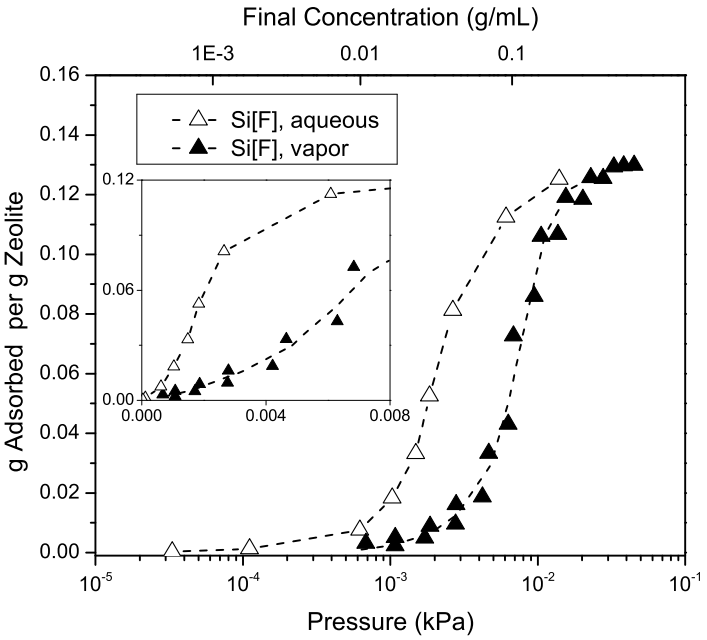

Figure 5.7: Aqueous and vapor adsorption isotherms for propylene glycol on Si[F] 333 K (logarithmic pressure scale). Inset: Data plotted on a linear pressure scale. Dashed lines are a guide to the eye.

formed in a system of methanol, water, and defect-free silicalite-1 is highest for methanol-water pairings followed by methanol-methanol and then water-water interactions.[84] On the basis of our results and the findings of these computational studies, we propose that the increase in propylene glycol adsorption in the presence of water is due to an increase in the number of adsorption sites due to hydrogen bonding with water within the zeolite framework.

As opposed to the findings on Si[F], it can be observed in Figure 5.8 that water suppresses propylene glycol adsorption by a factor of 2 at pressures below 10^{-3} kPa on the defective material, S1. Since the effect of water on propylene glycol adsorption is material dependent, this change in adsorption affinity must be attributed to interactions between water and propylene glycol within the zeolite. Lee *et al.* determined by gravimetry and calorimetry that methanol adsorbs with an enthalpy up to 60 kJ mol^{-1} more than water on silicalite-1,[23] so it can be extrapolated that propylene glycol adsorption has a greater adsorption affinity over water adsorption on S1. However, it is possible at low concentrations of propylene glycol, where water accounts for more than 99.9% percent of the molecules in the system, that competition of water with propylene glycol for adsorption on the silanol defect sites cannot be neglected. Molecular simulations could probe the effect of water on propylene

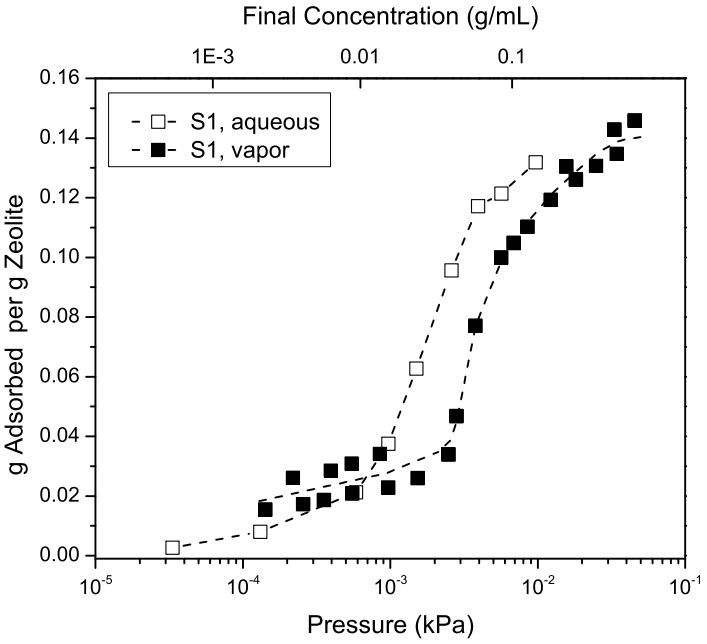

Figure 5.8: Aqueous and vapor adsorption isotherms for propylene glycol on S1 at 333 K (logarithmic pressure scale). Top axis relates aqueous solution concentration to the pressure reported. Dashed lines are a guide to the eye.

glycol adsorption on defective silicalite-1 materials.

5.3.4 Correlating K_{ads} for Polyol Adsorption from Aqueous Solutions with Silanol Defect Concentration

A comparison of the aqueous adsorption isotherms for propylene glycol (C_3), ethylene glycol (C_2), and 1,2-butanediol (C_4) at 298 K on the four different silicalite-1 materials indicates that defects promote adsorption for all these polyol adsorbates (see Figures 5.9-5.11). Adsorption of these molecules at dilute concentrations (less than 4×10^{-3} g/mL) increases in the order Si[F]< S2< S1< Si[OH], which corresponds with an increase in the silanol defect density.

Since adsorption is linearly dependent on the adsorbate concentration, we can extract the Henry's constants from the isotherm slopes, and these are reported in Figures 5.9-5.12. A 24-31 fold increase is observed when comparing the K_{ads} values for Si[F] and Si[OH] for a single adsorbate. We find a K_{ads} value of 0.57 mL solution/g silicalite which is within 10% of the value reported by Xiong *et al.* (0.6 mL solution/g silicalite).[4]

We reported in Chapters 2 and 3 that Henry's constants for these molecules on MFI materials increase exponentially with carbon number, and, for all Si/Al ratios, we identified

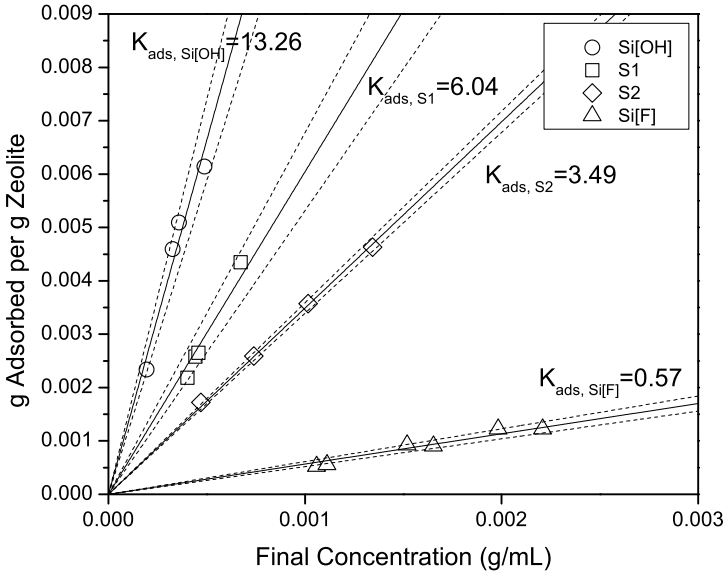

Figure 5.9: Aqueous propylene glycol adsorption solutions on Si[OH], S1, S2, and Si[F] at 298 K. Solid lines represent least-squares linear regressions and dashed lines represent 95% confidence intervals. K_{ads} values are reported in mL solution/g zeolite.

that K_{ads} for propylene glycol is approximately one order of magnitude greater than K_{ads} for ethylene glycol. The simulations of Xiong *et al.* also showed an exponential relationship between K_{ads} and carbon number for diols and triols with more than three carbon atoms.[4] However, these simulations predicted that ethylene glycol adsorption was greater than propylene glycol. The authors proposed a number of hypotheses for the discrepancy in the propylene glycol/ethylene glycol selectivity between our previous experimental study and their predictions. One of these proposals was that our experiments were performed with materials that contain defects which alter the propylene glycol/ethylene glycol selectivity, while their simulations were performed using a defect-free framework. Indeed, the effect of defects on K_{ads} very pronounced, but as shown in Figure 5.12, the affinity of adsorption for propylene glycol is greater than that for ethylene glycol on all materials tested. This trend includes the defect-free Si[F] material, which has a ratio of K_{ads} for propylene glycol over ethylene glycol of $\sim$10, suggesting that this discrepancy remains unresolved.

We also found in Chapter 2 that K_{ads} for aqueous propylene glycol adsorption on the MWW, MFI, BEA, MOR, and FAU frameworks decreased up to 50% with a decrease in the zeolite Si/Al from infinity to 10 at 298 K. One hypothesis we presented was that propylene glycol adsorption increases with a decrease in the number of hydrophilic Brønsted acid due to

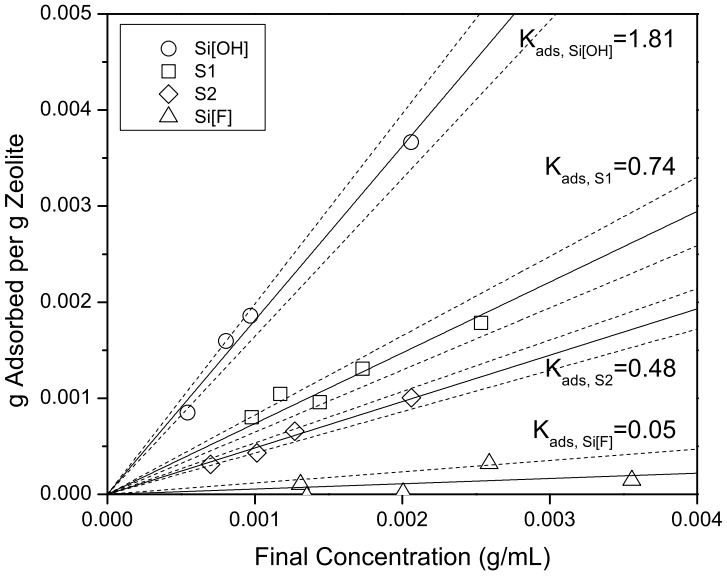

Figure 5.10: Aqueous ethylene glycol adsorption on Si[OH], S1, S2, and Si[F] at 298 K. Solid lines represent least-squares linear regressions and dashed lines represent 95% confidence intervals. K_{ads} values are reported in mL solution/g zeolite.

a decrease in the competitive adsorption of water. By studying polyol adsorption on a series of siliceous MFI materials, we have identified that interactions between the adsorbate and silanol groups can increase K_{ads} over an order of magnitude. We now propose, on the basis of the work presented here, that the previously observed increase in K_{ads} with Si/Al cannot be exclusively attributed to decreasing Brønsted acid site density since both Brønsted acid sites and silanol defects are likely to exist on the zeolite surface and interact with polyol adsorbates. Therefore, both Brønsted acid sites as well as silanol defect sites need to be counted in order in order to quantify the effect of Brønsted acid sites on adsorption of polyols.

The most striking trend presented in Figure 5.12 is that K_{ads} in aqueous solutions increases linearly with the number of silanol defects per unit cell for ethylene glycol, propylene glycol, and 1,2-butanediol for all silicalite-1 materials at 298 K. That is, K_{ads} for a particular adsorbate-silicalite-1 system scales with the number of silanols per unit cell by

$$K_{ads} = K_{ads,Si[F]} + c \times \rho_{Si-OH}, \tag{5.1}$$

where K_{ads} is the Henry's constant for the system, $K_{\text{ads,Si[F]}}$ is the Henry's constant for the adsorbate of interest on Si[F], c is a constant, and $\rho_{\text{Si}-\text{OH}}$ is the number of silanols per

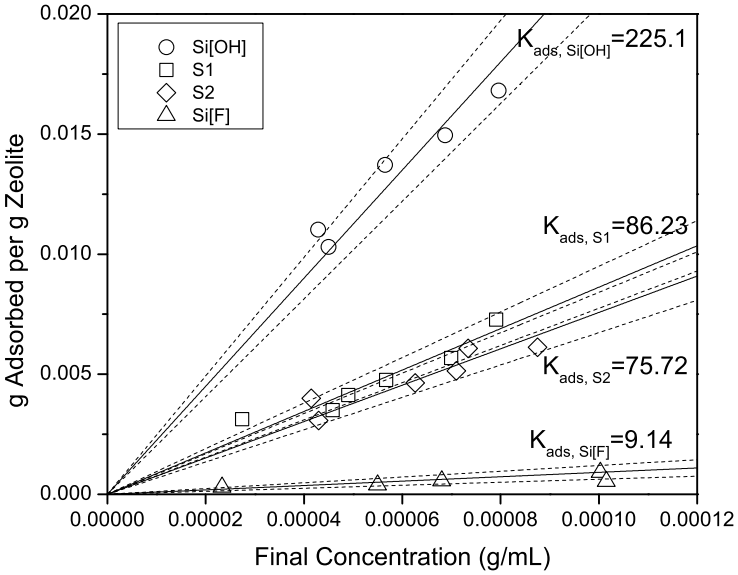

Figure 5.11: Aqueous 1,2-Butanediol adsorption on Si[OH], S1, S2, and Si[F] at 298 K. Solid lines represent least-squares linear regressions and dashed lines represent 95% confidence intervals. K_{ads} values are reported in mL solution/g zeolite.

unit cell. Since K_{ads} is proportional to the number of molecules adsorbed, this analysis indicates that the linear increase in K_{ads} with silanol defect number in Figure 5.12 results from interactions between adsorbate molecules and silanol defects.

5.4 Conclusions

Defective silicalite-1 crystals were synthesized using an alkaline solution method and defects were subsequently healed using steaming treatments to obtain crystals with defect densities ranging from ∼8.5 to 2.9 silanols per unit cell as measured with ^{29}Si MAS NMR. A fluoride-based synthesis method was used to obtain defect-free silicalite-1.

The hysteresis at 10^{-3} reduced pressure in the Ar adsorption measured at 87 K, which has only been linked with a low Brønsted acid site number in aluminosilicate materials, was resolved through the reduction of silanol defects. It was proposed on the basis of XRD and ^{29}Si MAS NMR analyses that this step may be the result of a monoclinic-orthorhombic transition for those materials that have less than 2.9 Si-OH defects per unit cell.

Silanol defects were shown to promote vapor and aqueous solution adsorption of propylene glycol up to a factor of 20 from Si[F] to Si[OH] at 333 K. A change in the aqueous

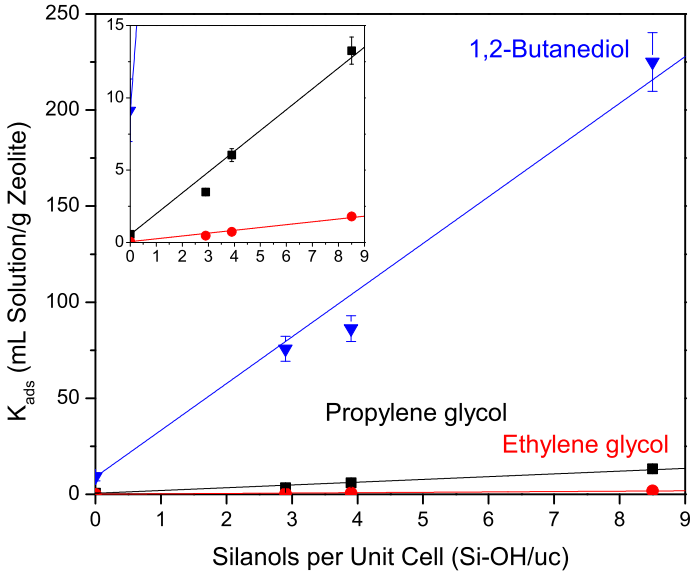

Figure 5.12: K_{ads} versus Si-OH/uc for aqueous 1,2-butanediol, propylene glycol, and ethylene glycol adsorption on Si[OH], S1, S2, and Si[F] at 298 K. Error bars represent 95% confidence intervals. Inset: Magnified view of K_{ads} values below 15 mL Solution/g Zeolite.

solution isotherm shape from Type I for a material with 8.5 silanols per unit cell to Type V for the defect-free material was also detected. A Type V isotherm was also identified for vapor propylene glycol adsorption on the defect-free material, although water was found to promote adsorption by a factor of 2 in the low pressure regime (less than 10^{-4} kPa).

An enhancement in adsorption by a factor of ∼20-30 in the Henry's Law regime was found for propylene glycol, 1,2-butanediol, and ethylene glycol adsorption from aqueous solutions at 298 K. It was also identified that K_{ads} is linearly dependent on silanol defect density for these systems, which provides evidence that these molecules preferentially interact with defects in the Henry's Law adsorption regime.

5.5 Supporting Information

5.5.1 ^{1}H-^{29}Si CPMAS and ^{1}H MAS NMR Data for the Silicalite-1 Materials

MAS NMR spectra of the solids (^{1}H MAS NMR and ^{1}H-^{29}Si CPMAS NMR) were recorded on a Bruker DSX-500 spectrometer equipped with a Bruker 4 mm MAS NMR probe. The ^{1}H-^{29}Si CPMAS NMR and ^{1}H MAS spectra were recorded with a spinning rate of 8 kHz

and 14 kHz, respectively, and at a ^{29}Si frequency of 99.5 MHz and 1H frequency of 500.2 MHz. The pulse length was of 2.0 ms for the CPMAS spectra and of 4.0 ms for the ^{1}H MAS spectra. The recycle delay was 4 s.

The ^{1}H-^{29}Si CPMAS NMR spectrum for Si[OH] contains two peaks at -102 and -113 ppm, as shown in Figure 5.13, indicating that silanols are present in the sample[29]. These features would also be expected for the S1 and S2 samples on the basis of the ^{29}Si MAS NMR, but they cannot be clearly distinguished in the spectra possibly due to the large signal noise.

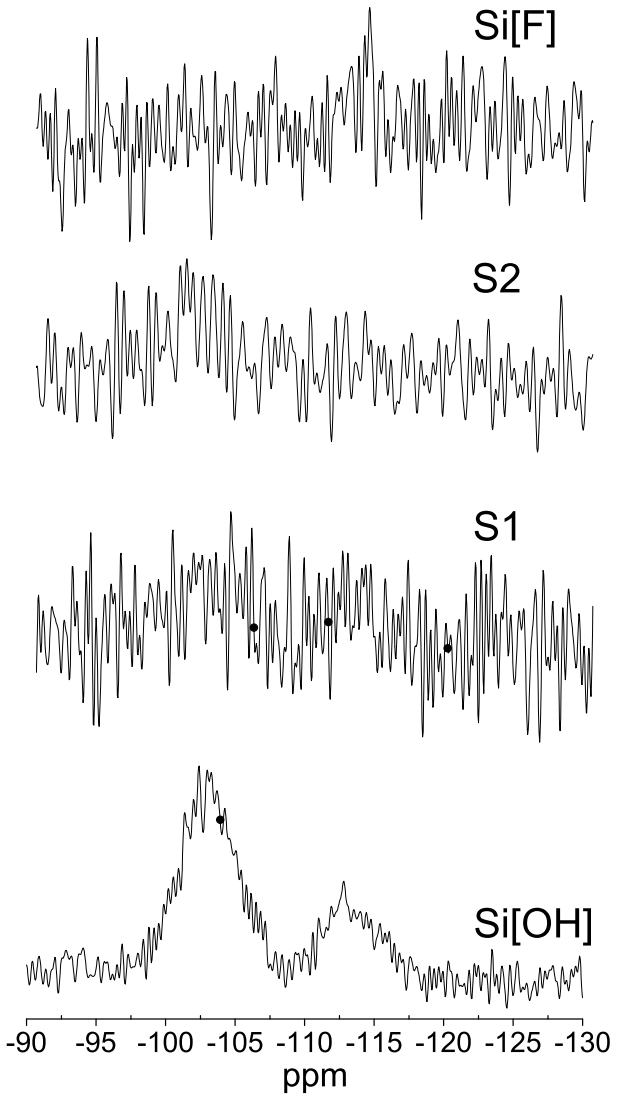

Figure 5.13: ^{1}H-^{29}Si CPMAS NMR of the Si[OH], S1, S2, and Si[F] silicalite-1 materials.

The ^{1}H MAS NMR spectra for the Si[OH] and S1 samples both contain a peak at ∼1.3 ppm ,which has been ascribed to silanol defects[119]. The intense broad line present at chemical shifts greater than 3 ppm for the Si[OH], S1, and S2 samples is due to adsorbed water on the surface[119]. Since water only adsorbs at silanol defects at atmospheric pressure[29], the decreasing line width in the order Si[OH]>S1>S2 is also indicative of a decrease in silanol defects.

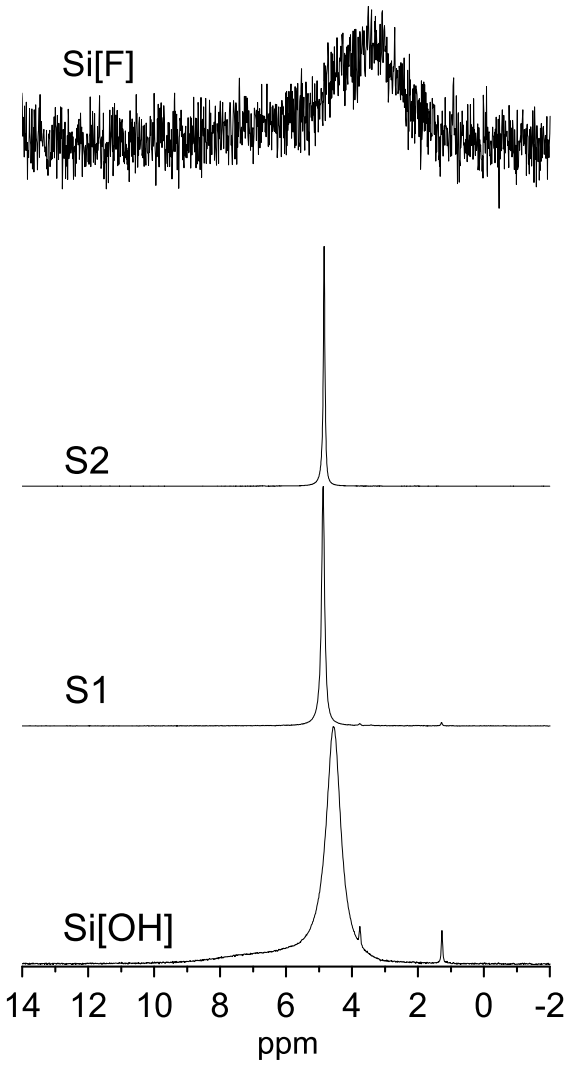

Figure 5.14: ^{1}H MAS NMR of the Si[OH], S1, S2, and Si[F] silicalite-1 materials.

5.5.2 Comparison of Vapor Propylene Glycol Adsorption on Si[F] with Simulations

Xiong *et al.* used grand canonical Monte Carlo to obtain vapor propylene glycol adsorption data on defect-free silicalite-1 at 298 K.[4] To compare our results at 333 K with their data, the pressure axes need to be normalized to the propylene glycol saturation pressures at their respective temperatures. That is, the propylene glycol pressure values reported by Xiong *et al.* are normalized to the vapor pressure at 298 K, 17.3 Pa, and our data is normalized to the vapor pressure at 333 K, 280 Pa. Note that the vapor pressures were obtained from interpolation of the vapor pressure data reported by Curme and Johnston.[114] The normalized data is plotted in Figure 5.15, and it can be observed that we have good agreement with the results of Xiong *et al.* at P/P_s below 3×10^{-3} and at saturation. However, they report an uptake which is a factor of 6 higher than what we find in the moderate pressure range (P/Ps =0.01).

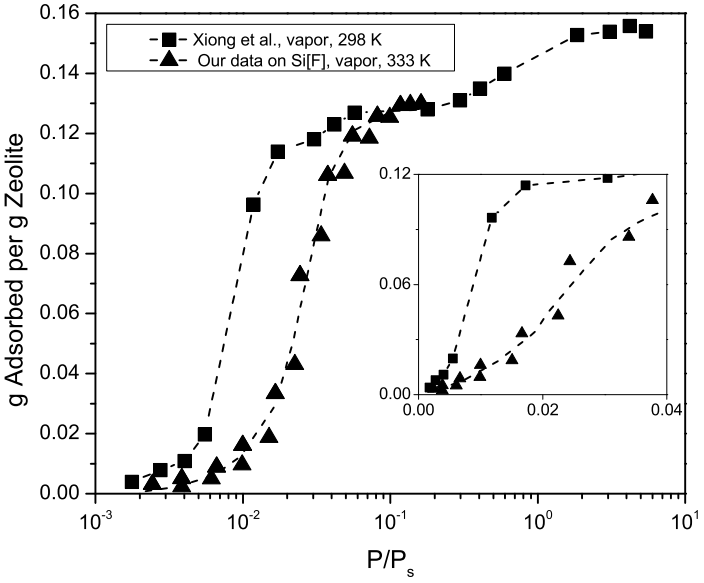

Figure 5.15: Vapor propylene glycol adsorption on Si[F] at 333 K and computational adsorption data from Xiong *et al.* for vapor propylene glycol on defect-free silicalite-1 at 298 K[4]. Inset: Data on a linear pressure scale. Dashed lines are a guide to the eye.

5.5.3 Effect of Solution Volume Change on Aqueous Solution Adsorption Measurements

The amount of propylene glycol adsorbed on the zeolite is not directly measured in the aqueous phase adsorption experiments. Rather, the final concentration of the solution is determined via high performance liquid chromatography and the amount adsorbed, a, can be calculated from the difference in the initial and final concentrations by

$$a = \frac{(C_I - C_F)\,V}{m_z}, \tag{5.2}$$

where C_{I} is the initial solution concentration, C_{F} is the final solution concentration, V is the solution volume, and m_{z} is the zeolite mass. Note that assumptions in this calculation are 1) the volume of the solution does not change with propylene glycol adsorption, 2) water adsorption is neglected, and 3) there is no volume change due to non-ideal mixing. If solution volume changes are accounted for in this calculation, the equation becomes

$$a = \frac{C_I V_I - C_F V_F}{m_z}, \tag{5.3}$$

where V_{F} is the final volume in mL. Calculation of C_{I}, V_{I}, and V_{F}, when accounting for volume changes, are described below.

Every solution is created by taking an aliquot of a stock solution and diluting it with water. The stock solution is created by weighing out propylene glycol and water. Therefore, the moles and mole fractions of each component ($x_{\mathrm{PG,stock}}$ and $x_{\mathrm{H2O,stock}}$ for propylene glycol and water, respectively) are known. Romero *et al.* reported molar volumes ($\mathrm{cm^3\ mol^{-1}}$) of solutions ranging from 0-0.2 mole fraction of propylene glycol in water at 298 K.[134] These data were fit with a least-squares linear regression resulting in

$$V_m = 52.535\,cm^3mol^{-1} \times x_{PG} + 18.07\ cm^3mol^{-1}, \tag{5.4}$$

where V_{m} is the solution molar volume and x_{PG} is the propylene glycol mole fraction, which allows for calculation of the stock solution molar volume, $V_{\mathrm{m,stock}}$.

To create a solution for an adsorption measurement, a known volume of the stock solution, V_{stock}, is diluted with a known volume of water, V_{water}. The moles of propylene glycol, $n_{\mathrm{PG,initial}}$, and water, $n_{\mathrm{H2O,initial}}$, in the initial solution are then calculated by

$$n_{PG,initial} = \left(\frac{V_{stock}}{V_{m,stock}}\right) x_{PG,stock}, \tag{5.5}$$

and

$$n_{H2O,initial} = \left(\frac{V_{stock}}{V_{m,stock}}\right) x_{H2O,stock} + \frac{V_{water} \times \rho_{H2O}}{MW_{H20}}, \tag{5.6}$$

where ρ_{H2O} is the density of pure water at 298 K and MW_{H20} is the molecular weight of water.

The mole fraction of propylene glycol in the initial solution is then calculated, and the molar volume of the initial solution, $V_{\mathrm{m,I}}$, is identified from Equation 5.4 This is then used to calculate the volume of the initial solution, V_{I}, by

$$V_I = V_{m,I}\left(n_{PG,initial} + n_{H2O,initial}\right). \tag{5.7}$$

The initial volumes calculated in this method varied less than 2% from the ideal solution volumes, resulting in a change in the initial concentrations calculated of less than 4%.

In order to calculate the final volume for a non-ideal solution, the following approach is used. The final concentration, C_{F}, is obtained from high performance liquid chromatography. The number of moles of propylene glycol in the final solution, $n_{\mathrm{PG,final}}$, is defined as

$$n_{PG,final} = \frac{C_F \times V_F}{MW_{PG}}, \tag{5.8}$$

where MW_{PG} is the molecular weight of propylene glycol, and V_{F} is the final solution volume, which is defined as

$$V_F = V_{m,F}\left(n_{PG,final} + n_{H2O,final}\right). \tag{5.9}$$

Combining Equations 5.8 and 5.9 one obtains

$$C_F = \frac{x_{PG,final} \times MW_{PG}}{V_{m,F}}. \tag{5.10}$$

By inserting Equation 5.4 into Equation 5.10, the value of $x_{\mathrm{PG,final}}$ is calculated. $V_{\mathrm{m,F}}$ is then determined from $x_{\mathrm{PG,final}}$ and Equation 5.4. By assuming that water is not adsorbed, that is $n_{\mathrm{H2O,final}} = n_{\mathrm{H2O,initial}}$, the final number of moles of propylene glycol can be calculated since $x_{\mathrm{PG,final}} = n_{\mathrm{PG,final}}/(n_{\mathrm{PG,final}} + n_{\mathrm{H2O,final}})$. V_{F} is then calculated from Equation 5.9, which is used to calculate the amount adsorbed, a, from Equation 5.3.

In order to calculate the amount adsorbed when accounting for volume changes due to propylene glycol and water adsorption, the following method is used. An extreme approach is to assume that water fills any pore volume not occupied by propylene glycol, or

$$n_{H2O,ads} = \frac{\left(1 - \frac{a}{a_{max}}\right) \times w_{max} \times \rho_z \times m_z}{N_A}, \tag{5.11}$$

where $n_{\mathrm{H2O,ads}}$ is the number of moles of water adsorbed, $a_{\max}$ is the maximum amount of propylene glycol adsorbed (taken as 0.12984 g PG/g zeolite for Si[F] and 0.14582 g PG/g zeolite for Si[OH] and S1, from vapor adsorption saturation values), $w_{\max}$ is the maximum amount of water adsorbed (taken as 41 molecules per unit cell, as reported by Trzpit *et al.*[29]), ρ_{z} is the number of unit cells per g of silicalite-1 (1.04×10^{20} uc/g), and N_{A} is Avogadro's number (6.022×10^{23} molecules/mol). Note that this assumption results in a gross overestimation of the amount of water adsorbed at low polyol loadings since liquid water at atmospheric pressure has been shown to adsorb less than 5 molecules per unit cell.[29]. Also, the number of unit cells per gram silicalite-1, ρ_{z}, was calculated using

$$\rho_z = \frac{96\ T\ atoms}{uc} \times \frac{1\ SiO_2\ molecule}{T\ atom} \times \frac{mol}{6.022 \times 10^{23}\ molecules} \times \frac{g}{60.09\ mol} = 1.04 \times 10^{20} uc/g. \tag{5.12}$$

The final number of moles in the solution, $n_{\mathrm{H2O,final}}$, can then be calculated from

$$n_{H2O,final} = n_{H2O,initial} - n_{H2O,ads}. \tag{5.13}$$

A new final mole fraction of propylene glycol is calculated from the final moles of propylene glycol and water, and this is used to determine a new final solution molar volume with Equation 5.4. A new final volume (Equation 5.9) and, therefore, new amount adsorbed (Equation 5.3) is calculated.

Using these methods to calculate the final solution volume results in larger values for the amount adsorbed for aqueous adsorption isotherms. As shown in Figures S4-S6, a maximum increase of ∼40% is found for saturation conditions where up to 240 mg of zeolite was used in the measurements (as compared with only 20 mg required for accurate measurements at low concentrations)..

Using these methods to calculate the final solution volume results in larger values for the amount adsorbed for aqueous adsorption isotherms. As shown in Figures 5.16-5.18, a maximum increase of ∼40% is found for saturation conditions where up to 240 mg of zeolite was used in the measurements (as compared with only 20 mg required for accurate measurements at low concentrations).

As for the Henry's Law regime (see Figures 5.19-5.21 and Tables 5.2-5.4, the K_{ads} values change to varying extents depending on the system, and this is the result of different zeolite amounts used for the measurements and the amounts adsorbed. Since it is most accurate to account for volume changes due to polyol adsorption, *volume changes associated with polyol adsorption were considered in the reporting of aqueous adsorption data.* However, water adsorption was neglected since it cannot be quantified in our measurements, and is likely to

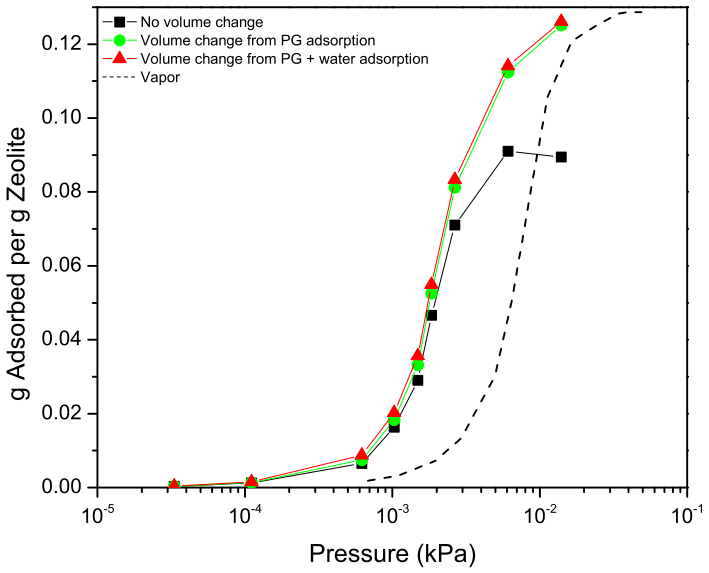

Figure 5.16: Aqueous propylene glycol adsorption on Si[F] at 333 K.

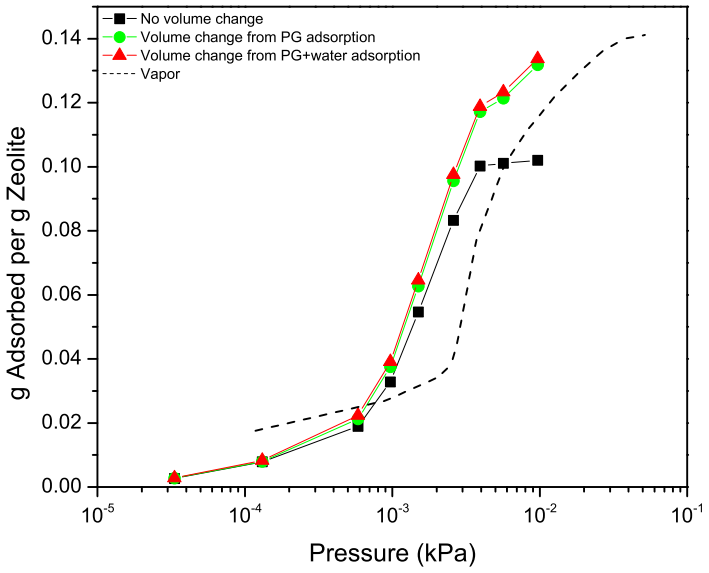

Figure 5.17: Aqueous propylene glycol adsorption on S1 at 333 K.

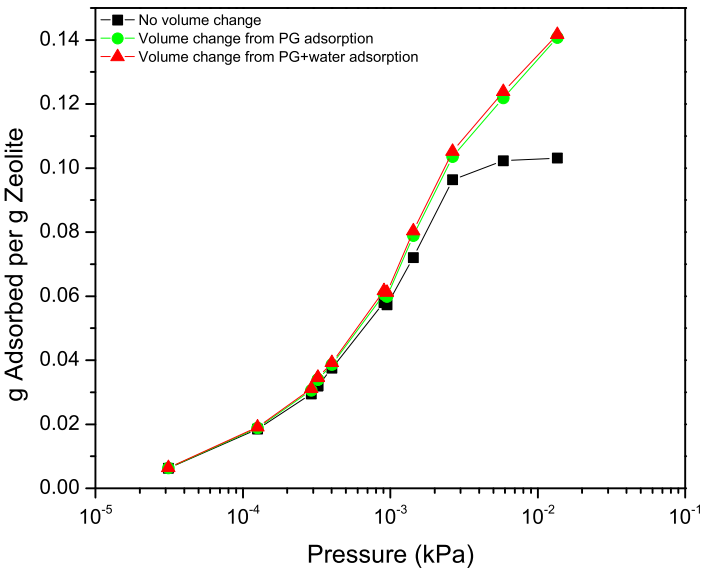

Figure 5.18: Aqueous propylene glycol adsorption on Si[OH] at 333 K.

amount to only a few molecules per unit cell at the experimental conditions. Note that the volume changes for aqueous 1,2-butanediol and ethylene glycol adsorption were calculated in the same fashion as propylene glycol, with the exception that Equation 5.4 is replaced by

$$V_m = 52.535\, cm^3 mol^{-1} \times x_{BD} + 18.07 cm^3 mol^{-1}, \tag{5.14}$$

for 1,2-butanediol (where x_{BD} is the mole fraction of 1,2-butanediol), which results from a linear regression on the solution molar volume data published by Romero *et al.*[135]. Similarly, Equation 5.4 is replaced by

$$V_m = 52.535\, cm^3 mol^{-1} \times x_{EG} + 18.07 cm^3 mol^{-1}, \tag{5.15}$$

for ethylene glycol (where x_{EG} is the mole fraction of ethylene glycol), which results from a linear regression on the solution density data published by Ambrosone *et al.*[136].

5.5.4 Calculation of Partial Pressures from Aqueous Solution Concentrations

In order to calculate partial pressures from aqueous solution concentrations, one can use Raoult's law,

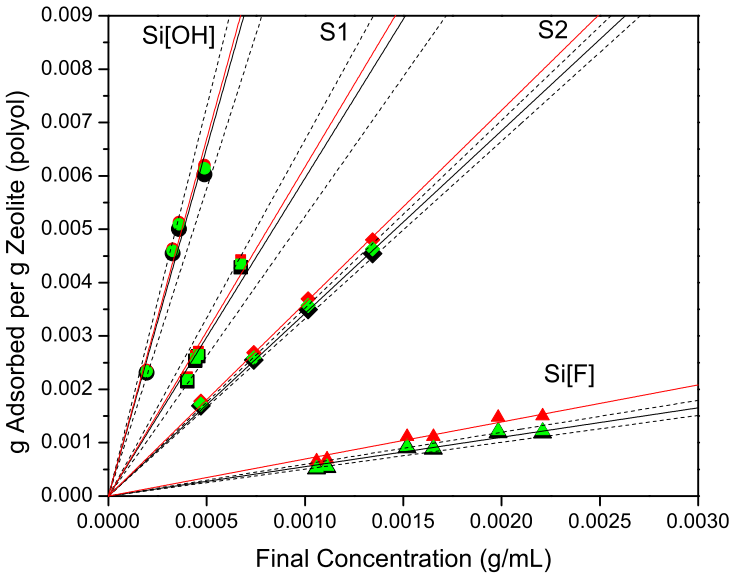

Figure 5.19: Aqueous propylene glycol adsorption on silicalite-1 at 298 K. Black points/lines are for the assumption that there is no volume change, green are for a volume change with propylene glycol adsorption, and red are for a volume change with propylene glycol adsorption and filling of the remaining pore volume with water.

Table 5.2: Comparison of propylene glycol K_{ads} values calculated with and without a solution volume change.

	No Correction	Correction for volume change due to polyol adsorption	Correction for volume change due to polyol adsorption assuming that remaining pore volume is filled with water
$K_{ads,Si[OH]}$ (mL solution/g zeolite) (0.01 to 0.04 g zeolite per 0.4 mL solution)	13.05	13.26 (2% increase)	13.39 (3% increase)
$K_{ads,S1}$ (mL solution/g zeolite) (0.03 to 0.06 g zeolite per 0.4 mL solution)	5.95	6.04 (2% increase)	6.17 (4% increase)
$K_{ads,S2}$ (mL solution/g zeolite) (0.03 to 0.04 g zeolite per 0.4 mL solution)	3.42	3.49 (2% increase)	3.61 (6% increase)
$K_{ads,Si[F]}$ (mL solution/g zeolite) (0.12-0.18 g zeolite per 0.4 mL solution)	0.55	0.57 (4% increase)	0.69 (25% increase)

Table 5.3: Comparison of 1,2-butanediol K_{ads} values calculated with and without a solution volume change.

	No Correction	Correction for volume change due to polyol adsorption
$K_{ads,Si[OH]}$ (mL solution/g zeolite) (0.02 g zeolite per 0.4 mL solution)	223.2	225.1 (1% increase)
$K_{ads,S1}$ (mL solution/g zeolite) (0.02 g zeolite per 0.4 mL solution)	85.51	86.23 (1% increase)
$K_{ads,S2}$ (mL solution/g zeolite) (0.02 g zeolite per 0.4 mL solution)	75.09	75.72 (1% increase)
$K_{ads,Si[F]}$ (mL solution/g zeolite) (0.02 g zeolite per 0.4 mL solution)	9.00	9.14 (2% increase)

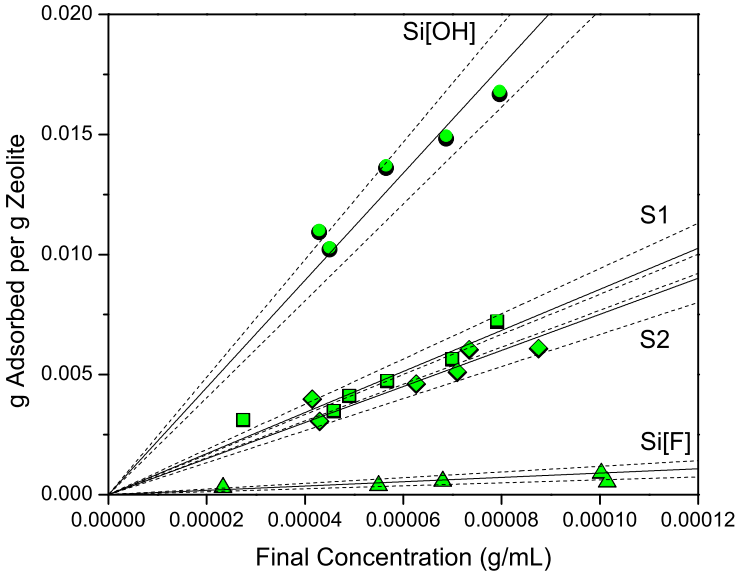

Figure 5.20: Aqueous 1,2-butanediol adsorption on silicalite-1 at 298 K. Black points/lines are for the assumption that there is no volume change, and green points are for a volume change with polyol adsorption.

Table 5.4: Comparison of ethylene glycol K_{ads} values calculated with and without a solution volume change.

	No Correction	Correction for volume change due to polyol adsorption
$K_{ads,Si[OH]}$ (mL solution/g zeolite) (0.06 g zeolite per 0.4 mL solution	1.84	1.81 (2% decrease)
$K_{ads,S1}$ (mL solution/g zeolite) (0.18 g zeolite per 0.4 mL solution)	0.74	0.74 (no change)
$K_{ads,S2}$ (mL solution/g zeolite) (0.1-0.18 g zeolite per 0.4 mL solution)	0.49	0.48 (2% decrease)
$K_{ads,Si[F]}$ (mL solution/g zeolite) (0.12-0.18 g zeolite per 0.4 mL solution)	0.06	0.05 (17% decrease)

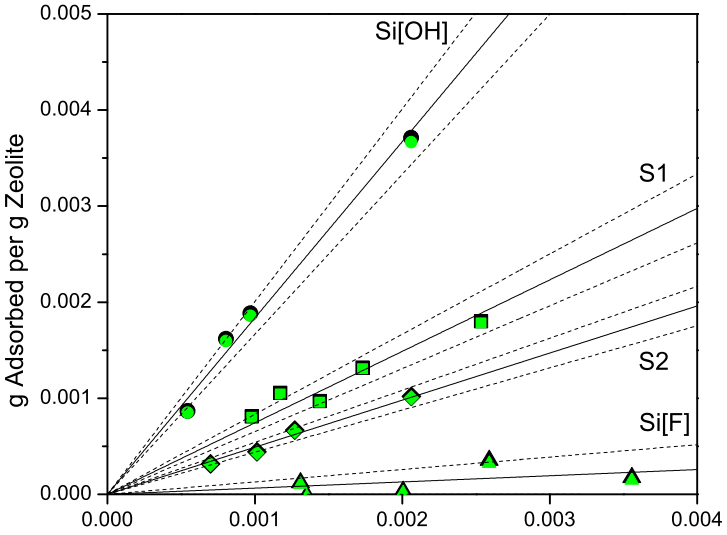

Figure 5.21: Aqueous ethylene glycol adsorption on silicalite-1 at 298 K. Black points/lines are for the assumption that there is no volume change, and green points are for a volume change with polyol adsorption.

$$Py_i = P_i^{sat} x_i, \tag{5.16}$$

where P is the total system pressure, y_i is the mole fraction of species i in the vapor phase, $P_\mathrm{i}^\mathrm{sat}$ is the vapor pressure of species i at the system pressure and temperature, and x_i is the mole fraction of species i in the liquid phase. Note that the mole fractions of the final solutions were calculated as described in the previous section. When interactions between species in the liquid phase cannot be neglected, one must account for these non-idealities and the expression above now becomes

$$Py_i = P_i^{sat} \gamma_i x_i. \tag{5.17}$$

The activity coefficients for different concentrations of propylene glycol in water, γ_1, were calculated using the binary form of the Wilson equation,

$$\ln \gamma_1 = -\ln\left(x_1 + \Lambda_{12} x_2\right) + x_2 \left(\frac{\Lambda_{12}}{x_1 + \Lambda_{12} x_2} - \frac{\Lambda_{21}}{\Lambda_{21} x_1 + x_2} \right), \tag{5.18}$$

where x_1 and x_2 are the mole fractions of propylene glycol (1) and water (2) in the system, respectively, and Λ_{12} and Λ_{21} are defined as

$$\Lambda_{12} = \frac{\upsilon_2}{\upsilon_1} \exp\left(-\frac{\lambda_{12} - \lambda_{11}}{RT}\right), \tag{5.19}$$

$$\Lambda_{21} = \frac{\upsilon_1}{\upsilon_2} \exp\left(-\frac{\lambda_{21} - \lambda_{22}}{RT}\right), \tag{5.20}$$

where υ_1 and υ_2 are the pure component molar volumes at the system temperature, T, and λ_{11}, λ_{12}, λ_{21} and λ_{22} are molecular interaction parameters independent of the system composition and temperature. Suleiman *et al.* reported values for these parameters, which we used to calculate the activity coefficients for our systems.[87] These parameters as well as the molar volumes used in our calculations are shown in Table 5.5.

Table 5.5: Wilson equation parameter values used to calculate activity coefficients.

	λ_{11} (kJ mol^{-1})	λ_{12} (kJ mol^{-1})	λ_{22} (kJ mol^{-1})	υ_1 (cm^3 mol^{-1})		υ_2 (cm^3 mol^{-1})	
				298 K	333 K	298 K	333 K
Propylene glycol (1) in water (2)	10.86[a]	9.99[a]	8.30[a]	73.73[b]	75.64[c]	18[d]	18.31[e]

[a]Values reported by Suleiman *et al.*[87] [b]Calculated from a propylene glycol density of 1.032 g cm^{-3}. [c]Calculated from a propylene glycol density of 1.006 g cm^{-3}. [d]Calculated from a water density of 1 g cm^{-3}. [e]Calculated from a water density of 0.9832 g cm^{-3}.

A comparison of the adsorption isotherms for propylene glycol adsorption on Si[F] at 333 K with and without consideration of solution non-idealities is presented in Figure 5.22. It can be observed that calculation of the partial pressures by Raoult's law overestimates the propylene glycol partial pressure by approximately 15% for all points on the adsorption isotherm.

Xiong *et al.* reported another approach, and related aqueous solution concentrations to partial pressure by

$$P_i = \rho RT \exp\left(\frac{\mu^{\infty}_{ex,i}}{RT}\right) x_i, \tag{5.21}$$

where P_i is the partial pressure of component i, ρ is the solvent density since the solute concentration is considered dilute, $\mu^{\infty}_{\mathrm{ex,i}}$ is the excess chemical potential at infinite dilution, and x_i is the mole fraction of component i in solution.[4,5]

The authors reported a value for $\mu^{\infty}_{\mathrm{ex,i}}$ of -37.6 ± 0.7 kJ mol^{-1}, which was calculated using their expanded ensemble (EE) simulation.[4] Although this approach is only valid at infinite dilution, where each propylene glycol molecule is surrounded by water molecules,

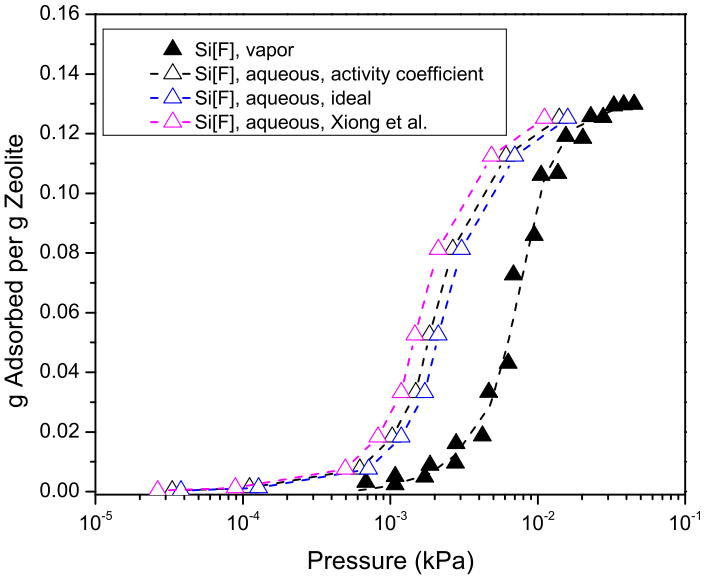

Figure 5.22: Aqueous propylene glycol adsorption on Si[F] at 333 K with pressures calculated with an activity coefficient of one (ideal solution), non-unity activity coefficients, and with the method of Xiong *et al.*[4,5]

we also calculated partial pressures using this method and these are shown in Figure 5.22. It can be observed that the pressures calculated from this method are consistently ∼20% lower that the values calculated with activity coefficients.

Based on these analyses, the pressures reported for aqueous adsorption data at 333 K in this dissertation were calculated using non-unity activity coefficients per Equation 5.17. It should be noted from Figure 5.22 that regardless of the method for calculating partial pressures for the aqueous adsorption isotherms, the conclusion is the same- water promotes adsorption of propylene glycol on Si[F]. For example, it would require an activity coefficient of over 2.5 to reconcile the difference between aqueous and vapor propylene glycol adsorption at loadings of 0.02-0.03 g per g zeolite.

Xiong *et al.* reported K_{ads} values for their aqueous propylene glycol adsorption data in units of mL solution per g zeolite. In order to obtain a K_{ads} in units that allowed quantitative comparison with their vapor propylene glycol K_{ads} value, conversion of the aqueous data from units of concentration to units of pressure was required. Activity coefficients for aqueous adsorption data at 298 K were calculated and found to be ∼0.99, resulting in less than 1% difference in the corresponding partial pressures. Therefore, partial pressures for these data were calculated using Equation 5.16.

5.5.5 Effect of Non-Ideal Solution Interactions on K_{ads}

We showed in Chapter 3 that the K_{ads} we measure, which is referred to as $K_{\text{ads,measured}}$in this section, is defined as

$$K_{ads,measured} = \gamma_i K_{ads,intrinsic} \tag{5.22}$$

where $K_{\text{ads,intrinsic}}$ is the Henry's constant for pure liquid polyol adsorption, and γ_{i} is the activity coefficient for the polyol in water. Since the concentrations we report for aqueous adsorption of 1,2-butanediol, propylene glycol, and ethylene glycol onto the silicalite-1 materials at 298 K are within the concentrations used by Sulieman and Eckert[87] to obtain infinite-dilution activity coefficients for diols in water (0.01-0.1 mole percent), it is assumed that the infinite-dilution activity coefficients they report (2.0 for 1,2-butanediol, 1.0 for propylene glycol, and 0.8 for ethylene glycol) are appropriate for calculating $K_{\text{ads,intrinsic}}$for our polyol-water systems.

A comparison of the $K_{\text{ads,intrinsic}}$ and $K_{\text{ads,measured}}$values for 1,2-butanediol, propylene glycol, and ethylene glycol for the silicalite-1 materials is presented in Figure 5.23. Two conclusions can be drawn from this comparison: 1) propylene glycol/ethylene glycol selectivity is greater than 1 regardless of solution interactions, and 2) the linear relationship between K_{ads} and silanol defect density is unaffected by decoupling of solution interactions.

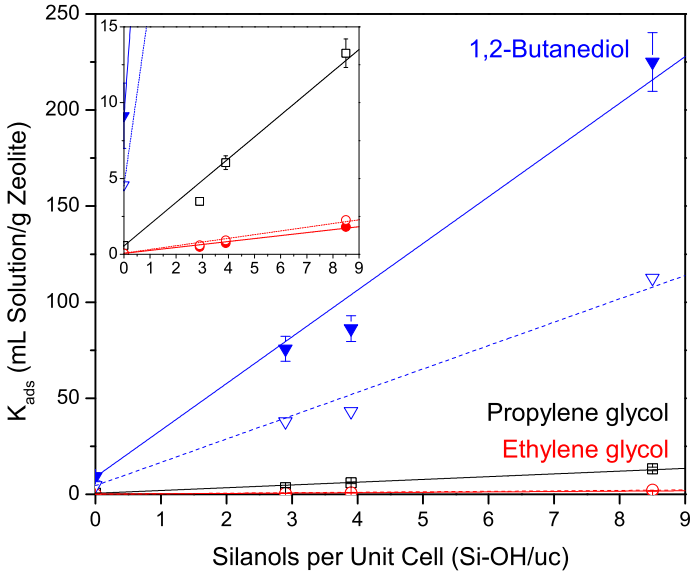

Figure 5.23: $K_{\text{ads,measured}}$ (closed symbols) and $K_{\text{ads,intrinsic}}$(open symbols) versus silanol defect density (Si-OH/uc) for aqueous 1,2-butanediol, propylene glycol, and ethylene glycol adsorption on Si[OH], S1, S2, and Si[F] at 298 K. Lines represent least-squares linear regressions. Error bars represent 95% confidence intervals. Inset: Magnified view of K_{ads} values below 15 mL Solution/g Zeolite.

This material is based upon work supported by the Catalysis Center for Energy Innovation, an EFRC funded by the U.S. Department of Energy (Award Number DE SC0001004). We acknowledge Dr. Sonjong Hwang at the Caltech Solid State NMR Facility for the NMR analyses. We thank Mr. Peng Bai and Mr. Mark Mazar for assistance with the simulated XRD patterns.

CHAPTER

SIX

FUTURE DIRECTIONS

Aqueous and vapor phase adsorption isotherms of oxygenates with functionality representative of biomass were presented and analyzed with respect to the zeolite and oxygenate properties to elucidate the roles of adsorbate-water, adsorbate-zeolite, and adsorbate-adsorbate interactions on adsorption affinity. The critical role of confinement on oxygenate adsorption was highlighted by several results including an exponential increase in Henry's constant, K_{ads}, with oxygenate carbon number and a decrease in K_{ads} with zeolite pore size. This conclusion was further supported by the observation that the K_{ads}-K_{ow} correlation for 1,2-diols is unperturbed by adsorbate-water interactions.

However, several unanswered questions remain regarding the effect of adsorbate-water interactions on oxygenate adsorption affinity. For example, an order of magnitude change in K_{ads} was identified with an increase from 2 to 3 alcohol functional groups in Chapter 2, and the interactions responsible for this change are still not clear. Specifically, the decrease in K_{ads} could be the result of increased molecule hydrophilicity, thus making it energetically preferable for the molecule to partition into the bulk with water rather than enter the lipophilic zeolite pores. Alternatively, the decrease in K_{ads} with increasing -OH number could result from a change in the molecule's adsorption configuration in the zeolite pores. Adsorption experiments in which water is eliminated from the system would probe the effect of adsorbate functionality on adsorbate-zeolite interactions. On this basis, a recommended starting point for future work is measurement of vapor glycerol adsorption on the silicalite-1 materials from Chapter 5, and upon comparison with the vapor propylene glycol data reported in Chapter 5, the role of -OH number on adsorbate-zeolite interactions could be uncovered.

While aqueous K_{ads} data for many oxygenate-zeolite systems were presented in this dissertation, there are still very few reports of vapor oxygenate K_{ads} and ΔH_{ads} values, and

these are currently limited to alcohol adsorbates. It is necessary for these measurements to be made in order to interpret catalytic data, and this need is growing with the increasing interest in biomass conversion technologies. Therefore, it is recommended that vapor phase calorimetric measurements are performed on oxygenates with functionality representative of biomass (*e.g.* polyols, aldehydes, and ketones). A comparison of the heats of adsorption for these molecules would also provide information on the effect of molecule functionality on adsorbate-zeolite interactions.

Future work focused on implementation of zeolites as membranes and adsorbents for oxygenate separations is also recommended. It was identified that small pore FER results in an order of magnitude decrease in aqueous K_{ads} with increasing oxygenate branching (*e.g.* compare 1,3-propanediol with propylene glycol), which is postulated to be the result of pore size exclusion. It would be interesting to explore opportunities to exploit this phenomenon to separate oxygenates in aqueous solutions with similar K_{ow} values.

It is the hope of this author that the data presented here will also be useful in the development of computational approaches to study oxygenate adsorption on zeolites. These studies have the potential to provide a wealth of information on the interactions between oxygenates and the zeolite framework, and as was postulated from results in Chapter 5, they could probe adsorbate-adsorbate and adsorbate-water interactions in the zeolite framework. Specific questions that would be interesting to address are the effect of oxygen functionality on adsorption configuration, and whether branched polyols in fact adsorb at the pore mouths of FER.

BIBLIOGRAPHY

[1] *Top Value Added Chemicals from Biomass*, volume 1. U.S. Department of Energy, (2004).

[2] Vankoningsveld, H., Jansen, J. C., and Vanbekkum, H. *Zeolites* **10**(4), 235–242 (1990).

[3] Vankoningsveld, H., Vanbekkum, H., and Jansen, J. C. *Acta Crystallographica Section B-Structural Science* **43**, 127–132 (1987).

[4] Xiong, R., Sandler, S. I., and Vlachos, D. G. *Langmuir* **28**(9), 4491–4499 (2012).

[5] Xiong, R., Sandler, S. I., and Vlachos, D. G. *Journal of Physical Chemistry C* **115**(38), 18659–18669 (2011).

[6] Ranjan, R., Thust, S., Gounaris, C. E., Woo, M., Floudas, C. A., von Keitz, M., Valentas, K. J., Wei, J., and Tsapatsis, M. *Microporous and Mesoporous Materials* **122**(1-3), 143–148 (2009).

[7] Corma, A., Iborra, S., and Velty, A. *Chemical Reviews* **107**(6), 2411–2502 (2007).

[8] Huang, H.-J., Ramaswamy, S., Tschirner, U. W., and Ramarao, B. V. *Separation and Purification Technology* **62**(1), 1–21 (2008).

[9] Ruthven, D. M. *Principles of Adsorption and Adsorption Processes.* John Wiley Sons, Inc., New York, (1984).

[10] Krishna, R. and Wesselingh, J. A. *Chemical Engineering Science* **52**(6), 861–911 (1997).

[11] Davis, M. E. and Lobo, R. F. *Chemistry of Materials* **4**(4), 756–768 (1992).

[12] Baerlocher, C. and McCusker, L. *Database of Zeolite Structures http://www.iza-structure.org/databases/* (2007).

[13] Sherman, J. D. *Proceedings of the National Academy of Sciences of the United States of America* **96**(7), 3471–3478 (1999).

[14] Eder, F., Stockenhuber, M., and Lercher, J. A. *Journal of Physical Chemistry B* **101**(27), 5414–5419 (1997).

[15] Savitz, S., Siperstein, F., Gorte, R. J., and Myers, A. L. *Journal of Physical Chemistry B* **102**(35), 6865–6872 (1998).

[16] Davis, M. E. and Davis, R. J. *Fundamentals of Chemical Reaction Engineering.* MGraw-Hill, (2003).

[17] Zhang, K., Lively, R. P., Noel, J. D., Dose, M. E., McCool, B. A., Chance, R. R., and Koros, W. J. *Langmuir* **28**(23), 8664–8673 (2012).

[18] Smit, B. and Siepmann, J. I. *Science* **264**(5162), 1118–1120 (1994).

[19] Eder, F. and Lercher, J. A. *Zeolites* **18**(1), 75–81 (1997).

[20] Denayer, J. F., Souverijns, W., Jacobs, P. A., Martens, J. A., and Baron, G. V. *Journal of Physical Chemistry B* **102**(23), 4588–4597 (1998).

[21] Denayer, J. F., Baron, G. V., Martens, J. A., and Jacobs, P. A. *Journal of Physical Chemistry B* **102**(17), 3077–3081 (1998).

[22] Denayer, J. F. M., Ocakoglu, R. A., Thybaut, J., Marin, G., Jacobs, P., Martens, J., and Baron, G. V. *Journal of Physical Chemistry B* **110**(17), 8551–8558 (2006).

[23] Lee, C. C., Gorte, R. J., and Farneth, W. E. *Journal of Physical Chemistry B* **101**(19), 3811–3817 (1997).

[24] Thamm, H. *Journal of the Chemical Society-Faraday Transactions I* **85**, 1–9 (1989).

[25] Dubinin, M. M., Rakhmatkariev, G. U., and Isirikyan, A. A. *Bulletin of the Academy of Sciences of the Ussr Division of Chemical Science* **38**(9), 1950–1953 (1989).

[26] Nguyen, C. M., Reyniers, M. F., and Marin, G. B. *Physical Chemistry Chemical Physics* **12**(32), 9481–9493 (2010).

[27] Ma, L. and Yang, R. T. *Industrial Engineering Chemistry Research* **46**(14), 4874–4882 (2007).

[28] Ma, L. and Yang, R. T. *Industrial Engineering Chemistry Research* **46**(9), 2760–2768 (2007).

[29] Trzpit, M., Soulard, M., Patarin, J., Desbiens, N., Cailliez, F., Boutin, A., Demachy, I., and Fuchs, A. H. *Langmuir* **23**(20), 10131–10139 (2007).

[30] Chen, X., Ping, Z. H., and Long, Y. C. *Journal of Applied Polymer Science* **67**(4), 629–636 (1998).

[31] Christensen, C. H., Rass-Hansen, J., Marsden, C. C., Taarning, E., and Egeblad, K. *Chemsuschem* **1**(4), 283–289 (2008).

[32] Petrus, L. and Noordermeer, M. A. *Green Chemistry* **8**(10), 861–867 (2006).

[33] Xiu, Z. L. and Zeng, A. P. *Applied Microbiology and Biotechnology* **78**(6), 917–926 (2008).

[34] Caro, J., Noack, M., Kolsch, P., and Schafer, R. *Microporous and Mesoporous Materials* **38**(1), 3–24 (2000).

[35] Corma, A. and Orchilles, A. V. *Microporous and Mesoporous Materials* **35-6**, 21–30 (2000).

[36] Butler, A. C. and Nicolaides, C. P. *Catalysis Today* **18**(4), 443–471 (1993).

[37] Feller, A. and Lercher, J. A. *Advances in Catalysis, Vol 48* **48**, 229–295 (2004).

[38] Weitkamp, J. and Traa, Y. *Catalysis Today* **49**(1-3), 193–199 (1999).

[39] Eder, F. and Lercher, J. A. *Journal of Physical Chemistry B* **101**(8), 1273–1278 (1997).

[40] Ison, A. and Gorte, R. J. *Journal of Catalysis* **89**(1), 150–158 (1984).

[41] Nakamoto, H. and Takahashi, H. *Zeolites* **2**(2), 67–68 (1982).

[42] Mirth, G., Lercher, J. A., Anderson, M. W., and Klinowski, J. *Journal of the Chemical Society-Faraday Transactions* **86**(17), 3039–3044 (1990).

[43] Long, Y. C., Jiang, H. W., and Zeng, H. *Langmuir* **13**(15), 4094–4101 (1997).

[44] Li, S., Tuan, V. A., er, J. L., and Noble, R. D. *Microporous and Mesoporous Materials* **53**(1-3), 59–70 (2002).

[45] Li, S. G., Tuan, V. A., Falconer, J. L., and Noble, R. D. *Chemistry of Materials* **13**(5), 1865–1873 (2001).

[46] Li, S. G., Tuan, V. A., Falconer, J. L., and Noble, R. D. *Industrial and Engineering Chemistry Research* **40**(8), 1952–1959 (2001).

[47] Li, S. G., Tuan, V. A., Falconer, J. L., and Noble, R. D. *Journal of Membrane Science* **191**(1-2), 53–59 (2001).

[48] de Moor, P.-P. E. A., Beelen, T. P. M., and van Santen, R. A. *Journal of Physical Chemistry B* **103**(10), 1639–1650 (1999).

[49] Narkhede, V. V. and Gies, H. *Chemistry of Materials* **21**(18), 4339–4346 (2009).

[50] Kruk, M., Jaroniec, M., Ko, C. H., and Ryoo, R. *Chemistry of Materials* **12**(7), 1961–1968 (2000).

[51] Fan, W., Snyder, M. A., Kumar, S., Lee, P. S., Yoo, W. C., McCormick, A. V., Penn, R. L., Stein, A., and Tsapatsis, M. *Nature Materials* **7**(12), 984–991 (2008).

[52] Schmidt, I., Madsen, C., and Jacobsen, C. J. H. *Inorganic Chemistry* **39**(11), 2279–2283 (2000).

[53] Maheshwari, S., Jordan, E., Kumar, S., Bates, F. S., Penn, R. L., Shantz, D. F., and Tsapatsis, M. *Journal of the American Chemical Society* **130**(4), 1507–1516 (2008).

[54] He, Y. J., Nivarthy, G. S., Eder, F., Seshan, K., and Lercher, J. A. *Microporous and Mesoporous Materials* **25**(1-3), 207–224 (1998).

[55] Olson, D. H., Haag, W. O., and Lago, R. M. *Journal of Catalysis* **61**(2), 390–396 (1980).

[56] Sano, T., Kasuno, T., Takeda, K., Arazaki, S., and Kawakami, Y. In *Progress in Zeolite and Microporous Materials, Pts A-C*, volume 105 of *Studies in Surface Science and Catalysis*, 1771–1778. Elsevier, Amsterdam (1997).

[57] Flanigen, E. M., Bennett, J. M., Grose, R. W., Cohen, J. P., Patton, R. L., Kirchner, R. M., and Smith, J. V. *Nature* **271**(5645), 512–516 (1978).

[58] Marcolli, C. and Peter, T. *Atmospheric Chemistry and Physics* **5**, 1545–1555 (2005).

[59] Smit, B. and Maesen, T. L. M. *Nature* **374**(6517), 42–44 (1995).

[60] Vlugt, T. J. H., Krishna, R., and Smit, B. *Journal of Physical Chemistry B* **103**(7), 1102–1118 (1999).

[61] Bates, S. P., vanWell, W. J. M., vanSanten, R. A., and Smit, B. *Journal of Physical Chemistry* **100**(44), 17573–17581 (1996).

[62] Ryoo, R., Ko, C. H., Kruk, M., Antochshuk, V., and Jaroniec, M. *Journal of Physical Chemistry B* **104**(48), 11465–11471 (2000).

[63] Lukens, W. W., Schmidt-Winkel, P., Zhao, D. Y., Feng, J. L., and Stucky, G. D. *Langmuir* **15**(16), 5403–5409 (1999).

[64] Pieterse, J. A. Z., Veefkind-Reyes, S., Seshan, K., and Lercher, J. A. *Journal of Physical Chemistry B* **104**(24), 5715–5723 (2000).

[65] Beerdsen, E., Dubbeldam, D., Smit, B., Vlugt, T. J. H., and Calero, S. *Journal of Physical Chemistry B* **107**(44), 12088–12096 (2003).

[66] June, R. L., Bell, A. T., and Theodorou, D. N. *Journal of Physical Chemistry* **94**(4), 1508–1516 (1990).

[67] Eder, F. and Lercher, J. A. *Journal of Physical Chemistry* **100**(41), 16460–16462 (1996).

[68] Mallon, E. E., Bhan, A., and Tsapatsis, M. *Journal of Physical Chemistry B* **114**(5), 1939–1945 (2010).

[69] De Vos, D. E., Denayer, J., van Laar, F., Baron, G. V., and Jacobs, P. A. *Topics in Catalysis* **23**(1-4), 191–198 (2003).

[70] Langhendries, G., De Vos, D. E., Baron, G. V., and Jacobs, P. A. *Journal of Catalysis* **187**(2), 453–463 (1999).

[71] Ramachandran, C. E., Du, H. W., Kim, Y. J., Kung, M. C., Snurr, R. Q., and Broadbelt, L. J. *Journal of Catalysis* **253**(1), 148–158 (2008).

[72] Davis, L. *Bioorganic Chemistry* **2**(3), 197–201 (1973).

[73] Yaylayan, V. A., Harty-Marjors, S., and Ismail, A. A. *Carbohydrate Research* **318**, 20–25 (1999).

[74] SRC. *Interactive PhysProp Database Demo http://www.syrres.com/what-we-do/databaseforms.aspx?id=386.*

[75] Sangster. *LOGKOW: A databank of evaluated octanol-water partition coefficients. http://logkow.cisti.nrc.ca/logkow/index.jsp.*

[76] Cheng, T., Zhao, Y., Li, X., Lin, F., Xu, Y., Zhang, X., Li, Y., Wang, R., and Lai, L. *Journal of Chemical Information and Modeling* **47**(6), 2140–2148 (2007).

[77] Ghose, A. K., Viswanadhan, V. N., and Wendoloski, J. J. *Journal of Physical Chemistry A* **102**(21), 3762–3772 (1998).

[78] Leo, A. and Hoekman, D. *Perspectives in Drug Discovery and Design* **18**(1), 19–38 (2000).

[79] Viswanadhan, V. N., Ghose, A. K., Revankar, G. R., and Robins, R. K. *Journal of Chemical Information and Computer Sciences* **29**(3), 163–172 (1989).

[80] Meylan, W. and Howard, P. *Perspectives in Drug Discovery and Design* **19**(1), 67–84 (2000).

[81] Moriguchi, I., Hirono, S., Liu, Q., Nakagome, I., and Matsushita, Y. *Chemical and Pharmaceutical Bulletin* **40**(1), 127–130 (1992).

[82] Tetko, I. V., Tanchuk, V. Y., and Villa, A. E. P. *Journal of Chemical Information and Computer Sciences* **41**(5), 1407–1421 (2001).

[83] Tetko, I. V. and Tanchuk, V. Y. *Journal of Chemical Information and Computer Sciences* **42**(5), 1136–1145 (2002).

[84] Krishna, R. and van Baten, J. M. *Langmuir* **26**(13), 10854–10867 (2010).

[85] Smit, B. *Chemical Reviews* **108**(10), 4125–4184 (2008).

[86] Vlugt, T. J. H., Zhu, W., Kapteijn, F., Moulijn, J. A., Smit, B., and Krishna, R. *Journal of the American Chemical Society* **120**(22), 5599–5600 (1998).

[87] Suleiman, D. and Eckert, C. A. *Journal of Chemical Engineering Data* **39**(4), 692–696 (1994).

[88] Tochigi, K., Uchiyama, M., and Kojima, K. *Korean Journal of Chemical Engineering* **17**(5), 502–505 (2000).

[89] Chen, B. and Siepmann, J. I. *Journal of the American Chemical Society* **122**(27), 6464–6467 (2000).

[90] Yang, X. B., Camblor, M. A., Lee, Y., Liu, H. M., and Olson, D. H. *Journal of the American Chemical Society* **126**(33), 10403–10409 (2004).

[91] Olson, D. H., Yang, X. B., and Camblor, M. A. *Journal of Physical Chemistry B* **108**(30), 11044–11048 (2004).

[92] van Well, W. J. M., Cottin, X., de Haan, J. W., Smit, B., Nivarthy, G., Lercher, J. A., van Hooff, J. H. C., and van Santen, R. A. *Journal of Physical Chemistry B* **102**(20), 3945–3951 (1998).

[93] Yoda, E., Kondo, J. N., Wakabayashi, F., and Domen, K. *Physical Chemistry Chemical Physics* **5**(15), 3306–3310 (2003).

[94] Ching, C. B. and Ruthven, D. M. *Zeolites* **8**(1), 68–73 (1988).

[95] Barrer R, M. and Cram P, J. *Heats of Immersion of Outgassed Ion-Exchanged Zeolites*, volume 102 of *Advances in Chemistry*, chapter 47, 105–131. American Chemical Society (1971).

[96] Matsumoto, Y., Touhara, H., Nakanishi, K., and Watanabe, N. *The Journal of Chemical Thermodynamics* **9**(8), 801–805 (1977).

[97] Knauth, P. and Sabbah, R. *Thermochimica Acta* **164**(0), 145–152 (1990).

[98] Knauth, P. and Sabbah, R. *Structural Chemistry* **1**(1), 43–46 (1990).

[99] Burgess, D. *Thermochemical Data*. National Institute of Standards and Technology, Gaithersburg M.D. 20899 (2012).

[100] *Dow Propylene Glycol, Industrial Grade Technical Data Sheet*. Dow Chemical Company, Form No. 117-01540-0604X-AA.

[101] Domalski, E. and Hearing, E. *Condensed Phase Heat Capacity Data*. National Institute of Standards and Technology, Gaithersburg M.D. 20899 (2012).

[102] Piccione, P. M., Yang, S., Navrotsky, A., and Davis, M. E. *The Journal of Physical Chemistry B* **106**(14), 3629–3638 (2002).

[103] Vane, L. M. *Journal of Chemical Technology and Biotechnology* **80**(6), 603–629 (2005).

[104] Bowen, T. C., Noble, R. D., and Falconer, J. L. *Journal of Membrane Science* **245**(1-2), 1–33 (2004).

[105] Mallon, E. E., Babineau, I. J., Kranz, J. I., Guefrachi, Y., Siepmann, J. I., Bhan, A., and Tsapatsis, M. *Journal of Physical Chemistry B* **115**(39), 11431–11438 (2011).

[106] Lin, X., Chen, X. S., Kita, H., and Okamoto, K. *AIChE Journal* **49**(1), 237–247 (2003).

[107] Chezeau, J. M., Delmotte, L., Guth, J. L., and Gabelica, Z. *Zeolites* **11**(6), 598–606 (1991).

[108] Koller, H., Lobo, R. F., Burkett, S. L., and Davis, M. E. *Journal of Physical Chemistry* **99**(33), 12588–12596 (1995).

[109] Flanigen, E. M. and Patton, R. L. *US Patent No. 4073865* (1978).

[110] Chezeau, J. M., Delmotte, L., Guth, J. L., and Soulard, M. *Zeolites* **9**(1), 78–80 (1989).

[111] Navarro, M., Mayoral, A., Mateo, E., Lahoz, R., de la Fuente, G. F., and Coronas, J. *ChemPhysChem* **13**(3), 736–740 (2012).

[112] *Materials Studio, Release 6.0*. Accelyrs Software Inc., San Diego, (2011).

[113] *Origin, Release 8.5.1*. OriginLab, Northampton, (2011).

[114] Curme, G. O. and Johnston, F. *Glycols*. Reinhold, New York, (1953).

[115] Hay, D. G. and Jaeger, H. *Journal of the Chemical Society-Chemical Communications* (21), 1433–1433 (1984).

[116] Inui, M., Ikeda, T., Suzuki, T., Sugita, K., and Mizukami, F. *Bulletin of the Chemical Society of Japan* **82**(9), 1160–1169 (2009).

[117] Heitmann, G. P., Dahlhoff, G., and Holderich, W. F. *Journal of Catalysis* **186**(1), 12–19 (1999).

[118] Wu, E. L., Lawton, S. L., Olson, D. H., Rohrman, A. C., and Kokotailo, G. T. *Journal of Physical Chemistry* **83**(21), 2777–2781 (1979).

[119] Engelhardt, G. and Michel, D. *High-Resolution Solid-State NMR of Silicates and Zeolites*. John Wiley and Sons, Chichester, (1987).

[120] Llewellyn, P. L., Coulomb, J. P., Grillet, Y., Patarin, J., Andre, G., and Rouquerol, J. *Langmuir* **9**(7), 1852–1856 (1993).

[121] Saito, A. and Foley, H. C. *Microporous Materials* **3**(4-5), 543–556 (1995).

[122] Llewellyn, P., Coulomb, J. P., Reichert, H., Patarin, J., Grillet, Y., and Rouquerol, J. *Journal of Thermal Analysis* **38**(4), 683–692 (1992).

[123] Borghard, W. S., Reischman, P. T., and Sheppard, E. W. *Journal of Catalysis* **139**(1), 19–23 (1993).

[124] Muller, U., Reichert, H., Robens, E., Unger, K. K., Grillet, Y., Rouquerol, F., Rouquerol, J., Pan, D. F., and Mersmann, A. *Fresenius Zeitschrift Fur Analytische Chemie* **333**(4-5), 433–436 (1989).

[125] Muller, U., Unger, K. K., Pan, C., Mersmann, A., Grillet, Y., Rouquerol, F., and Rouquerol, J. In *Zeolites as Catalysts, Sorbents, and Detergent Builders,* Karge, H. G. and Weitkamp, J., editors. Elsevier, (1988).

[126] Guth, J. L., Kessler, H., and Wey, R. 121. Elsevier, Amsterdam (1986).

[127] Pellenq, R. J. M. and Nicholson, D. *Langmuir* **11**(5), 1626–1635 (1995).

[128] Garcia-Perez, E., Parra, J. B., Ania, C. O., Dubbeldam, D., Vlugt, T. J. H., Castillo, J. M., Merkling, P. J., and Calero, S. *Journal of Physical Chemistry C* **112**(27), 9976–9979 (2008).

[129] Engelhardt, G. and Vankoningsveld, H. *Zeolites* **10**(7), 650–656 (1990).

[130] Rouqurol, F., Rouquerol, J., and Sing, K. *Adsorption by Powders and Porous Solids: Principles, Methodology and Applications.* Academic Press, (1999).

[131] Halasz, I., Kim, S., and Marcus, B. *Journal of Physical Chemistry B* **105**(44), 10788–10796 (2001).

[132] Ahunbay, M. G. *Langmuir* **27**(8), 4986–4993 (2011).

[133] Kuhn, J., Castillo-Sanchez, J. M., Gascon, J., Calero, S., Dubbeldam, D., Vlugt, T. J. H., Kapteijn, F., and Gross, J. *Journal of Physical Chemistry C* **113**(32), 14290–14301 (2009).

[134] Romero, C. M., Paez, M. S., and Perez, D. *Journal of Chemical Thermodynamics* **40**(12), 1645–1653 (2008).

[135] Romero, C. M., Lozano, J. M., and Giraldo, G. I. *Physics and Chemistry of Liquids* **46**(1), 78–85 (2008).

[136] Ambrosone, L., Sartorio, R., Vescio, A., and Vitagliano, V. *Journal of the Chemical Society-Faraday Transactions* **92**(7), 1163–1166 (1996).

[137] Zhang, X., Liu, D., Xu, D., Asahina, S., Cychosz, K. A., Agrawal, K. V., Al Wahedi, Y., Bhan, A., Al Hashimi, S., Terasaki, O., Thommes, M., and Tsapatsis, M. *Science* **336**(6089), 1684–1687 (2012).

[138] Karger, J. and Ruthven, D. M. *Diffusion in Zeolites.* Wiley, New York, (1992).

[139] Gueudre, L., Jolimaite, E., Bats, N., and Dong, W. *Adsorption-Journal of the International Adsorption Society* **16**(1-2), 17–27 (2010).

[140] Gueudre, L., Bats, N., and Jolimaitre, E. *Microporous and Mesoporous Materials* **147**(1), 310–317 (2012).

[141] Wloch, J. *Microporous and Mesoporous Materials* **62**(1-2), 81–86 (2003).

[142] Kortunov, P., Chmelik, C., Karger, J., Rakoczy, R. A., Ruthven, D. M., Traa, Y., Vasenkov, S., and Weitkamp, J. *Adsorption-Journal of the International Adsorption Society* **11**(3-4), 235–244 (2005).

[143] Choudhary, V. R., Nayak, V. S., and Mamman, A. S. *Industrial Engineering Chemistry Research* **31**(2), 624–628 (1992).

[144] Stewart, G. W. *Physical Review* **37**(1), 9–16 (1931).

[145] Morgan, J. and Warren, B. E. *The Journal of Chemical Physics* **6**(11), 666–673 (1938).

[146] Soper, A. K. *Journal of Physics-Condensed Matter* **19**(33) (2007).

[147] Hura, G., Russo, D., Glaeser, R. M., Head-Gordon, T., Krack, M., and Parrinello, M. *Physical Chemistry Chemical Physics* **5**(10), 1981–1991 (2003).

[148] Wikfeldt, K. T., Leetmaa, M., Ljungberg, M. P., Nilsson, A., and Pettersson, L. G. M. *The Journal of Physical Chemistry B* **113**(18), 6246–6255 (2009).

APPENDIX

A

MASS TRANSFER MODELING OF ADSORPTION KINETICS ON ZEOLITES

Introduction

It was found that some of the points on the vapor propylene glycol adsorption isotherms presented in Chapter 5 would take several days to reach equilibrium. The root cause of this long equilibration time was investigated through mass transfer modeling of the adsorption kinetics. It was identified that the slow equilibration time may be the result of the slow adsorbate delivery rate.

Methods

Adsorption Experiments

All kinetic vapor adsorption data presented was collected using a Shimadzu TGA-50 thermobalance. The entire apparatus is described in detail in Chapter 5.

Materials used in the vapor adsorption experiments include H-MFI, 3DOm-MFI, and self-pillared pentasil (SPP). The H-MFI (CBV28014 from Zeolyst) and 3DOm-MFI materials are described in Section 2.2.1. The synthesis for SPP is described by Zhang *et al.*[137]

Mass Transfer Models

It was assumed that the rate of adsorption was much slower than the vapor convection rate and, therefore, the TGA was modeled as a batch system. The mass transfer time constant for the system was obtained by fitting the appropriate dimensionless mass transfer model to the experimental uptake curve.

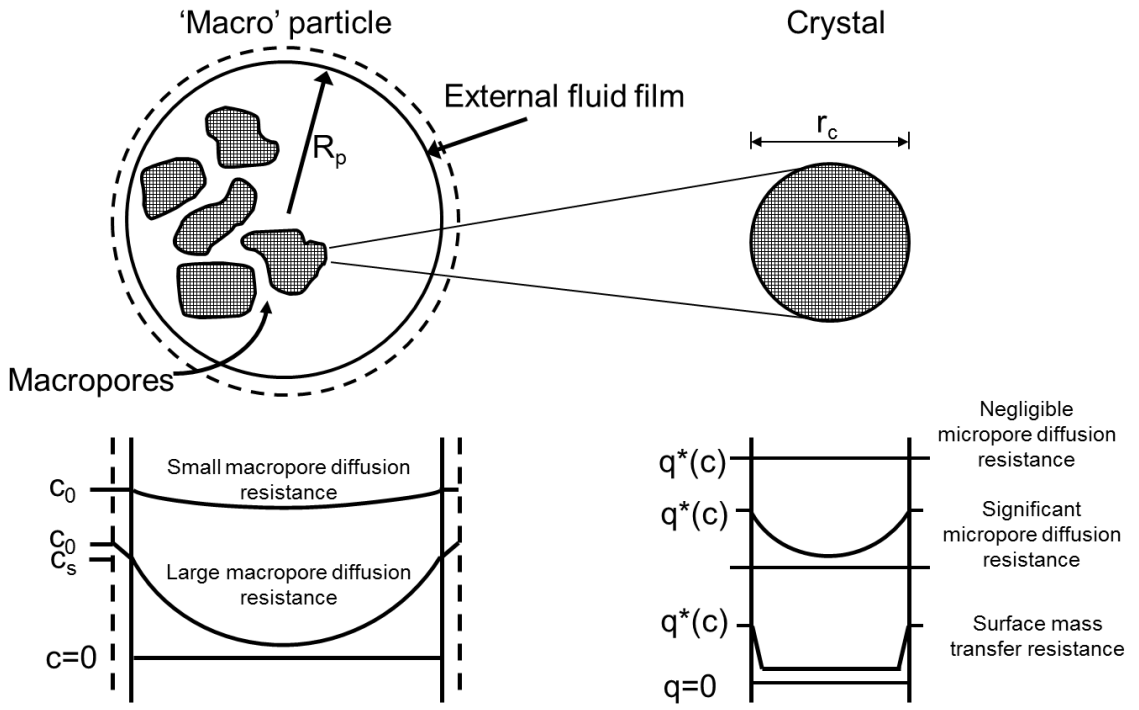

Figure A.1: Schematic of the sources and corresponding concentration profiles for zeolite mass transfer resistance.

Two approaches outlined by Kärger and Ruthven[138] were adopted in the mathematical modeling of the adsorption kinetics that differ in the assumed dominant mass transfer resistance. As shown in Figure A.1, multiple mass transfer resistances exist for a biporous adsorbent including resistance at the crystal surface and micropore diffusional resistance.

Evidence of surface resistance to adsorption, which may be the result of blocked pore mouths on the external crystal surface, has been observed in several transient adsorption experiments reported in the literature.[139–142] Wloch used gravimetry to show that the n-hexane adsorption rate on MFI increased by two orders of magnitude when the as-synthesized crystals were treated with hydrofluoric acid (HF) in a water-acetone solution, and this result was attributed to removal of an amorphous layer on the external crystal surface.[141] Recently, Kortunov *et al.* obtained transient concentration profiles for methanol adsorption on ∼200 micron defect-free pure-silica FER crystals using interference microscopy (IFM) and infrared microscopy (IRM) which provide direct evidence of surface resistance to diffusion.[142] A concentration gradient was measured along the y-axis due to diffusion of methanol through the 8-member ring channels, while concentration was independent of the z-axis position, indicating that the pore mouths of the z-axis 10-member ring channels are blocked.

A simplified approach was taken here in which it was assumed that surface resistance effects are independent of the transport direction. That is, diffusion from the crystal surface to the micropore network is much slower than micropore diffusion in all directions, thus there is no adsorbed phase concentration gradient within the crystal ($\bar{q}$ everywhere within in crystal), and the amount adsorbed on the surface (q^*) is at equilibrium with the fluid phase concentration at the surface. If it is assumed that 1) the particle is spherical, 2) diffusivity is constant, and 3) the system is isothermal (no heat effects from adsorption), then the adsorption rate is described by

$$\frac{d\bar{q}}{dt} = k_s a(q^* - \bar{q}) = \frac{3k_s}{r_c}(q^* - \bar{q}), \tag{A.1}$$

where t is time, k_s is surface mass transfer resistance, which is defined as the ratio of the effective diffusivity and solid film thickness ($k_s = D_s/\delta$), and a is the specific surface area for a spherical particle ($a = 3/r_c$), where r_c is the crystal radius. Integration of Equation A.1 using the initial condition

$$t = 0, \quad \bar{q} = 0 \tag{A.2}$$

yields

$$\frac{m}{m^*} = \frac{\bar{q}}{q^*} = 1 - \exp\left[-\frac{3k_s t}{R_p}\right], \tag{A.3}$$

and this is the equation for surface resistance used to model the results presented here.

Note that a mathematically similar result is obtained for external fluid film mass transfer control,

$$\frac{m}{m^*} = \frac{\bar{q}}{q^*} = 1 - \exp\left[-\frac{3k_f t}{KR_p}\right], \tag{A.4}$$

where k_f is the film mass transfer coefficient, K is the equilibrium coefficient between the fluid phase concentration, C, and the equilibrium adsorbed concentration, q^*, and R_p is the macroparicle radius. Note that an assumption to obtain Equation A.4 is that the adsorbed phase concentration change is sufficiently small such that the equilibrium relationship is linear and $q^* = KC$.

When micropore diffusion is the primary mass transfer resistance for a spherical crystal, a mass balance on the crystal is performed to obtain

$$\frac{\partial q}{\partial t} = \frac{1}{r^2}\frac{\partial}{\partial r}\left(r^2 D_c \frac{\partial q}{\partial r}\right). \tag{A.5}$$

If the concentration change is small giving a small change in adsorbed phase concen-

tration, it can be assumed that the micropore diffusivity, D_c, is constant which simplifies Equation A.5 to

$$\frac{\partial q}{\partial t} = D_c \left(\frac{\partial^2 q}{\partial r^2} + \frac{2}{r} \frac{\partial q}{\partial r} \right). \tag{A.6}$$

The relevant initial and boundary conditions to solve Equation A.6 for the amount adsorbed as a function of time are:

$$\begin{array}{ll} \text{at } t = 0, & q = q_0; \\ \text{for } t \geq 0, & q(r_c, t) \rightarrow q^*; \\ \text{for } t \rightarrow \infty, & q(r, t) \rightarrow q^*; \\ \left.\frac{\partial q}{\partial t}\right|_{r=0} = 0 & \text{for all t.} \end{array} \tag{A.7}$$

The resulting solution to Equation A.6

$$\frac{m}{m^*} = \frac{\bar{q} - q_0}{q^* - q_0} = 1 - \frac{6}{\pi^2} \sum_{n=1}^{\infty} \frac{1}{n^2} \exp\left(-\frac{n^2 \pi^2 D_c t}{r_c^2} \right), \tag{A.8}$$

and this equation for micropore diffusion resistance is used to model the results in the following section.

Note that another form of Equation A.8 is

$$\frac{m}{m^*} = \frac{\bar{q} - q_0}{q^* - q_0} = 6 \left(\frac{D_c t}{r_c^2} \right)^{1/2} \left[\frac{1}{\sqrt{\pi}} + 2 \sum_{n=1}^{\infty} \text{ierfc} \left(\frac{n r_c}{\sqrt{D_c t}} \right) \right] - \frac{3 D_c t}{r_c^2}. \tag{A.9}$$

Results and Discussion

Analysis of TGA Adsorption Kinetics

Kinetics for adsorption of propylene glycol on H-MFI at 0.28 Pa (furnace temperature of 303 K, saturator temperature of 273 K, bubbler flow rate at 25 mL min^{-1}, diluent flow rate of 100 mL min^{-1}) are presented in Figure A.2. It was found that the time to reach equilibrium was very long- on the order of approximately 50 hours. The uptake data is presented relative to both absolute (Figure A.2(a)) and square root (Figure A.2(b)) time and fits of the surface resistance (Equation A.3) and diffusion-limited (Equation A.8) models are shown. Note that the crystal radius, r_c, was approximated as 1 micron, and the surface film thickness, δ, was assumed to scale with the crystal size, and was thus also set to 1 micron.

Although the best fit with the data is achieved with the surface resistance model, the diffusivities calculated by the surface resistance and diffusion-limited models were 5.5×10^{-14}

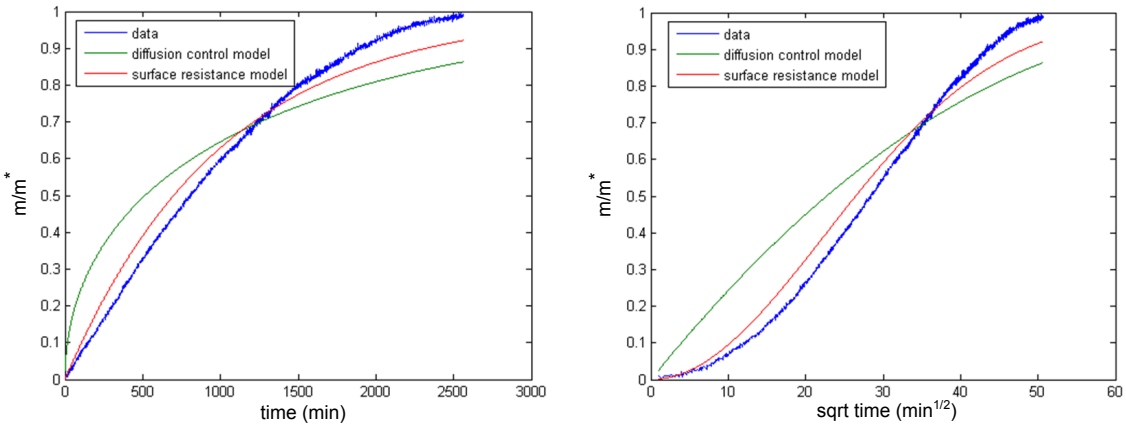

(a) (b)

Figure A.2: Propylene glycol adsorption at 0.28 Pa (P/P_0=0.1) onto H-MFI at 303 K with respect to (a) time and (b) square root time.

and 9.84×10^{-15} cm^2 s^{-1}, respectively, and are only a factor of 6 different. In order to assess the validity of these diffusivities, they were compared with reported diffusivites for other organic molecules on zeolites. Choudhary *et al.* modeled the initial uptake of liquid adsorption of n- and iso-butanol on H-ZSM-5 (aluminum-containing MFI) at 293 K to find diffusivities of 10^{-10} and 10^{-12} cm^{2}s^{-1} for these adsorbates, respectively,[143] which are several orders of magnitude larger than the diffusivities found for propylene glycol here.

The small diffusivities could be the result of intrinsic diffusion behavior or artefacts associated with the TGA. It was of interest to identify if the source of the slow equilibration time was the instrumentation which could then potentially be resolved in order to expedite adsorption data collection. Contributions from external mass transfer resistance were probed though calculation of the characteristic time, τ, which is defined as

$$\tau = \frac{L^2}{D}, \tag{A.10}$$

where L is the characteristic diffusion length and D is diffusivity. Using a typical bulk gas diffusivity of 0.1 cm^2 s^{-1} and a diffusion length of 100 micron for external fluid film mass transfer (*i.e.* the macroparticle radius, R_p, is 100 micron), one obtains a characteristic time of $\sim$0.001 s and, therefore, the long equilibration time cannot be attributed to fluid film resistance. The time for radial diffusion of propylene glycol in the TGA furnace (radius of $\sim$1 cm^2) was also calculated and found to be on the order of 1 s. These analyses indicate that another resistance is the cause of the slow equilibration time.

Surface resistance due to pore blocking was examined by performing adsorption on MFI crystals that had been contacted with 10 wt% HF solution for 5 minutes as described by

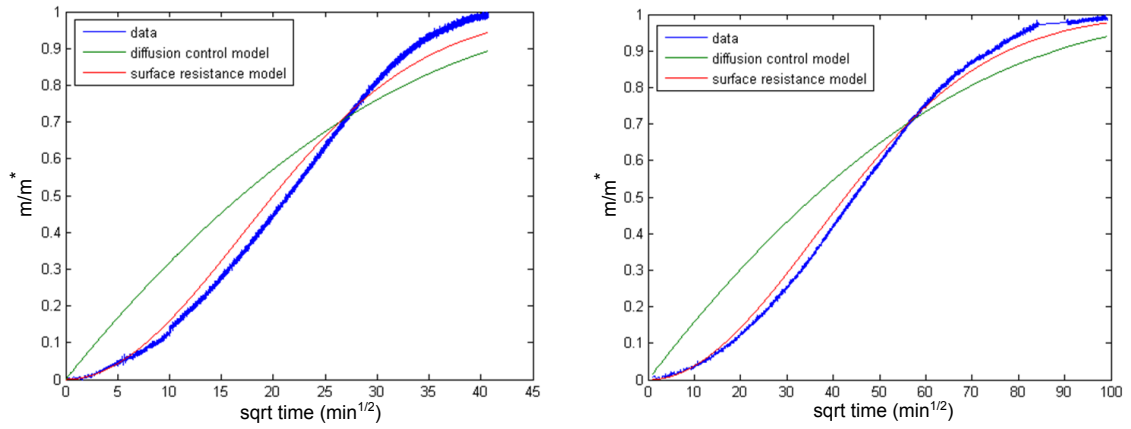

Figure A.3: Propylene glycol adsorption at 0.28 Pa (P/P_0=0.1) onto (a) 3DOm-MFI and (b) SPP at 303 K.

Gueudré *et al.*[140] Although the measurement did not fully equilibrate, it was found that the amount adsorbed was approximately equivalent to that measured on the untreated MFI (0.06 g adsorbed per g zeolite) with a diffusivity on the same order of magnitude (4.4×10^{-14} cm^2 s^{-1}). Therefore, it does not appear that the HF etching had any effect on the adsorption rate.

Although the diffusion-limited model does not provide the best fit of the data, the effect of intracrystalline diffusion on the uptake rate was examined by performing adsorption kinetics studies on 3DOm-MFI and SPP, both of which contain MFI micropores as well as large mesopores which are expected to decrease the barrier to diffusion. The adsorption rate data were collected at identical conditions as the data on H-MFI and are presented in Figure A.3. It can be observed that the surface resistance model also provides the best fit for these data. Furthermore, the adsorption time constants were still found to be on the order of hours, ranging from 29 hours for 3DOm-MFI to 131 hours for the SPP material, and these values scale with the amount adsorbed. That is, the shortest time constant and lowest amount adsorbed were both identified on 3DOm-MFI, whereas the SPP material, which took the longest to equilibrate, also adsorbed the most at 0.13 g propylene glycol per g zeolite.

The coincidence of short equilibration time and low equilibration coverage on the same material is an indication that delivery rate may contribute to the slow uptake rate. The delivery rate of propylene glycol at the conditions reported here is 1.7×10^{-5} mmol min^{-1} with an equilibration uptake of 0.05 g propylene glycol per g zeolite (0.002 mmol total). Ethanol adsorption was studied using the same adsorbent, furnace temperature, and reduced pressure (P/P_0 where P_0 is the adsorbate vapor pressure), which resulted in a final loading

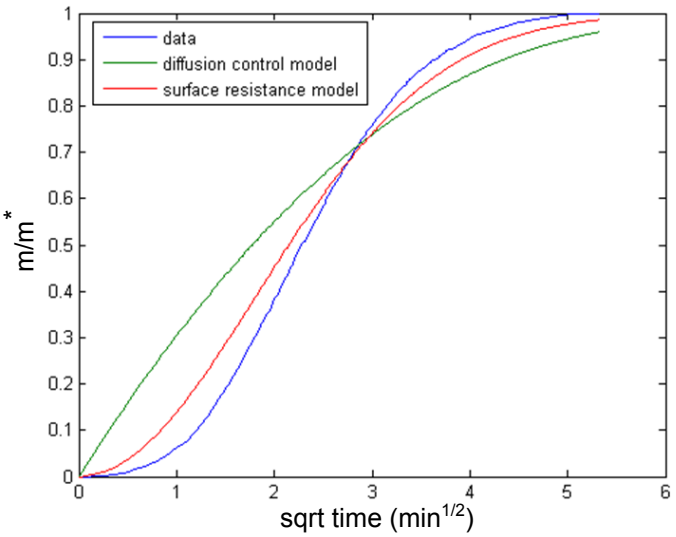

Figure A.4: Ethanol adsorption at 110 Pa (P/P_0=0.1) onto H-MFI at 303 K

of 0.005 mmol. Due to the three orders of magnitude greater vapor pressure of ethanol at 303 K (10 kPa versus 0.03 kPa for propylene glycol), the ethanol partial pressure must be three orders of magnitude greater than that of propylene glycol in order to achieve the same reduced pressure. Since the partial pressure is proportional to the delivery rate, this results in a delivery rate which is two orders of magnitude greater (6×10^{-3} mmol min^{-1}), and it can be seen in Figure A.4 that ethanol adsorption kinetics are also much faster, with equilibrium achieved in less than one hour.

This difference in adsorption kinetics could also be attributed to differences in diffusivities, however, an examination of the diffusivity measured for ethanol indicates that delivery rate may also play a role. A diffusivity of 8.3×10^{-12} is determined from the surface resistance model fit of the ethanol uptake rate data (see Figure A.4) which is three orders of magnitude smaller than the diffusivity reported by Choudhary *et al.* ($\sim10^{-9}$ cm^2s^{-1}) for liquid adsorption at 274 K. Therefore, delivery rate is likely to also have an effect of the equilibration rate.

On the basis of the results presented, it is recommended that adsorption is performed at above ambient temperatures, which allows for higher partial pressures to achieve the same reduced pressure, thereby giving higher delivery rates and shorter equilibration times. These results also indicate that volumetric batch adsorption techniques could be better suited for measuring adsorption of non-volatile molecules.

Conclusions

Batch mass transfer modeling of propylene glycol adsorption kinetics on zeolites using a TGA indicate that the predominant resistance to mass transfer is surface resistance. Analysis of the time constants for external and fluid film mass transport indicate that these are not the primary barriers for adsorption in the system, while the adsorbate delivery rate, which is proportional to the partial pressure, does appear to be correlated with the uptake rate. Therefore, in order to reduce the time to obtain equilibrium measurements on a TGA, it is recommended that they are conducted at a higher temperature, which allows for higher partial pressure measurements and delivery rates. Otherwise, it is recommended that these measurements are performed with a batch volumetric technique.

APPENDIX

B

XRD STUDY OF HYDROXYMETHYLFURFURAL ADSORPTION ON SILICALITE-1

Introduction

X-ray diffraction (XRD) patterns for silicalite-1 loaded with 5-hydroxymethylfurfural (HMF), a potential bio-derived platform chemical that can be obtained from dehydration of fructose, are presented to show that the increasing HMF coverage may induce a monoclinic-orthorhombic shift in silicalite-1 symmetry. These results indicate that accurate modeling of HMF adsorption could require the use of a flexible silicalite-1 structure.

Methods

Aqueous adsorption experiments were performed as described in Section 2.2, with the exception that equilibrium was assumed to occur instantaneously (an assumption that is supported by preliminary time dependent adsorption studies). HMF reagent information can be found in a previous report.[6] The silicalite-1 adsorbent was synthesized as described in Section 2.2.1. Initial concentrations of HMF in water ranging from 0.17 to 58 g/L (see Table B.1) were used in the measurements on the basis of aqueous HMF adsorption isotherms reported by Ranjan *et al.*[6]

Note that the initial concentrations were known from sample preparation, and the final concentrations and amounts adsorbed were calculated using the data from Ranjan *et al.*[6], which are shown in Figure B.1. That is, the data from Ranjan *et al.* were fit with the linearized Langmuir regression as described in Section 3.5.1 in order to obtain values of 2.487 [L solution per g HMF] and 0.1862 [g HMF adsorbed per g zeolite] for K and $[*]_0$, respectively. The amount adsorbed, a, is related to these parameters by

Table B.1: HMF concentrations used in XRD measurements

samples	initial concentration (g/L)	calculated final concentration (g/L)	amount adsorbed (g per g zeolite)
1	0.167	0.162	0.053
2	0.251	0.244	0.070
3	4.92	4.90	0.172
4	9.84	9.82	0.179
5	14.8	14.8	0.181
6	58.2	58.2	0.185

$$a = \frac{[*]_0 K C_F}{1 + K C_F}, \tag{B.1}$$

where C_F is the final solution concentration. The amount adsorbed is also related to the initial and final solution concentration using

$$a = \frac{(C_I - C_F)V}{m_z}, \tag{B.2}$$

where C_I is the initial solution concentration, V is the solution volume (which is assumed to be constant in these measurements), and m_z is the mass of zeolite added. It can be observed from Equations B.1 and B.2 that there are two equations and two unknowns that allowed for calculation of C_F and a, and these values are reported for samples 1-6 in Table B.1 and Figure B.1.

X-Ray diffraction (XRD) was performed at 20 keV on Beamline X18A at Brookhaven National Laboratory, which is equipped with a Si(111) channel cut monochromator. 50 μL of the water/HMF/zeolite solutions was transferred to a kapton capillary and the diffracted x-rays were collected with a 2-dimensional detector.

Results and Discussion

XRD measurements performed on the empty kapton cell, the cell containing pure deionized water, and the cell with a solution of HMF and water are presented in Figure B.2. Diffraction of the empty kapton capillary results in a peak at approximately 2° 2θ while a broad peak at 11° 2θ develops when the capillary is loaded with pure water and the aqueous HMF solution. This peak represents a d-spacing of ~3.2 Å that several authors have shown via XRD,[144–147] neutron diffraction,[146] and Monte Carlo modeling[148] is from long range structure in ambient temperature water.

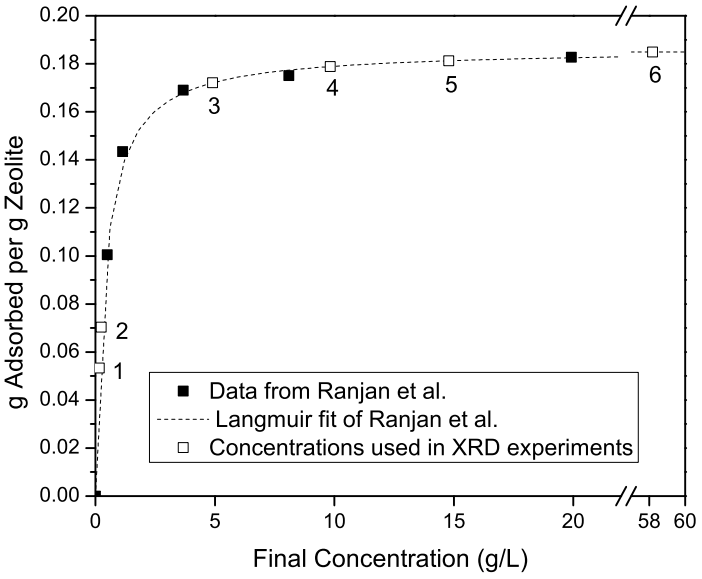

Figure B.1: HMF adsorption data reported by Ranjan *et al.*[6] and calculated final concentrations and loadings for samples 1-6 used in this study. Dashed line represents a linearized Langmuir fit of the data from Ranjan *et al.* with K=2.487 [L solution per g HMF] and $[*]_0$=0.1862 [g HMF adsorbed per g zeolite]

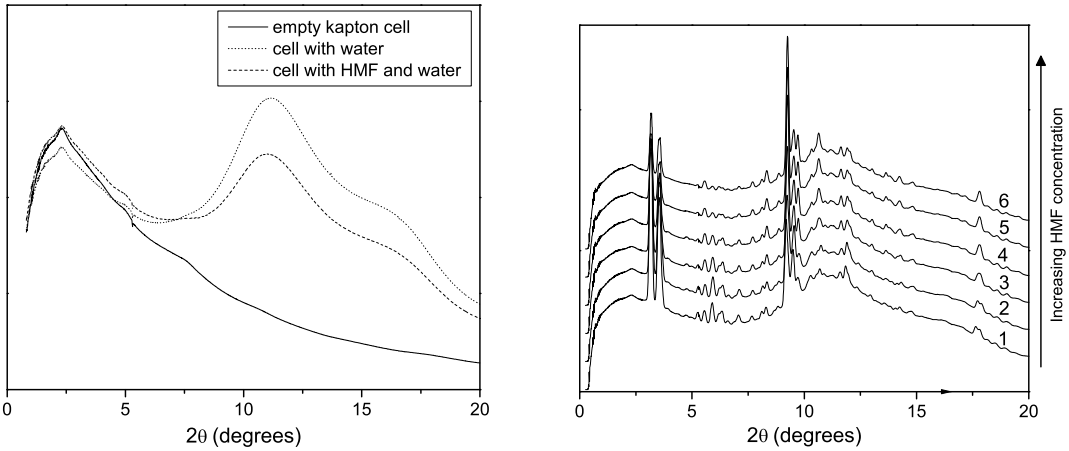

(a) (b)

Figure B.2: Diffraction patterns for (a) the sample background and (b) raw samples without background correction.

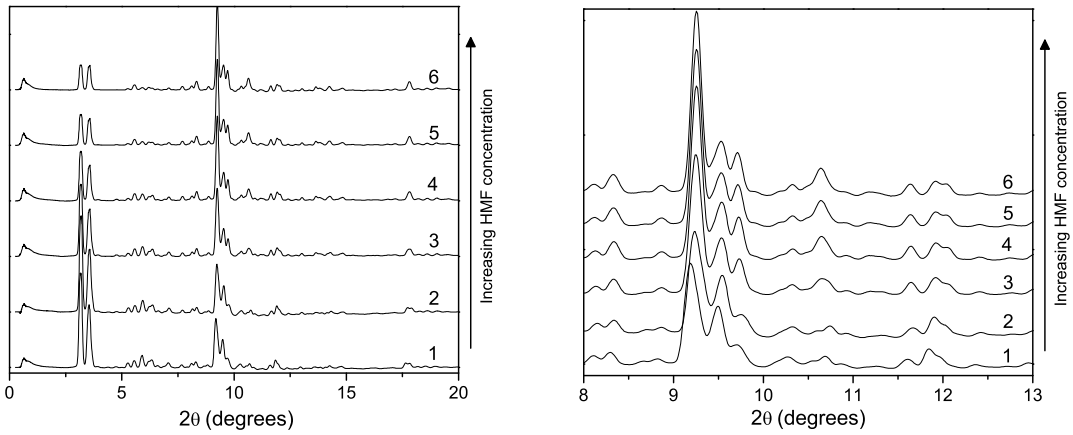

(a) (b)

Figure B.3: Background corrected diffraction patterns for silicalite-1 with adsorbed HMF in the ranges of (a) 0-20° and (b) 8-13° 2θ.

The raw XRD data for samples 1-6 is also shown in Figure B.2, and background contributions were removed from these data to obtain the diffraction patterns in Figure B.3. It can be seen that the 011 and 020 planes (peaks at 3.2 and 3.6° 2θ, respectively) have the greatest intensity for dilute HMF concentrations, and become increasingly attenuated with increasing HMF concentration. For the highest HMF concentration, the most intense peak is at 9.2° 2θ that is associated with the 051 plane.

This shift in peak intensity has been observed upon calcination of MFI zeolites.[118] That is, the as-synthesized zeolite, which is loaded with the organic structure directing agent, exhibits an XRD pattern with a prominent peak at approximately 9° 2θ (23° 2θ for Cu Kα radiation), and this peak is superseded by the peaks from 3-4° 2θ (7.5-9.5° 2θ for Cu Kα radiation) upon removal of the SDA due to calcination.

Furthermore, these changes in peak intensity are commensurate with a monoclinic-orthorhombic symmetry shift that is postulated from the 8 to 13° 2θ XRD data as shown in Figure B.3(b). The XRD pattern generated for monoclinic MFI using the coordinates from van Koningsveld *et al.*[2,12] contains two prominent peaks for the 051 and 033 planes at 9.233 and 9.583° 2θ, respectively, and these can be observed in the patterns for samples 1 and 2, which contain less than 0.08 g of HMF per g zeolite. Alternatively, samples 3-6, which have HMF loadings greater than 0.17 g HMF per g zeolite (within 6% of saturation), exhibit three peaks in the range 9 to 10° 2θ (9.209, 9.489, and 9.770° 2θ for the 501, 151, and 133 planes, respectively) which is in agreement with the simulated pattern for orthorhombic MFI.[3,12] Therefore, it appears that adsorption of aqueous HMF induces a change in the silicalite-1 symmetry from monoclinic to orthorhombic.

An implication of this observation is that accurate modeling of the adsorbate-structure relationship may not be achieved with a rigid zeolite framework. Structure flexibility is critical in identifying the preferential adsorption sites of HMF, particularly at loadings in excess of 0.17 g HMF per g zeolite where a structural change in the zeolite is induced.

Conclusions

Analysis of XRD data for adsorbed HMF on silicalite-1 indicates that a monoclinic-orthorhombic symmetry shift may occur due to HMF adsorption. These results show that simulation of HMF adsorption on MFI may be best achieved with a flexible zeolite framework.

APPENDIX

C

LIST OF PURE SILICA ZEOLITE ANALOGUES

While over 200 zeolite frameworks have been catalogued by the International Zeolite Association[12], as of 2009 only approximately 40 frameworks had been synthesized in their pure silica forms. These frameworks are listed in the table below.

Table C.1: Zeolites which can be synthesized in pure silica form

Framework	Name	Framework	Name
AFI	SSZ-24	LTA	ITQ-29
AST	Octadecasil	MEL	ZSM-11
ATS	SSZ-55	MFI	Silicalite, ZSM-5
BEA	Beta	MRE	ZSM-48, UTD-12
BEC	ITQ-14	MSE	YNU-2
CDO	CDS-1, MCM-65	MTF	MCM-35
CFI	CIT-5	MTN	ZSM-39, Dodecasil-3C
CHA	Chabazite	MTT	ZSM-23
DDR	DDR3	MTW	ZSM-12
DOH	Dodecasil-1H	MWW	MCM-22, ITQ-1
DON	UTD-1	NON	Nonasil
EUO	EU-1	NSI	Nu-6(2)
FAU	DAY	RRO	RUB-41
FER	Ferrierite	RTE	RUB-3
GON	GUS-1	RUT	RUB-10
IFR	SSZ-42, ITQ-4	RWR	RUB-24
IHW	ITQ-32	SAS	SSZ-73
ISV	ITQ-7	SGT	Sigma-2
ITE	ITQ-3	SOD	Sodalite
ITH	ITQ-13	STF	SSZ-35, ITQ-9
ITW	ITQ-12	STT	SSZ-23
IWR	ITQ-24	TON	Theta-1